THE MOTION OF A THETA PINCH PLASMA IN A PERTURBING MAGNETIC FIELD

by

ALAN WOOTTON

Department of Physics,
Royal Holloway College

This thesis is presented for the Degree of Doctor of Philosophy in the University of London

May, 1973

ABSTRACT

The motion of a theta pinch hydrogen plasma in the presence of a local perturbing magnetic field is described. A small coil outside the plasma was excited by capacitors to produce a dipole field. Experiments were performed on a 3.5 m long, collisional , high-beta plasma with a temperature of 60 eV, a radius of 1 cm and a density of 10^{16} particles cm^{-3}. Sinusoidal currents of 20 kA and frequency 10^6 rad s^{-1} in a 3-turn perturbing field coil produced oscillating plasma displacements of 1 cm, which propagated along the plasma with a velocity of 20 cm μs^{-1} . The displacement was proportional to the coil current, inversely proportional to the axial magnetic field outside the plasma, and was spatially damped with an e-folding length of 20 cm. Using a step current waveform the plasma could be moved to an equilibrium position which was displaced from the initial unperturbed equilibrium. Experiments on a 2 m long low-beta plasma with a temperature of 10 eV showed that propagating plasma displacements of 0.5 cm could be obtained, which were damped in 5 cm.

Predictions of the plasma displacement and velocity are made by considering the motion as long wavelength, m = 1 perturbations about an equilibrium position. Damping mechanisms are introduced by making an analogy between the excited waves and Alfven waves in a dissipative medium.

Feedback stabilization of long wavelength gross modes in theta-pinch plasmas is shown to be possible, using a system of coils similar to those used to excite plasma motion.

Experiments were performed to determine the effect of the initial conditions on the 3.5 m theta-pinch parameters, and the results compared with computations. A computed heating rate was obtained; including partial ionization of the initial gas revealed a value of the initial rate of change of axial magnetic field below which no heating occurred. This cut-off was overcome experimentally by using bias fields.

ACKNOWLEDGEMENTS

I am grateful to Culham Laboratory, of the United Kingdom Atomic Energy Authority, for the generous provision of experimental facilities and technical assistance in the studies described here.

The machine on which most of the experimental work was performed was designed under the direction of Dr A.A. Newton, but the experimental studies of theta pinch heating described in Chapter IV were performed by the author alone. Computations of heating and energy loss processes, described in Chapter V, were directed by Dr A.A. Newton, but the interpretation of the results and comparison with experiments were made by the author.

The theory describing perturbed plasma motion described in Chapter VI was developed by the author, although an independent theory was developed by Dr J. Junker of the Max-Planck-Institut fur Plasmaphysik, Garching bei Munchen. Solutions of the equations of motion of a plasma column were performed by the author, the numerical code used for this purpose being adapted from one written by W. Schneider of the Max-Planck-Institut.

Experimental studies of the perturbed motion of a low beta plasma were performed by the author with assistance from Dr J. Junker. Studies of the high beta plasma motion, described in Chapter VII, were made by the author with initial assistance from Dr N.F. Nalesso, of the Universite di Padova. Valuable practical assistance was provided by Mr G. Harding and Mr L. Piper. Interpretation of the results, in Chapter VIII, and the feasibility study of feedback stabilization in Chapter IX, were undertaken by the author alone.

Finally I would like to thank my supervisor, Dr E.R. Wooding, and the members of Division 'B', Culham Laboratory, in particular Dr A.A. Newton, for their valued assistance throughout my project. I also thank Ina Godwin, who typed this thesis.

ERRATA

Page	Line	Line beginning	Correction
5	30	3.4 The pre-ionization ..	pre-ionization should read preionization
11	11	Energy and particle loss	process should read processes
27	9	The earth return	systen should ready system
28	13	3.4 The pre-ionization ...	pre-ionization should read preionization
28	19	A pre-ionization	pre-ionization should read preionization
32	1	a) The 3.5 thetatron	3.5 shoud read 3.5m
54	24	To maintain pressure	Insert comma after '(see section A1.3)'
58	14	In this experiment	continuum light should read soft X-ray, and larger should read smaller
58	25	none of the experiments ...	experiments should read experimental results
81	9	equation (6.6.2)	Denominator should be b^4 not b^2
125	25	A complete calculation ...	The paragraph should be replaced by the following

A complete calculation of the $\bar{j} \times \bar{B}$ forces for a low beta plasma would result in a displacement related to the sector coil current I_d by terms in both I_d and I_d^2. Although the diamagnetic current j_o approaches zero for $\beta \ll 1$, the observed displacements were finite and were linearly dependent on I_d. Therefore the model described in Section 6.5 cannot apply to the experimental situation because the second force term in equation (6.5.1), which results from the interaction of the axial magnetic field and the currents induced in the plasma by the sector coil, is not negligible. The plasma displacement about the equilibrium (see Section 6.4) must include the displacements produced by both the linear $\bar{j} \times \bar{B}$ forces.

CONTENTS

C O N T E N T S
(continued)

C O N T E N T S
(continued)

Page

CHAPTER VI

A THEORY FOR PLASMA DISPLACEMENTS DUE TO A LOCAL PERTURBING MAGNETIC FIELD

CHAPTER VII

AN EXPERIMENTAL STUDY OF THE PLASMA MOTION PRODUCED BY A PERTURBING MAGNETIC FIELD

CONTENTS
(continued)

C O N T E N T S
(continued)

CHAPTER I

A GENERAL INTRODUCTION

The motion of a theta pinch plasma in the presence of a local perturbing magnetic field is discussed[68,79]. Experiments performed on a 3.5m theta pinch with a perturbing magnetic dipole field produced gross plasma displacements, which propagated axially and were spatially damped. The displacement, propagation velocity and damping were measured as functions of the plasma and perturbing field parameters.

A theory is presented which explains the plasma motion as long wavelength, m = 1 (see Appendix A1.3 - the m number) perturbations about an equilibrium position. The resulting transverse, hydromagnetic waves are similar to Alfven waves[47]. Previous experiments on Alfven wave propagation have been performed with torsional[81] or m = 0 [82] (sausage) waves in low temperature, low beta plasmas, where the plasma pressure is negligible. No experiments on the effect of perturbing magnetic fields on high beta, high temperature plasmas had been reported at the start of the project. Since then the effect of a spatially uniform perturbing force has been described[83]. This differs from that described in the text because no propagation occurred.

Feedback stabilization of long wavelength, gross instabilities in theta pinch plasmas is considered, as an extension of the experiments reported. These experiments showed that the position of a neutrally stable plasma could be controlled by the perturbing fields of a current carrying coil. The force between the perturbing field and the plasma can then be used as a feedback force to control instabilities. Experiments to control gross modes in high beta plasmas, reviewed in Chapter IX, have been restricted to systems with a spatially uniform feedback force[85,86], although the control of modes in low beta plasmas is well documented (see the review

of reference 84). With the system of perturbing field coils described in the text it would be possible to pin a plasma at a finite number of positions. In this way the confinement times of toroidal theta pinch type plasmas could be increased towards the times necessary for a fusion reactor.

The 3.5m thetatron, described in Chapter III, was built specifically for the studies of perturbed motion. Initial measurements showed that the peak plasma temperature was less than 40 eV; under these conditions it was thought that the $m=1$ Alfven waves produced were resistively damped. A series of experiments[59] was undertaken to obtain higher temperatures and so reduce this damping. The results, compared with computations, emphasised the importance of considering energy losses in the design of low power input thetatrons.

Most theta pinches operate with the azimuthal electric field at the vacuum tube wall $E_\theta \geqslant 200\,V\,cm^{-1}$ [42,43], but for the 3.5m theta pinch E_θ was $\leqslant 70\,V\,cm^{-1}$. Partial ionization and impurities were found to govern the heating rates for $E_\theta \leqslant 200\,V\,cm^{-1}$; small negative bias fields $\simeq -300$ gauss were used to overcome the energy losses and increase the temperature.

MKS units are used throughout the text for equations, unless it is stated otherwise. A glossary of terms and the nomenclature used is given as Appendix A1.

CHAPTER II

A REVIEW OF THETA PINCH EXPERIMENTS AND THEORY ON THE FORMATION, HEATING AND GROSS STABILITY OF THE PLASMA

2.1 INTRODUCTION

All the experiments described in this thesis were performed on a theta pinch plasma. This chapter describes those properties of a theta pinch which are necessary to understand the reported results. The experimental and computational studies of the effect of the initial conditions on the plasma parameters (see Chapters IV and V) are concerned with plasma formation and heating. Therefore the implosion, adiabatic and Joule heating stages are described. Energy and particle loss process are outlined, together with the conditions under which they occur. The use of bias fields to control plasma parameters is considered.

In the description of the experimental results, reference is made to certain gross, or magnetohydrodynamic (MHD), instabilities. Three of these, the resistive, rotational and kink or $m=1$, modes, are described. The $m=1$ mode is considered in Chapter IX for feedback stabilization. The theory presented in Chapter VI to describe perturbed plasma motion also concerns this mode; $m=1$ stability theory is then reviewed in detail.

The final section presents the criteria for designing a device (a thetatron) to produce a theta pinch plasma of required parameters. These criteria were used to design the thetatron described in Chapter III.

2.2 A TYPICAL THETA PINCH AND THETATRON

In its simplest form a thetatron consists of a cylindrical metal compression coil connected to a capacitor bank. A cylindrical vacuum vessel is supported inside this coil, and filled to typically 30 mtorr with hydrogen. The gas is pre-ionized by an axial current discharge, after which a fast rising current from the high energy, low inductance capacitor

bank is passed around the compression coil. An axial magnetic field is produced, which, together with the azimuthal current induced in the gas, constricts the gas to form a theta pinch plasma. Fig.2.1 illustrates a typical thetatron, the current waveforms and the plasma radial variation with time. The time during which the gas is constricted, or pinched, is called the implosion stage. This is followed by the adiabatic heating stage. Densities of 10^{16} particles cm^{-3} and temperatures of 100 eV are produced.

An axial magnetic bias field can be applied to the gas before the main discharge to control certain plasma parameters (see Section 2.7). If a low frequency current is passed around the compression coil before the main azimuthal current, the resulting bias field is constant over the plasma lifetime (see Fig.2.1(b)).

2.3 THE IMPLOSION STAGE

The main azimuthal current in the compression coil produces a current sheath in the preionized gas. The fast rising axial magnetic field acts as a piston, and a shock wave is produced. This shock wave travels radially inwards, heating electrons and ions. It is usually assumed that microinstabilities dominate the particle collision frequencies, so that the shock thickness is independent of the binary collision mean free path[1]. Experimentally determined anomalous resistivities can then be explained[2,3].

Particle collection models predict that the velocity of the gas collecting front (the shock) is a function of the azimuthal electric field E_θ,[4] which is related to the initial rate of change of axial magnetic field $\dot{B}_o$ by

$$2\pi r E_\theta = \pi r^2 \dot{B}_o \, . \qquad \ldots (2.3.1)$$

The conservation equations[5] relate the plasma temperature T to the Mach number M. Then

$$T = f(M) = f(\dot{B}_o) \qquad \ldots (2.3.2)$$

where M, the Mach number, = (shock velocity)/(sound speed). Kever[6] has derived an analytic expression for the temperature at the end of an irreversible implosion with no initial bias field or cross field diffusion:

$$kT_s = \frac{2}{9}\, a\, b\, r_w\, \dot{B}_o \left(\frac{m_i}{\mu_o n_i}\right)^{\frac{1}{2}} \qquad \ldots (2.3.3)$$

where kT_s is the temperature, assuming equipartition of energy between ions and electrons, in eV ;

a is a numerical factor; $\frac{1}{3}$ for a snowplough model[4] and 1 for a free particle model[7] ;

b is an energy transfer coefficient between the electrical circuit and the plasma

$\dot{B}_o$ is in Tesla μs^{-1} ;

m_i is the ion mass, in gm ;

n_i is the initial ion density, in particles cm^{-3} ;

r_w is the vacuum tube radius, in cm.

This expression has been modified to include trapped flux[8]; for typical experimental conditions T_s is reduced by 30%.

When the shock wave reaches the axis, the plasma executes $m = 0$ (see Appendix A1 , section 1.3 - the m number) oscillations, with a frequency dependent on the magnetic field and the line mass[9] (see Appendix A2.8). During this stage particle collisions produce an equipartition of energy.

2.4 ADIABATIC HEATING

The external axial magnetic field continues to increase after the implosion, adiabatically compressing the plasma. An energy and pressure balance equation can be written to predict the resulting plasma temperature. For no losses[10]

$$\frac{T_1}{T_2} = \left(\frac{B_1}{B_2}\right)^{\frac{4}{6-\beta}} \qquad \ldots (2.4.1)$$

where

$$\beta = \frac{2nkT}{B^2/2\mu_o} \quad \text{(see section A1.3 - Beta)}$$

Subscript 1 refers to the initial conditions

Subscript 2 refers to the final conditions.

Mewe[11] has analysed the effect of a radial adiabatic compression superimposed on a shock heated plasma. Using Kever's expression, equation (2.3.3), the temperature $\hat{T}$ at peak magnetic field $\hat{B}$ is, for a deuterium plasma,

$$k\hat{T} = 200\, d \left(\frac{r_w \dot{B}_o \hat{B}}{p}\right)^{\frac{2}{3}} \qquad \ldots (2.4.2)$$

where $k\hat{T}$ is the average peak temperature, $k(\hat{T}_e + \hat{T}_i)/2$, in eV;

$\hat{B}$ is in Tesla;

p is the filling pressure, in mtorr;

$\dot{B}_o$ is in Tesla μs^{-1};

d is a function of the plasma radius and β, $\simeq 1$;

r_w is the vacuum tube radius, in cm.

2.5 JOULE HEATING

Azimuthal electric currents flowing in the plasma produce Joule heating. Magnetic field diffusion also creates currents which result in heating. Most Joule heating occurs during the implosion stage, but Mewe has estimated that about 30% more is needed to account for measured plasma temperatures[11].

2.6 ENERGY AND PARTICLE LOSS PROCESSES

2.6.1 Introduction

Direct heating processes compete with energy and particle loss processes in any plasma. Fig.2.2 tabulates the most important loss mechanisms, the conditions under which they occur, their characteristic time and their effect on the plasma. Two of these, which are considered in a discussion of experimental results (see Chapter V), are now dealt with in more detail.

2.6.2 The Effect of Partial Ionization

It is usual to preionize the gas in a theta pinch; the first half cycle of the main current discharge then produces a hot plasma. If the preionization system is poor, energy imparted to the plasma during the implosion is used to ionize existing neutrals. This reduces the shock heating.

2.6.3 The Effect of Impurities

A common cause of energy loss in plasmas is the presence of impurities, often introduced by plasma contact with the vacuum vessel walls. Occluded oxygen exists in quartz vessels; this can be reduced by baking the system, or by repeated plasma wall contact.

Fig.2.3 shows the cooling rate due to oxygen in a hydrogen plasma[13]. The effects of bremsstrahlung, recombination (see section A.1.3) and line radiation are added, for an optically thin plasma, to give the power radiated P:

$$P = f(T_e) n_e n^* \qquad \ldots (2.6.1)$$

where n^* is the impurity particle density. The function $f(T_e)$ is plotted. Between 25 and 100 eV, $f(T_e)$ decreases. Below 100 eV the losses are dominated by line radiation; above 100 eV bremsstrahlung dominates. At very high temperatures the oxygen atoms are completely ionized.

2.7 THE EFFECT OF BIAS FIELDS

In the heating experiments to be described in Chapter IV, a bias field was used to control certain plasma characteristics. The results of these experiments disagreed with initial computational predictions (see Chapter V), so that the effect of the bias field was studied more carefully. This section summarises previous experimental results[17-19].

If a negative bias field (negative with respect to the main axial field) is introduced into the gas before the main azimuthal current discharge,

the negative field can diffuse across the plasma current sheath and produce extra Joule heating. During the time the plasma contains a trapped negative flux the density profile is hollow; that is, the peak density occurs symmetrically about the axis (see Chapter IV, Fig.4.4). The internal and external field lines may close at the plasma ends, resulting in a plasma contraction (see Section 2.8.3).

A positive bias field increases the positive trapped flux normally found in a theta pinch. This reduces the efficiency of the shock heating, resulting in lower temperatures. Larger plasma radii are produced; at the same time the plasma beta value is reduced.

If bias fields are applied before the axial preionization current, the gas breakdown time is changed[20]. It has been suggested that small bias fields, either positive or negative, reduce the electron loss to the walls, increasing the ionization efficiency and reducing breakdown times. Large bias fields reduce ion induced secondary emission from the walls, thus inhibiting the ionization process and increasing the breakdown time. Experiments have shown that the minimum breakdown time occurs when bias fields between 200 and 300 gauss are used[20].

2.8 MAGNETOHYDRODYNAMIC (MHD) INSTABILITIES

2.8.1 Introduction

Plasma lifetimes can be limited by MHD, or macro, instabililities, which drive the plasma to the vacuum vessel walls. Three of these, the rotating $m=2$, the resistive, and the $m=1$ long wavelength, or kink, modes are described. Each is referred to later in the text. A review of $m=1$ stability theory for theta pinches is given in Section 6.2.

2.8.2 The Rotational Instability

A rotating $m=2$ instability, illustrated in Fig.2.4(a), is the most common naturally occurring mode in a theta pinch[21-23]. Two possible mechanisms have been shown experimentally possible.

In one model[21,24] it is supposed that the radial electric space charge field in the current sheath is short-circuited at the compression coil ends, producing a radial displacement current $\bar{j}_r$ which in turn produces an azimuthal force $\bar{F}_\theta$;

$$\bar{F}_\theta \propto \bar{j}_r \times \bar{B}_z \ . \qquad \ldots (2.8.1)$$

Haines[25] has proposed that small transverse fields $\bar{B}_r$ interact with the azimuthal plasma current $\bar{j}_\theta$ to give a longitudinal Hall current $\bar{j}_z$. Then

$$\bar{F}_\theta \propto \bar{j}_z \times \bar{B}_r \ . \qquad \ldots (2.8.2)$$

The growth rate γ is given by

$$\gamma = (m-1)^{\frac{1}{2}}\Omega \qquad \ldots (2.8.3)$$

where Ω is the angular plasma velocity
m is the azimuthal mode number.

The observation that $m=2$ is the fastest growing mode is explained by considering finite Larmor radius effects[26,27].

2.8.3 The Resistive Instability

If resistivity is included in MHD stability analysis, the idea of 'frozen in' field lines (see Section A.1.3) is not applicable. The plasma and the magnetic field become detached, allowing new unstable modes[28,29]. In a reverse bias theta pinch, where the plasma lies within an annular cylinder with oppositely directed magnetic fields on either side, the field lines may close at the plasma ends (see Fig.2.4(b)). An axial contraction results. If the plasma has a finite conductivity the field lines may close anywhere along the axis, producing plasma rings. The instability produced is called the resistive tearing mode, and has been seen experimentally[30-32].

2.8.4 The Kink, or Long Wavelength m = 1, Instability

A linear theta pinch is neutrally stable to long wavelength, m = 1 instabilities[33]. If an $l = 0$ (bulged) field is added, the m = 1 instability is unstable with a growth-rate γ given by [34]

$$\gamma_{m=1} = \frac{V_A L}{r_{po}} \left\langle \left(\frac{dr_p}{d_z}\right)^2 \right\rangle \frac{\beta_o(1-\beta_o)(3-2\beta_o)}{(2-\beta_o)^{\frac{3}{2}}} \qquad \ldots (2.8.4)$$

where L is the bulge length

V_A is the Alfven speed, $= B_e/(\mu_o \rho)^{\frac{1}{2}}$

r_p is the plasma radius

subscript o refers to the uniform region.

$$\left\langle \left(\frac{dr_p}{dz}\right)^2 \right\rangle = \frac{1}{L} \int_{-L/2}^{L/2} \left(\frac{dr_p}{dz}\right)^2 dz \ .$$

The growth of the instability, illustrated in Fig.2.4(c), is accompanied by a propagation of its amplitude along the plasma column away from the bulge, with a velocity $V_{m=1}$;

$$V_{m=1} = V_A \sqrt{2-\beta} \ . \qquad \ldots (2.8.5)$$

Conducting walls stabilize the motion because of the image currents produced. Experiments have found that equation (2.8.4) describes the instability growth accurately. Finite Larmor radius effects are thought to damp modes with $m \geq 2$[26].

2.9 THETA PINCH DESIGN CRITERIA

To complete this review, the criteria for producing a theta pinch of length ℓ, lifetime τ and temperature T are derived. It is assumed that a long, n turn solenoid (the thetatron) of inductance L is connected to a low inductance capacitor bank of C Farads, charged to V Volts. The current around the solenoid is then:

$$I = \sqrt{\frac{CV^2}{L}} \sin \omega t \qquad \ldots (2.9.1)$$

where

$$\omega = \frac{1}{\sqrt{LC}} \qquad \ldots (2.9.2)$$

The inductance of the solenoid is given by [36]

$$L = \frac{\mu_0 n^2 A}{\ell} \qquad \ldots (2.9.3)$$

and the axial magnetic field by [37]

$$B = \frac{\mu_0 n I}{\ell} \qquad \ldots (2.9.4)$$

where A is the cross sectional area of the solenoid. If the current oscillates sinusoidally, the half-period restricts the plasma lifetime because of the radial expansion to the vacuum vessel walls (see Fig.2.1(c)). If a lifetime τ is required, the half period must be greater than τ. Using equation (2.9.2) a restriction on the solenoid inductance is found:

$$L \geq \frac{\tau^2}{\pi^2 C} \; . \qquad \ldots (2.9.5)$$

During the time τ the plasma should be free from energy and particle losses. Axial mass flow (see Fig.2.2) imposes a minimum length on the plasma and solenoid if area waves are not to disturb the plasma midplane [15]. Then

$$\ell \geq 2 v \tau \qquad \ldots (2.9.6)$$

where

$$v = c_s \sqrt{1 - \beta} \; , \qquad \ldots (2.9.7)$$

c_s being the sound speed. Values of c_s and β must be assumed for the required plasma. Thermal conduction imposes a minimum length [10] (see Fig.2.2):

$$\ell \geq 2 \sqrt{\tau \, \lambda_{ee} v_e} \qquad \ldots (2.9.8)$$

where λ_{ee} is the electron-electron mean free path
v_e is the electron thermal velocity.

Axial mass flow dominates electron thermal conduction [10] if:

$$\frac{2\lambda_{ee}}{\ell} < \frac{v_i}{v_e} \qquad \ldots (2.9.9)$$

where v_i is the ion thermal velocity. If axial mass flow dominates, equations (2.9.3), (2.9.5) and (2.9.6) restrict the product $n^2 A$:

$$n^2 A \geq \frac{2 v \tau^3}{\mu_0 \pi^2 C} \; . \qquad \ldots (2.9.10)$$

Having chosen the parameters n, A, ℓ and C through equations (2.9.5) and (2.9.10), the resulting plasma temperature can be estimated from Mewe's formula, equation (2.4.2). With a 30% Joule heating contribution (see section 2.5) this becomes

$$k\hat{T} = \frac{800d}{3}\left(\frac{r_w \hat{B}\dot{B}_o}{p}\right)^{\frac{2}{3}} \qquad \ldots (2.9.11)$$

where the symbols and units are defined with equation (2.4.2). Substituting for $\dot{B}_o = \omega\hat{B}$, and using equations (2.9.1), (2.9.3) and (2.9.4), gives

$$\hat{T} \propto \left(\frac{r_w}{p}\,\frac{V^2}{n}\left(\frac{C}{\ell A^3}\right)^{\frac{1}{2}}\right)^{\frac{2}{3}} . \qquad \ldots (2.9.12)$$

Therefore the area A and the number of turns n should be minimised. The temperature $\hat{T}$ can be varied by changing the charging voltage V and the initial pressure p.

2.10 SUMMARY

A typical theta pinch has a temperature of 100 eV, a density of 10^{16} particles cm^{-3}, a radius of 1 cm, and a lifetime of 10 μs. The plasma is heated by an implosion, an adiabatic compression and Joule heating. During the implosion micro instabilities produce an effective collision frequency such that the shock width is less than the mean free path for binary collisions. These instabilities produce an anomalous resistivity and diffusion coefficient. The external magnetic field continues to increase after the implosion, heating both electrons and ions adiabatically.

The most important loss mechanisms are thermal conduction along the field lines, axial mass flow, impurity radiation and cross field diffusion. Thermal conduction losses impose a maximum obtainable temperature.

Bias fields are used to control the plasma temperature and beta. Negative bias fields increase the temperature and beta, while positive bias fields decrease the temperature and beta.

Rotational instabilities driven by azimuthal $\bar{j} \times \bar{B}$ forces are the most common naturally occurring mode in a theta pinch. A straight theta pinch is neutrally stable to the $m=1$ long wavelength, or kink, mode. However, a bulged theta pinch is $m=1$ unstable; the resulting displacements propagate along the field lines.

a) A THETATRON

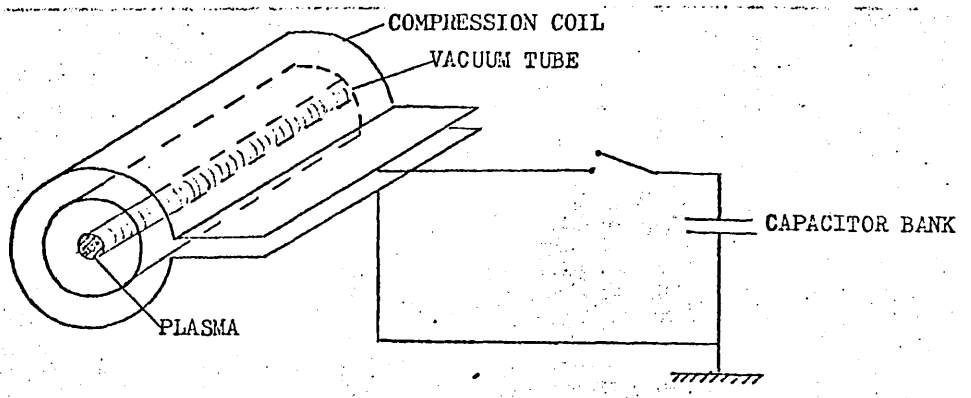

b) THE CURRENT WAVEFORMS

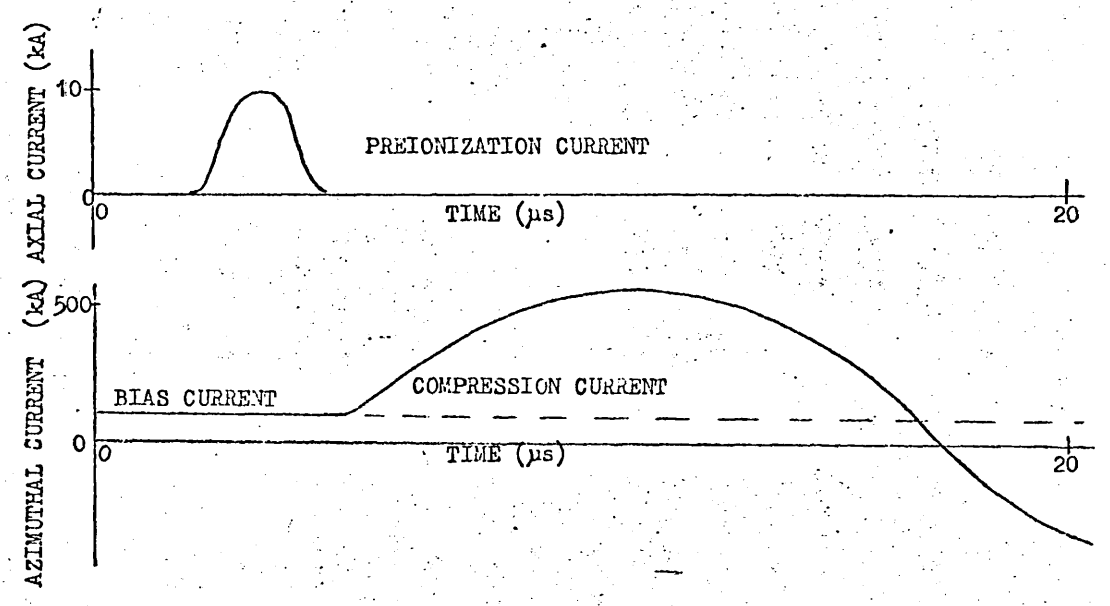

c) THE PLASMA RADIUS

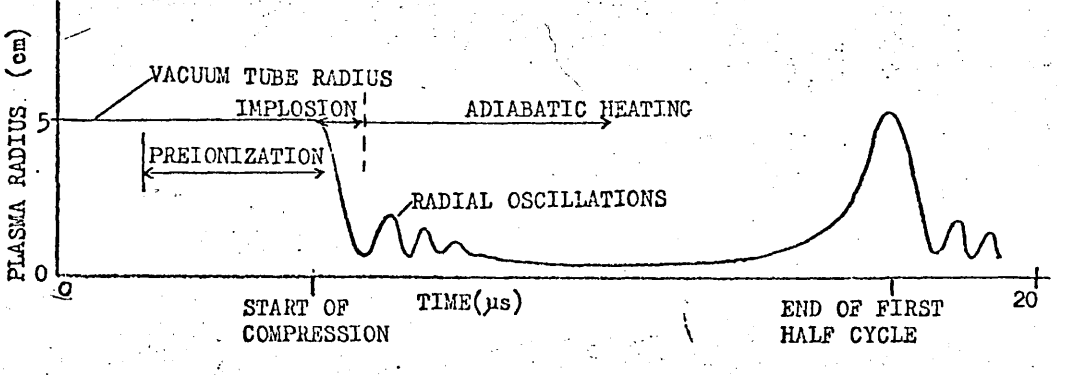

Fig.2.1
A simple theta pinch and thetatron

TYPE	PLASMA CONDITIONS	CHARACTERISTIC TIME	EFFECT	COMMENTS
DIFFUSION $\perp$ TO B (12)	PRESSURE GRADIENTS	$r_p/v_\perp$	JOULE HEATING AND A TENUOUS PLASMA	$D_\perp \sim$ BOHM DURING IMPLOSION $D_\perp \sim$ CLASSICAL AFTER IMPLOSION $v_\perp = -(\eta/B^2)\nabla p$
THERMAL CONDUCTION (10)	TEMPERATURE GRADIENTS ($\lambda_{ee} < L$)	$L^2/(\lambda_{ee} v_e)$	ELECTRON LOSS FROM THE ENDS	RESULTS IN A MAX. TEMP. $\hat{T}^{\frac{7}{2}} \propto \omega \hat{B}^2 L^2 (2-\beta)$
PARTIAL IONIZATION	LOW TEMPERATURE		ENERGY FROM SHOCK WAVE USED FOR IONIZATION	IMPORTANT FOR LOW ENERGY INPUT RATES, $\dot{B}_o \leqslant 10 kG\,\mu s^{-1}$
IMPURITY RADIATION (13)	TYPICALLY 1% O_2 (H ISOTOPES IONIZED FOR $T \geqslant 50$ eV)		COOLING	IMPORTANT FOR LOW ENERGY INPUT RATES
AXIAL MASS FLOW (80,14,15)	LOW β, HIGH TEMPERATURE	$\frac{L}{C_s\sqrt{1-\beta}}$	ION LOSS FROM PLASMA ENDS; AN AREA WAVE PROPAGATES TOWARDS THE CENTRE	DOMINATES THERMAL CONDUCTION LOSSES IF $(v_i/v_e) > (\lambda_{ee}/L)$
CHARGE EXCHANGE (16)	INCOMPLETELY IONIZED		IONS LOSE ENERGY TO NEUTRALS, WHICH ARE LOST FROM THE PLASMA	

r_p - Plasma Radius
L - Plasma Half Length
$\dot{B}_o$ - Initial Rate of Rise of Magnetic Field
D - Diffusion Coefficient
v - Thermal Velocity
λ_{ee} - Electron-Electron Mean Free Path
η - Resistivity; $\eta_B = \omega_{ce}\,\tau_{ei}\,\eta/16$
τ_{ei} - Electron-Ion Collision Time

Fig.2.2
Energy and particle losses

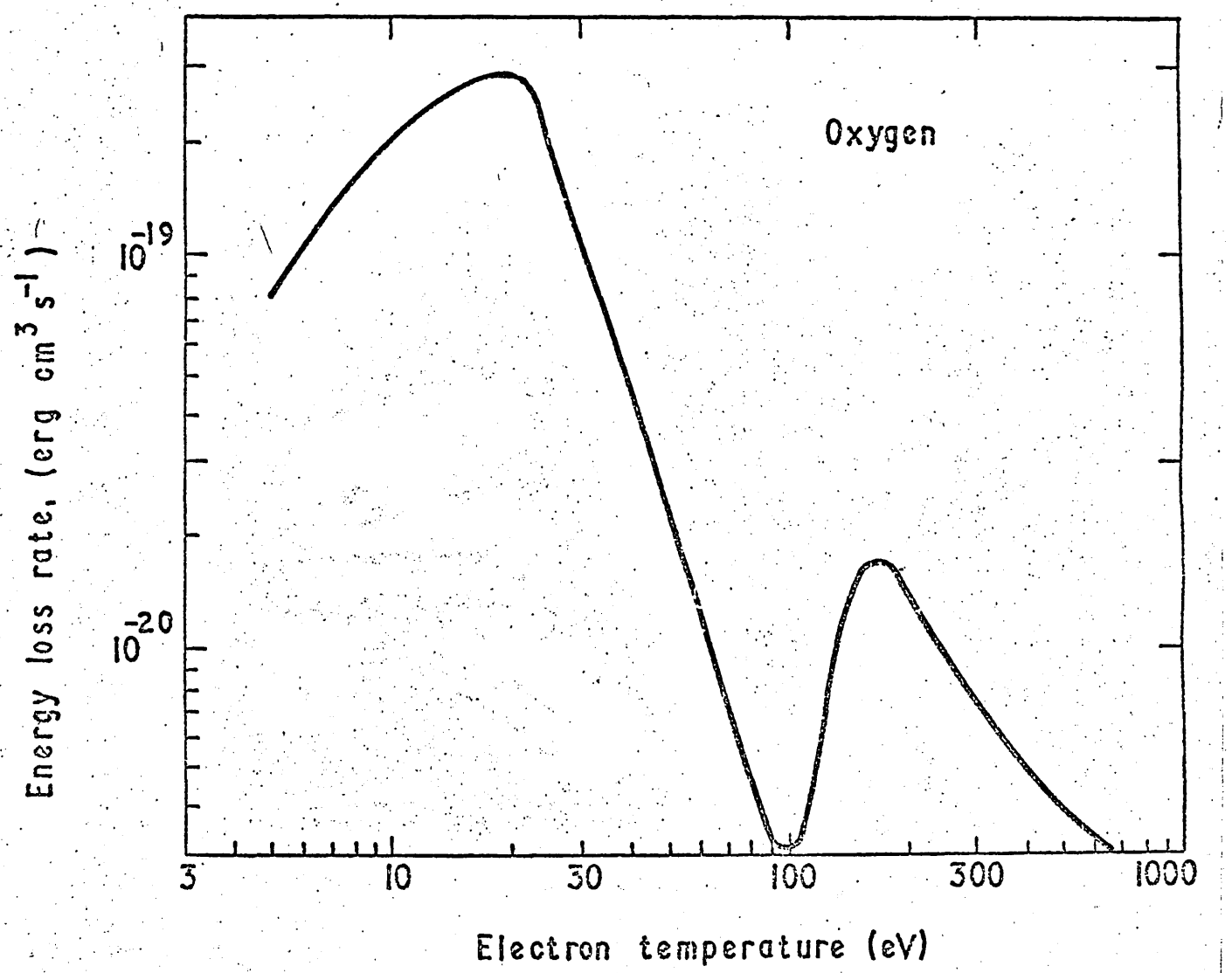

Fig.2.3

The energy loss rate due to oxygen impurities

(a) The Rotational m = 2 Instability

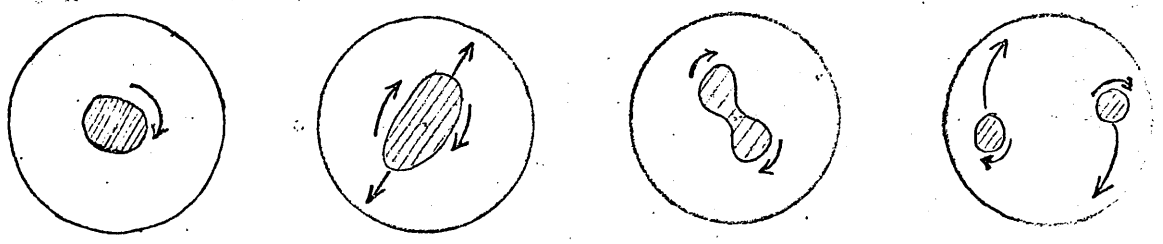

(1) ROTATING PLASMA CYLINDER IN A MAGNETIC FIELD

(2) CENTRIFUGAL FORCES ELONGATE THE CROSS SECTION

(3) PLASMA STARTS TO DIVIDE

(4) PLASMA DIVIDED, EACH HALF ROTATING TOWARDS THE WALLS

(b) The Resistive Tearing Instability

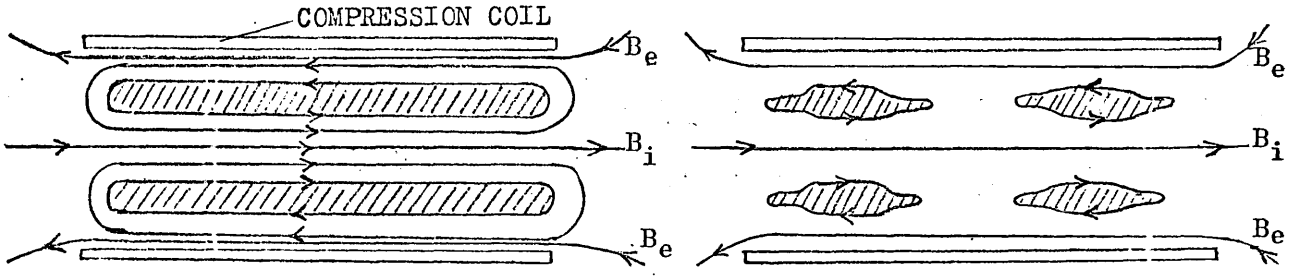

(1) CLOSED FIELD LINES AT THE ENDS OF A REVERSE (NEGATIVE) BIAS THETA PINCH CAUSE AXIAL CONTRACTION

(2) IF B = 0 WITHIN THE PLASMA AND THE RESISTIVITY $\neq$ 0, FIELD LINES CAN CLOSE ANYWHERE AND PRODUCE PLASMA RINGS

(c) The Long Wavelength m = 1 Instability

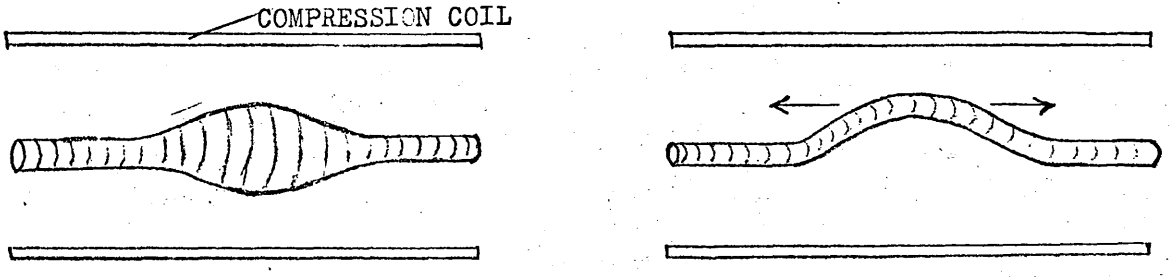

(1) A BULGED PLASMAS IS PRODUCED IN A $\sim$ 1 = 0 MAGNETIC FIELD

(2) A KINK- OR m = 1 INSTABILITY DEVELOPS, WHICH PROPAGATES ALONG THE PLASMA

Fig.2.4

Some MHD instabilities commonly found in theta pinch plasmas

CHAPTER III

THE 3.5 m THETATRON

3.1 INTRODUCTION

Most of the experiments to be reported were performed on a 3.5 m long thetatron, which is now described. The azimuthal and axial current circuits, the bias field circuit and the vacuum system are described. The distinctive features are discussed, in particular the series turns compression coil and the small azimuthal electric field produced. A 2 m long thetatron used for preliminary experiments on perturbed plasma motion is compared with the 3.5 m thetatron, and the main differences emphasised.

3.2 THE AZIMUTHAL CURRENT CIRCUIT

A compression coil (see section 2.2) was designed, using the criteria presented in section 2.9, to produce a plasma with a temperature of up to 50 eV, free from end effects (see section 2.6 and Fig.2.2) at the midplane for 15 μs. Seven series turns were used, each turn being 50 cm long and having an internal radius of 6.5 cm. Fig.3.1 is a photograph of the machine. Fig.3.2 shows a front view, plan and cross section. Each of the 7-turns was interconnected by a diagonal tab (see Fig.3.2(b)), which helped to produce a smooth current distribution in the coil[38].

Unwanted transverse magnetic fields were reduced by including a flux guide (see Fig.3.2(a)). This consisted of two cylindrical aluminium alloy tubes, each 1.6 m long and 0.8 cm thick, split longitudinally at the tab side (see Fig.3.2(c)). Each section was electrically connected to the compression coil centre turn. Axial magnetic fields could penetrate the flux guide. Azimuthal fields were theoretically reduced to a value on axis of 0.05% of the value outside the guide[39].

Both the compression coil and flux guide were machined with 180°, 0.5 cm wide optical viewing slots (see Fig.3.2(a)). The compression coil centre turn had slots every 4 cm; these were not expected to significantly perturb the axial field[40]. The volume between the vacuum tube and the centre turn was available for diagnostic probes and a sector loop, which was used to excite plasma motion (see Chapter VII).

An 84 μF capacitor bank, with a maximum charging voltage of 45 kV, was connected to the compression coil by 56 parallel cables and 14 parallel spark gaps, which were triggered by a Blumlein generator. The earth return was placed between the diagonal tab system (see Fig.3.2(c)), and connected to a copper earth mat.

The oscillating I_θ current waveform was used to determine the total circuit impedance (see section A2.3). Values of inductance and resistance obtained were

$$L_T = 330\,\text{nH}$$
$$R_T = 5\,\text{m}\Omega\,.$$

The inductance L_θ of the 7-turn compression coil was estimated using equation (2.9.3), where the cross sectional area A was taken as the coil area minus the flux guid area:

$$L_\theta = 190\,\text{nH}\,.$$

Fig.3.3(b) illustrates the electrical circuit. The external inductance L_E was accounted for by the inductances of the tabs, earth return plate, connecting cables, spark gaps and capacitors.

With the capacitor bank charged to 45 kV the maximum current measured was 690 kA, reached in 8.3 μs (see section A2.3). Using equation (2.9.4) the maximum axial field was calculated as 17.5 kG. This value was confirmed by search coil measurements (see section A2.4).

3.3 THE VACUUM SYSTEM

A cylindrical quartz tube, internal radius 4.3 cm and external radius 4.7 cm, was supported inside the flux guide (see Fig.3.2(a)). The tube interior was sand blasted at positions opposite the viewing slots, and the exterior 180° opposite the slots covered with black paper. These precautions reduce optical plasma reflections, which can complicate optical diagnostics[41].

A rotary pump, a mercury diffusion pump and a nitrogen trap were used to obtain base pressures of 5×10^{-7} torr, with leak rates of 5×10^{-4} mtorr litres s^{-1}. Deuterium was introduced into the system through a heated nickel leak. Gas pressures were measured using Pirani and ionization gauges.

3.4 THE PRE-IONIZATION CIRCUIT

A 0.75 μF, 40 kV capacitor was discharged axially through the gas for pre-ionization. The oscillating current was either diverted at current zero with a spark gap switch, or the circuit critically damped, to produce a single current pulse of 7 μs duration and 10 kA amplitude. Eight pre-ionization current return bars were used, placed symmetrically about the compression coil (see Fig.3.2(a) and (c)). A pre-preionization spark gap was mounted in the earth disc (see Fig.3.2(a)) to reduce the gas breakdown time; this was connected to the positive terminal of the pre-ionization system. Fig.3.2(b) illustrates the electrical network.

3.5 THE BIAS FIELD CIRCUIT

A 190 μF capacitor bank was discharged into the compression coil through a 2.7 μH isolating inductance, to produce a bias field with a period of 150 μs and a peak amplitude of ±1.4 kG (see section 2.7). If the bias bank was triggered about 35 μs before the main azimuthal current, the resulting bias field could be considered a constant over the plasma

lifetime. The isolating inductance reduced the peak axial magnetic field from 17.5 kG to 17 kG. Fig.3.3(a) tabulates the main parameters of the azimuthal (theta) current, the preionization (axial) current, and the bias field, circuits.

3.6 THE DISTINCTIVE FEATURES

Using a series turn compression coil allows the length and inductance of the coil to be increased simultaneously above normal values, typically 2 m and 10 nH. Efficient energy transfer from the capacitor bank to the long plasma can then be obtained without a carefully designed low inductance bank.

The initial rate of rise of axial magnetic field, $\dot{B}_0$, was ≤ 3.3 kG μs^{-1}, corresponding to an azimuthal electric field at the vacuum tube wall of $E_\theta \leq 70$ V cm^{-1} (see equation (2.3.1)). The plasma temperature is a function of E_θ (see equation (2.9.11)); most thetatrons operate with E_θ between 200 V cm^{-1} [42] and 600 V cm^{-1} [43]. Using equation (2.9.11) and a computer code (see Chapter V), peak temperatures of 50 eV were predicted.

3.7 THE 2 m THETATRON [44]

This machine, similar to the 3.5 m thetatron, was built with a 7 series turn compression coil, 2 m long. Each turn was interconnected by straight tabs, as opposed to diagonal tabs on the 3.5 m thetatron. A flux guide was not included, so that transverse field components were expected.

The compression coil was connected to a 60 μF capacitor bank, which was charged to 35 kV. A peak axial field of 14 kG, with a quarter period of 9 μs, resulted.

Preionization was performed by a clamped axial discharge of 10 kA over 6 μs. The vacuum system was similar to the 3.5 m thetatron system (see section 3.3). Fig.3.3(c) summarises the main electrical parameters of the azimuthal and the axial current circuits.

Fig.3.1 The 3.5m thetatron

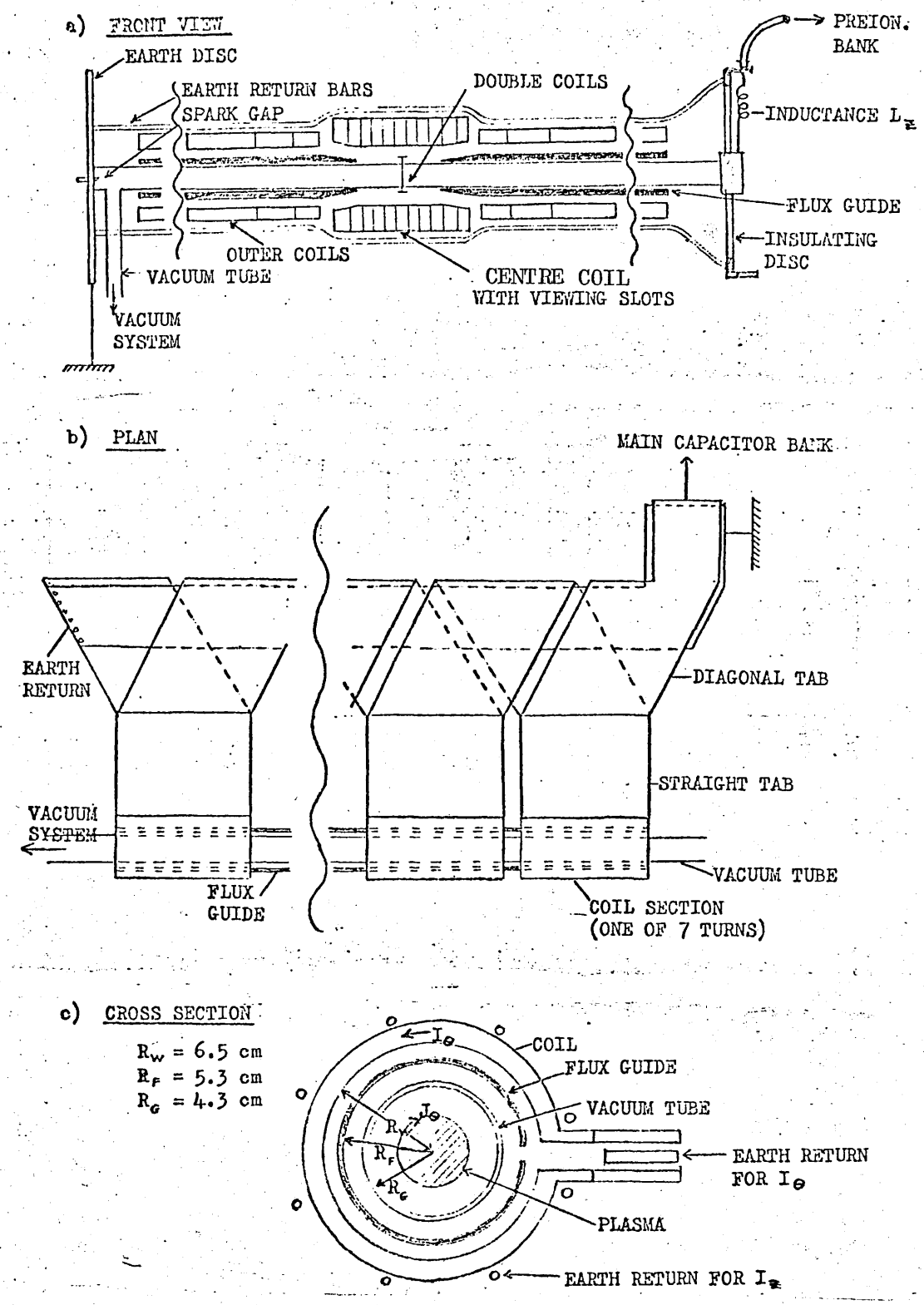

Fig.3.2
A schematic diagram of the 3.5 m thetatron

(a) The 3.5 Thetatron Bank Parameters

CIRCUIT	CAPACITANCE (μF)	ENERGY (kJ)	CURRENT (kA)	FIELD (kG)	PERIOD (μs)
THETA	C_θ = 84	85	690	17.5	33
BIAS	C_B = 190	6	50	± 1.4	150
PREION.	C_z = 0,75	0.6	10		14

(b) The 3.5 m Thetatron Circuit

A AZIMUTHAL CURRENT CIRCUIT (I_θ)

B AXIAL CURRENT CIRCUIT (I_z)

L_B = 2.7 μH
L_θ = 0.19 μH
L_z = 7.0 μH
L_E = 0.14 μH

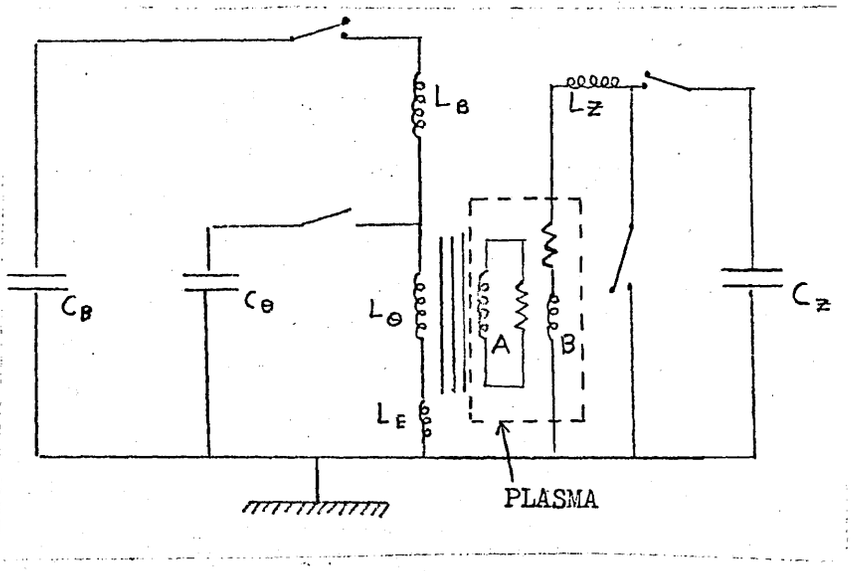

(c) The 2 m Thetatron Bank Parameters

CIRCUIT	CAPACITANCE (μF)	ENERGY (kJ)	CURRENT (kA)	FIELD (kG)	PERIOD (μs)
THETA	C_B = 60	36.5	320	14	36
PREION.	C_z = 0.75	0.6	10		12

Fig.3.3
The electrical parameters

CHAPTER IV

AN INVESTIGATION OF THE HEATING MECHANISMS IN A THETA PINCH

4.1 INTRODUCTION

The experiments to determine the effect of the initial conditions on the 3.5 m theta pinch plasma characteristics are described[59]. Preliminary experiments were aimed at producing a hot, reproducible, MHD stable plasma for the perturbed motion studies (see Chapter VII). The results are compared with the predictions of a computer code in Chapter V.

The experimental procedure is described, and the results of varying the bias field, gas filling pressure, preionization to compression current delay time and the rate of change of external magnetic field are presented. Measurements of the plasma diamagnetism, line mass, electron density profile, beta and temperature were made; details of the diagnostic techniques are given in Appendix A.2. The optimum initial conditions for achieving a hot, stable plasma were determined.

4.2 THE EXPERIMENTAL PROCEDURE

The vacuum tube of the 3.5 m thetatron (see Chapter III) was degassed by repeated discharges (see Section 2.6.3). Purified deuterium gas was used for the experiments. Each plasma produced was photographed with a streak camera through a 0.5 cm wide slit in the compression coil centre turn (see Section A.2.6), and the diamagnetism recorded 1 cm from this slit (see Section A2.8). From the resulting information the average temperature (see Section A2.10), average beta, written $\langle\beta\rangle$ (see Section A2.10), electron density (see Section A2.7), line mass (see Section A2.9) and radius (see Section A2.10) were deduced. A typical set of current waveforms, diamagnetic signal and streak photograph is shown in Fig.4.2(b). Fig.4.3 shows a typical intensity and radial electron density profile.

The initial conditions varied were :

(1) The capacitor bank voltage. This controlled the external magnetic field B_e, and the initial rate of change of the external magnetic field, $\dot{B}_0$.

(2) The bias field B_1.

(3) The filling pressure p.

(4) The delay τ_{pI} between the axial preionization current and the azimuthal current. τ_{pI} was defined as the time between the preionization current zero and the start of the azimuthal current; negative value of τ_{pI} were produced by triggering the main capacitor bank before the preionization current had reached zero.

A limited scan of the variables, with the emphasis on determining the dependence of the plasma temperature on the initial conditions, was performed. Experiments showed that the line mass was a function of p and $\dot{B}_0$ only (see section 4.4.6). The average temperature, derived from the diamagnetic signal (see equation A2.22), can be written

$$T_{Av} \propto \frac{SB\langle\beta\rangle}{M(1-\sqrt{1-\langle\beta\rangle}} \qquad \ldots (4.2.1)$$

where S is the diamagnetism, M is the line mass. Changing $\langle\beta\rangle$ from 0 to the maximum value of 0.5 (see equation A2.17) decreases T_{Av} by 15%. Therefore for constant M and B the temperature is approximately proportional to the diamagnetism. Therefore for constant p and $\dot{B}_0$ the optimisation of bias B_1 and delay τ_{pI} for the maximum temperature was performed as an optimisation for maximum diamagnetism.

4.3 THE EXPERIMENTAL ERRORS

When one observation was made for a particular set of conditions, the errors were taken as the percentage errors given in Appendix A2 and summarised in Fig.A2.2. When a number of observations was made for the same initial conditions, the most probable error, r, was used[57] :

$$r = 0.85 \frac{\sum_i |x_i|}{n\sqrt{n-1}} \qquad \ldots (4.3.1)$$

where x_i is the deviation of the i^{th} observation from the mean

n is the number of observations.

Error bars indicate the most probable error. Otherwise percentage errors must be assumed.

4.4 THE EXPERIMENTAL RESULTS

4.4.1 Varying the Pressure

The deuterium gas filling pressure was varied between 10 mtorr and 50 mtorr, and the diamagnetism recorded at 4 μs and 8 μs after the start of the main azimuthal current I_θ. The other variables were set to

$$\tau_{pI} = 0 \ \mu s;$$
$$B_1 = 0 \ kG;$$
$$\dot{B}_0 = 2.9 \ kG \ \mu s^{-1}.$$

The maximum diamagnetism occurred for $20 \leqslant p \leqslant 50$ mtorr. Above 30 mtorr the plasma was diffuse. Below 20 mtorr the streak photographs showed a plasma wobble of about 0.5 cm [58]. Below 10 mtorr the gas breakdown became erratic. A working pressure of 30 mtorr was chosen.

4.4.2 Varying the Preionization

The preionization to main azimuthal current delay, τ_{pI}, was varied between -3 μs and $+20$ μs, with the other variables:

$$p = 30 \text{ mtorr};$$
$$B_1 = 0 \ kG;$$
$$\dot{B}_0 = 2.2 \text{ to } 3.3 \ kG \ \mu s^{-1}.$$

For all the values of $\dot{B}_0$ used, the diamagnetism, recorded at 4 μs and 8 μs, was a maximum when τ_{pI} was -2 μs; that is, when the azimuthal current was initiated before the preionization current was zero. With $\tau_{pI} < -2$ μs

the streak photographs showed an asymmetric implosion followed by an $m=1$ instability (see Section 2.8.4). Plasma rotation (see Section 2.8.2), deduced from stereoscopic streak photographs, was observed with $\tau_{pI} \leqslant -2\,\mu s$ and $\dot{B}_0 \leqslant 2.2\,kG\,\mu s^{-1}$.

When τ_{pI} was increased, the plasma became diffuse and the diamagnetism decreased; for constant $\dot{B}_0$ this decrease was equivalent to a decrease in temperature (see Section 4.2). Fig.4.1 illustrates the dependence of diamagnetism on τ_{pI} and $\dot{B}_0$. With $\dot{B}_0 = 3.3\,kG\,\mu s^{-1}$ the diamagnetism, and therefore the temperature, varied strongly for $-2 < \tau_{pI} < 2\,\mu s$. As $\dot{B}_0$ was decreased the diamagnetism was found to be less dependent on τ_{pI}; with $\dot{B}_0 = 2.6\,kG\,\mu s^{-1}$ and $\tau_{pI} \geqslant 4\,\mu s$ the plasma was cold. Two values of τ_{pI} were chosen for further experiments; $\tau_{pI} = 0$ and $-2\,\mu s$.

4.4.3 The Effect of Bias Field on the Preionized Plasma

It was found that the bias field, present in the gas before preionization, altered the gas breakdown time[20] (see Section 2.7). Fig.4.2(a) shows two streak photographs of the preionized gas, one with a bias field of $-350\,G$ and one with no bias field. With no bias field the z pinch preionization produced a plasma implosion to the axis in $0.6\,\mu s$, followed by an expansion to the vacuum tube walls after a further $2\,\mu s$. When a bias field was applied the rapid contraction and expansion were not observed, and the light intensity was more uniform.

4.4.4 Varying the Bias Field (negative)[59]

The bias field B_1 was varied between 0 and $-1\,kG$, with

$p = 30$ mtorr;

$\tau_{pI} = 0$ and $-2\,\mu s$;

$\dot{B}_0 = 2.2$ to $3.3\,kG\,\mu s^{-1}$.

Fig.4.2(b) shows a typical set of current waveforms, diamagnetic signal and a streak photograph. Fig.4.3 shows an intensity profile and the resulting

radial electron density profile at $4\,\mu s$, for $\tau_{pI} = 0\,\mu s$, $\dot{B}_o = 2.9\,kG\,\mu s^{-1}$ and $B_1 = 0$. Fig.4.4 shows an intensity profile at $4\,\mu s$ for $\tau_{pI} = 0\,\mu s$, $\dot{B}_o = 2.9\,kG\,\mu s^{-1}$ and $B_1 = -1\,kG$. In this case the trapped negative flux produced a hollow profile (see Section 2.7). For $B_1 > -500\,G$ hollow profiles were not observed after $4\,\mu s$, implying that the trapped negative flux diffused out of the plasma. For $B_1 < -500\,G$ the streak photographs showed a rapid radial expansion after $4\,\mu s$; a corresponding increase in the diamagnetism was observed. This radial expansion was assumed to be caused by the joining of the internal and external field lines (see Section 2.7), which produces an axial plasma contraction.

Fig.4.5 shows the diamagnetism at 4.0 and $8.0\,\mu s$ as a function of $\dot{B}_o$ and B_1, for $\tau_{pI} = 0\,\mu s$. The diamagnetism decreased as $\dot{B}_o$ was decreased; this was not necessarily associated with a temperature decrease because of the dependence of line mass M on $\dot{B}_o$. Similar results were obtained with $\tau_{pI} = -2\,\mu s$, but the diamagnetism was larger.

Using equations A2.21 and A2.22, with measured values of plasma radius and line mass (see Section 4.4.6), the diamagnetism was interpreted as values of $\langle\beta\rangle$ and average temperature T_{Av}. Fig.4.6 shows the derived values of $\langle\beta\rangle$ at $4\,\mu s$ and $8\,\mu s$ as a function of B_1 and τ_{pI}, with $\dot{B}_o = 3.3\,kG\,\mu s^{-1}$. Negative bias fields increased $\langle\beta\rangle$, especially for $\tau_{pI} = 0\,\mu s$. A similar increase in $\langle\beta\rangle$ was found for $\dot{B}_o < 3.3\,kG\,\mu s^{-1}$.

4.4.5 Varying the Bias Field (positive)

The bias field was varied between 0 and 500 G, with

$$p = 30\,mtorr;$$

$$\tau_{pI} = 0 \text{ and } -2\,\mu s;$$

$$\dot{B}_o = 3.3\ kG\,\mu s^{-1}.$$

Using the same procedure as described in Section 4.4.4, values of average temperature T_{Av} were derived. Fig.4.7 shows the dependence of T_{Av} at

$4\,\mu s$ on the bias field B_1 (positive and negative) and τ_{pI}, with $\dot{B}_0 = 3.3\,kG\,\mu s^{-1}$. For $\tau_{pI} = -2\,\mu s$, negative bias fields increased T_{Av} and positive bias fields decreased T_{Av}. For $\tau_{pI} = 0\,\mu s$, negative bias fields sharply increased T_{Av}. Positive bias fields $B_1 \leqslant 200$ G increased T_{Av}, but $B_1 \geqslant 200$ G decreased T_{Av}. With $|B_1| \geqslant 250$ G, T_{Av} was independent of τ_{pI}. The two computational curves on Fig.4.7 are explained in Section 5.3.4.

Heating rates, $\dot{T}_{Av}$, defined as the increase in average temperature over the first $4\,\mu s$, were calculated as functions of $\dot{B}_0$, B_1 and τ_{pI}. The results, plotted in Fig.4.8, show that $\dot{T}_{Av}$ increased as $\dot{B}_0$ was decreased. The heating rates for a plasma with a ± 500 G bias field were independent of τ_{pI}. Although the diamagnetism decreased with decreasing $\dot{B}_0$ (see Fig.4.5), the change in line mass (see Section 4.4.6) dominated the calculations.

4.4.6 The Effect of the Initial Conditions on the Line Mass

The line mass, obtained from the radial mass oscillation frequency (see Section A2.9), was calculated as a percentage of the initial filling mass. Fig.4.9 illustrates the resulting mass collection percentage as a function of $\dot{B}_0$ and p. For both 20 mtorr and 30 mtorr the mass collection decreased with decreasing $\dot{B}_0$. Bias fields $|B_1| \leq 500$ G did not affect the results; nor did changing τ_{pI} from $-2\,\mu s$ to $+15\,\mu s$.

4.5 SUMMARY

Preliminary experiments with no bias field and a preionization to main azimuthal current delay $\tau_{pI} = 0\,\mu s$ produced a plasma with an average temperature $T_{Av} = 24$ eV and an average beta $\langle\beta\rangle = 0.2$ after $4\,\mu s$. The plasma parameters were strongly dependent on the initial conditions; decreasing τ_{pI} by $2\,\mu s$ to $-2\,\mu s$ increased T_{Av} to 44 eV and $\langle\beta\rangle$ to 0.4. Both these plasmas were MHD stable and reproducible for at least $15\,\mu s$.

Small negative bias fields $B_1 \simeq -200\,G$ increased the temperature and reduced the critical dependence on the initial conditions. Values of $\langle\beta\rangle \simeq 0.5$ were obtained. The plasmas produced using $\tau_{pI} = -2\,\mu s$, or $\tau_{pI} = 0\,\mu s$ and $B_1 \simeq -350\,G$, were suitable for the perturbed plasma motion experiments (see Chapter VII).

Small positive bias fields $B_1 \leqslant 200\,G$ increased the average temperature for $\tau_{pI} = 0\,\mu s$. With $\tau_{pI} = -2\,\mu s$ positive bias decreased the average temperature. Larger values of positive bias decreased the temperature for all values of τ_{pI}.

The percentage of the filling mass collected in the plasma decreased with decreasing external magnetic field; with $\dot{B}_0 = 2.2\,kG\,\mu s^{-1}$ and a filling pressure of 30 mtorr only 13% of the mass was collected.

The heating rate decreased with increasing $\dot{B}_0$. A value of $\dot{B}_0 \simeq 3\,kG\,\mu s^{-1}$ was found below which the heating rate increased and the line mass decreased.

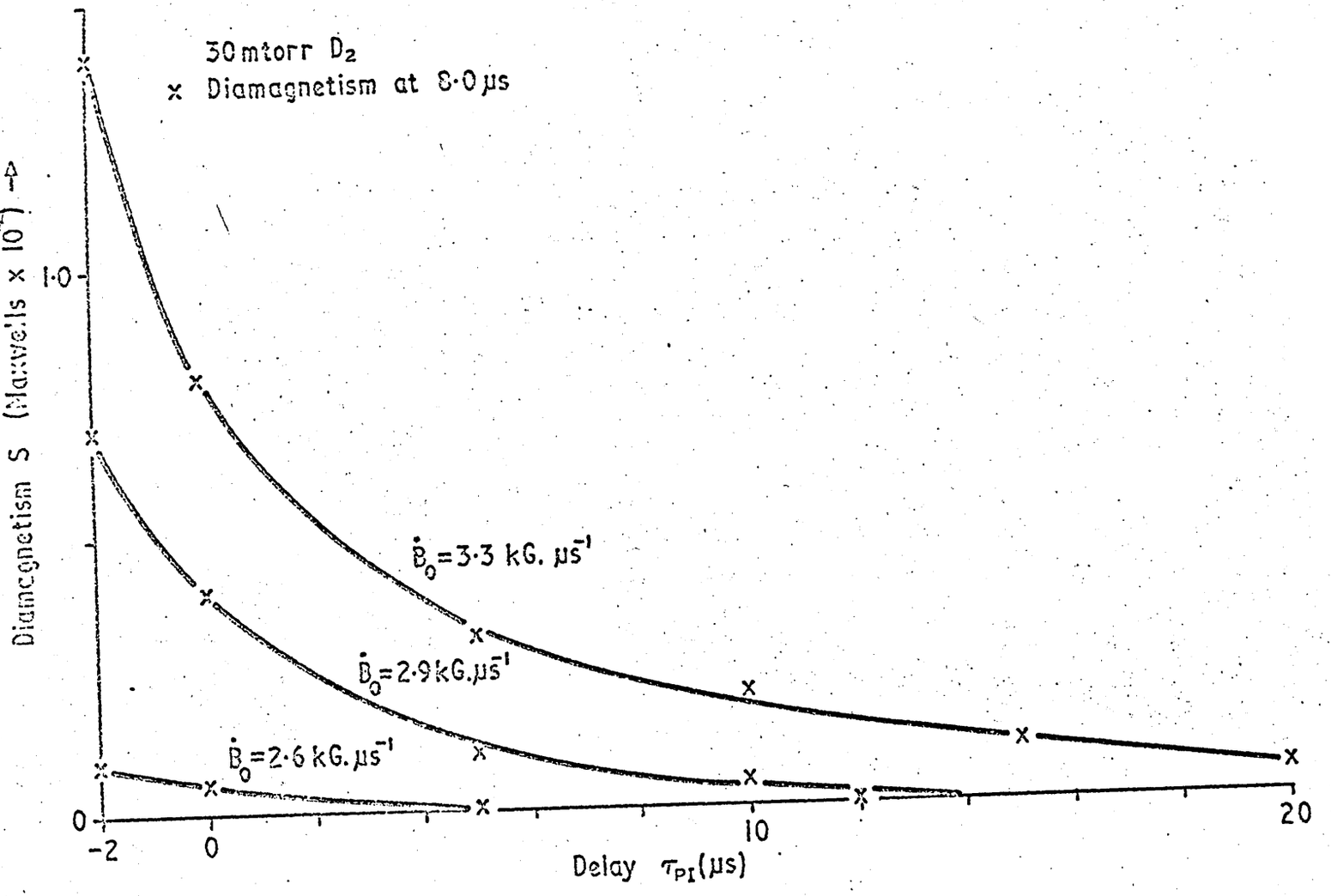

Fig.4.1

The diamagnetism as a function of $\dot{B}_0$ and τ_{pI}

a) THE EFFECT OF BIAS FIELDS ON THE PREIONIZED GAS

30 mtorr D_2, NO BIAS

30 mtorr D_2, BIAS = -350 G

Fig.4.2

b) TYPICAL DATA FROM THE HEATING EXPERIMENTS

PRESSURE = 30 mtorr D_2
$\dot{B}_\theta$ = 3.3 kG.μs^{-1}
BIAS B_z = -350 G

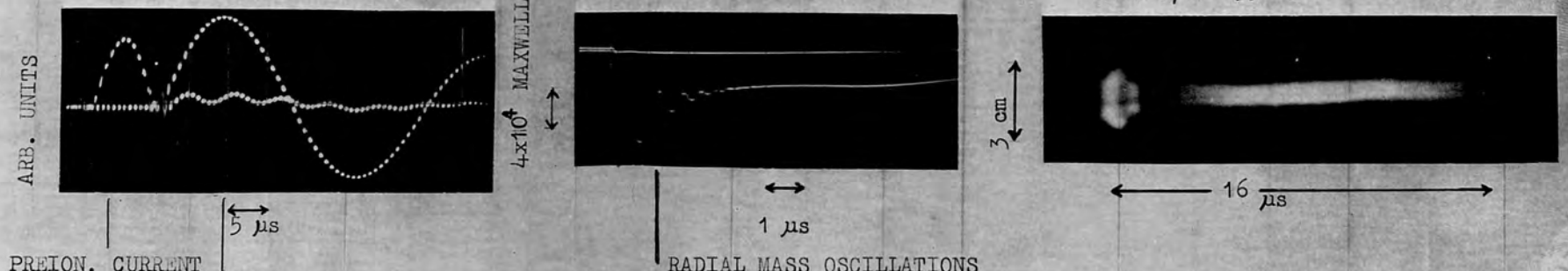

CURRENT WAVEFORMS

DIAMAGNETIC SIGNAL

STREAK PHOTOGRAPH

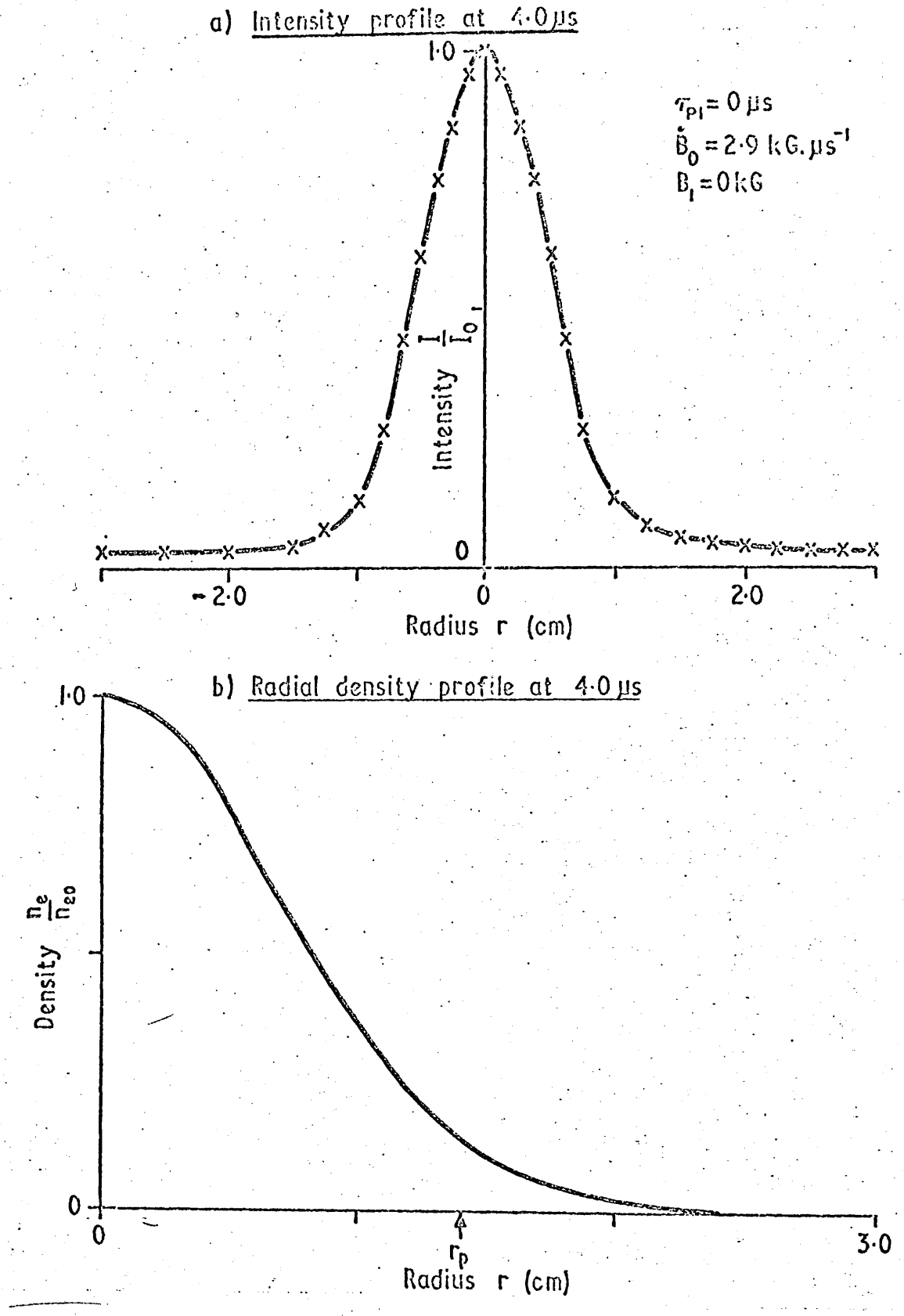

Fig.4.3

The intensity and electron density profiles with no bias field

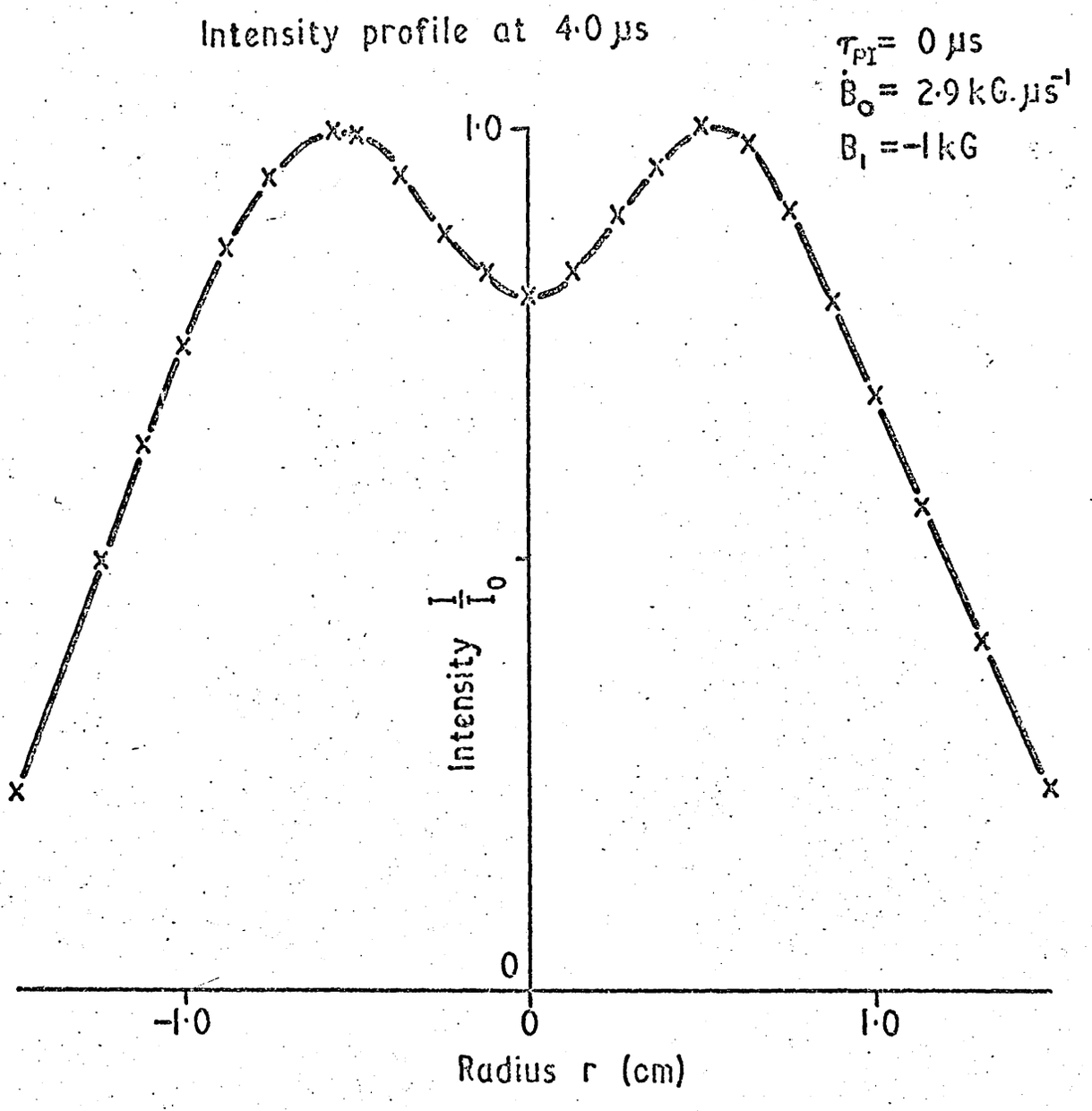

Fig.4.4

The intensity profile with a negative bias field

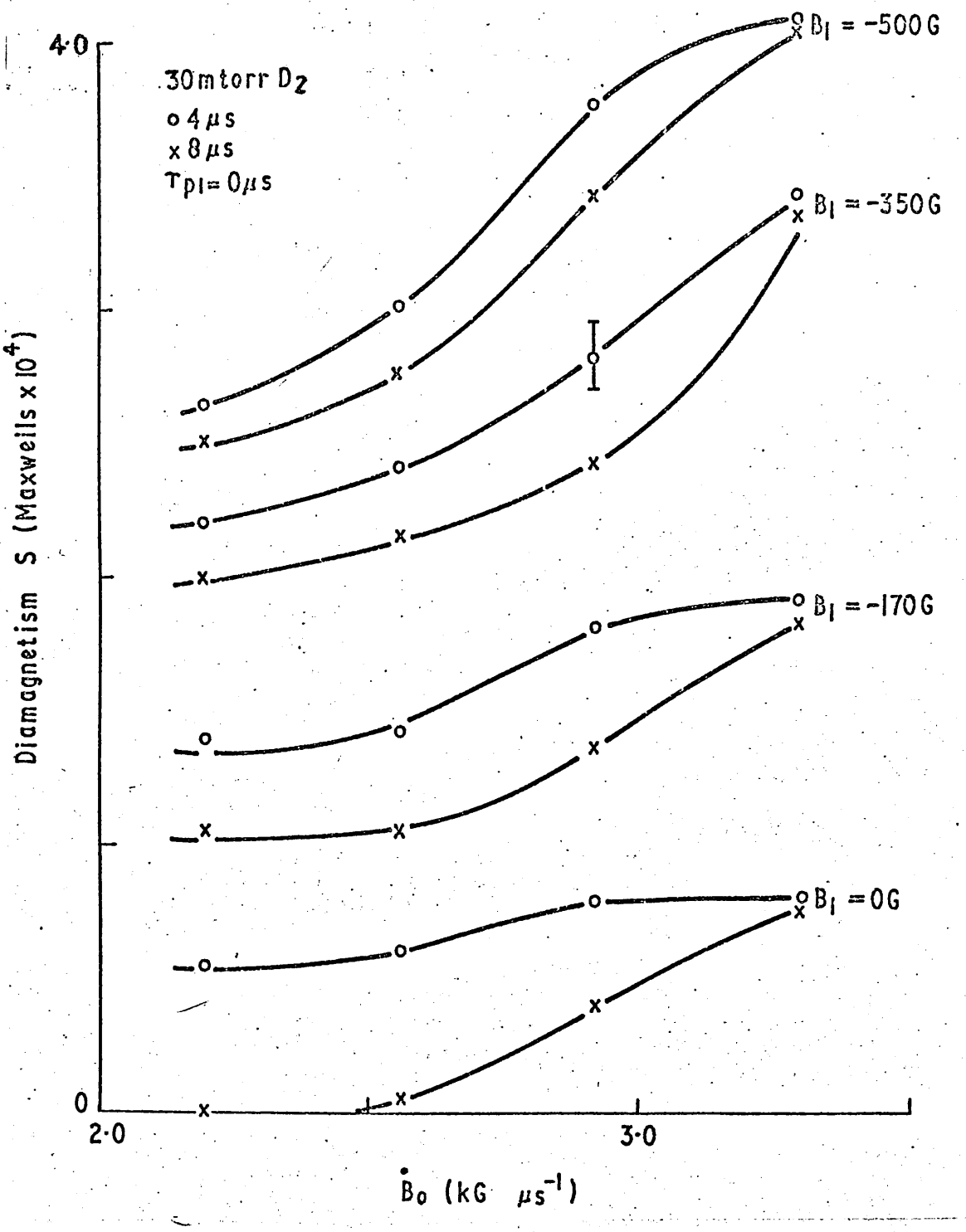

Fig.4.5

Diamagnetism against bias field and initial rate of rise of external field

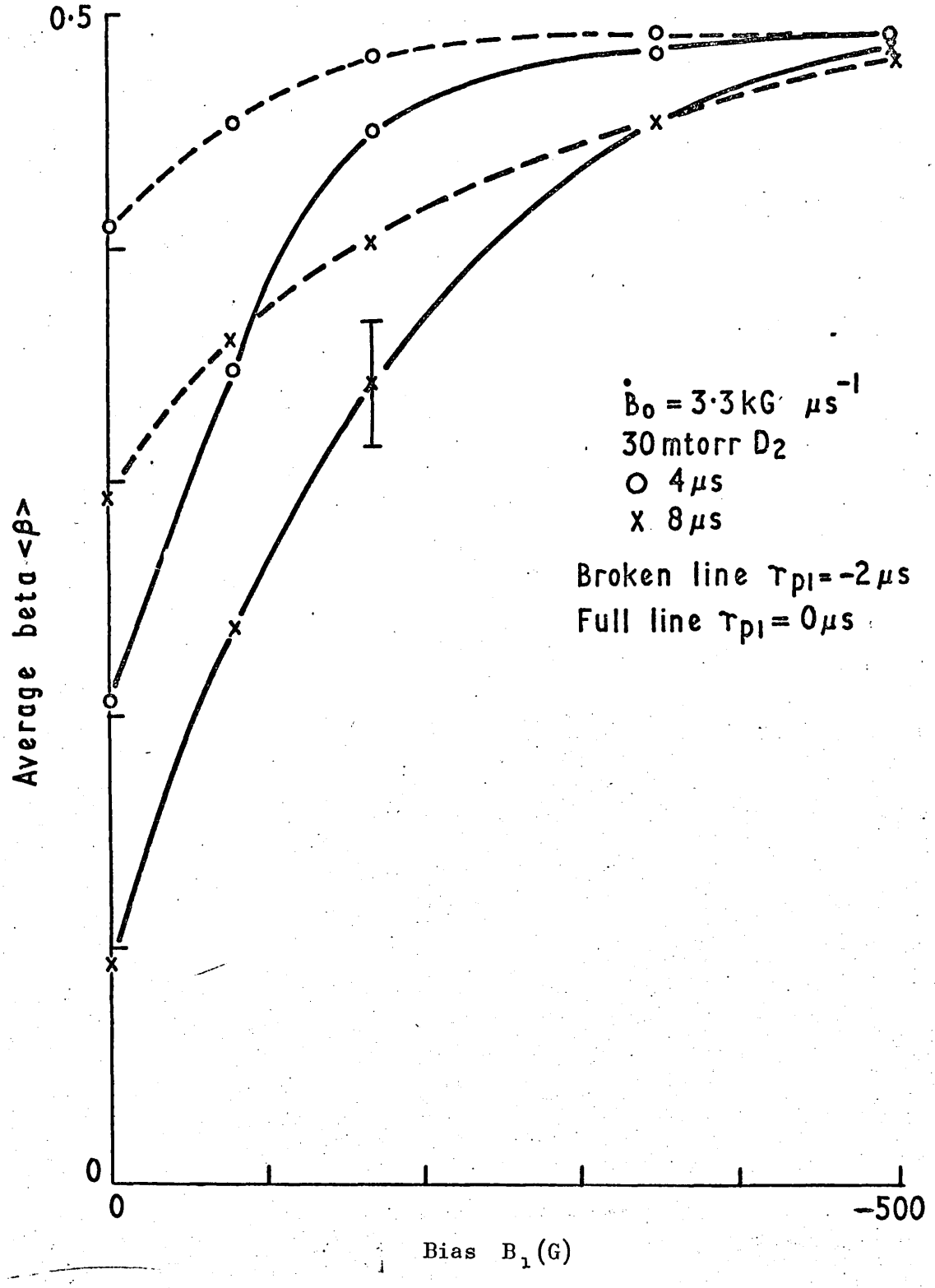

Fig.4.6
⟨β⟩ as a function of bias field and delay τ_{pI}

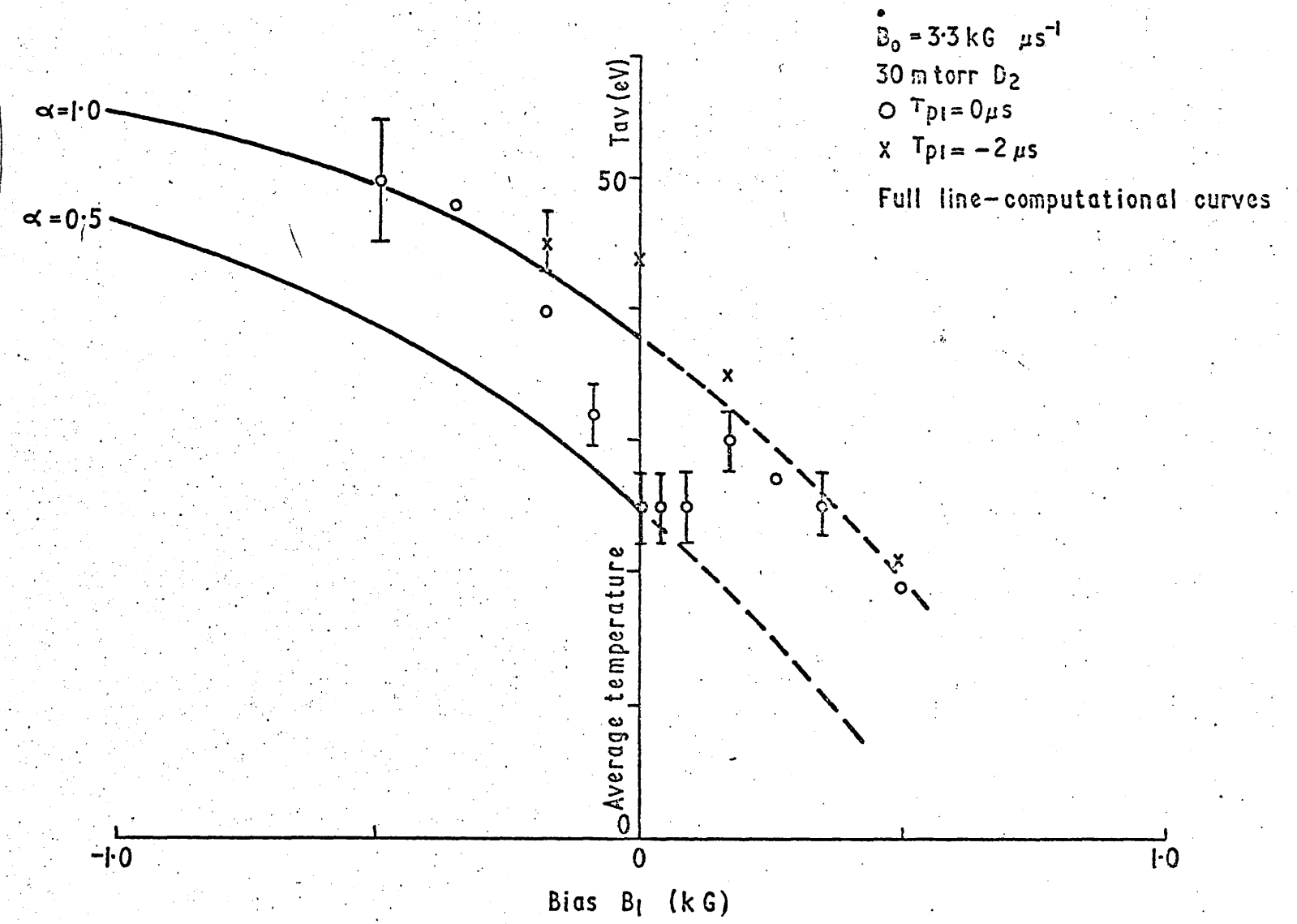

Fig.4.7

The temperature as a function of bias field and delay τ_{pI}

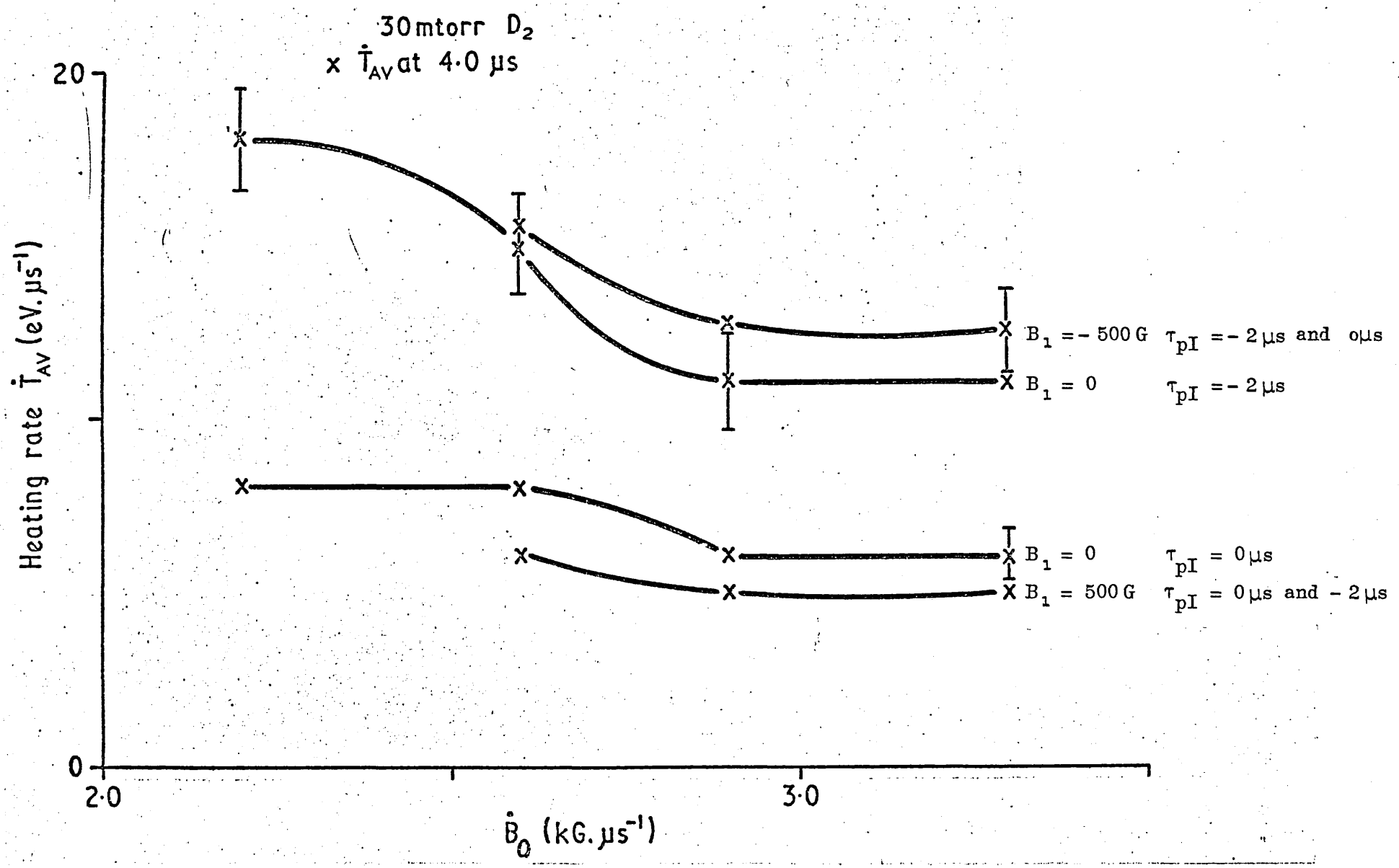

Fig.4.8

Heating rate against initial rate of rise of external field

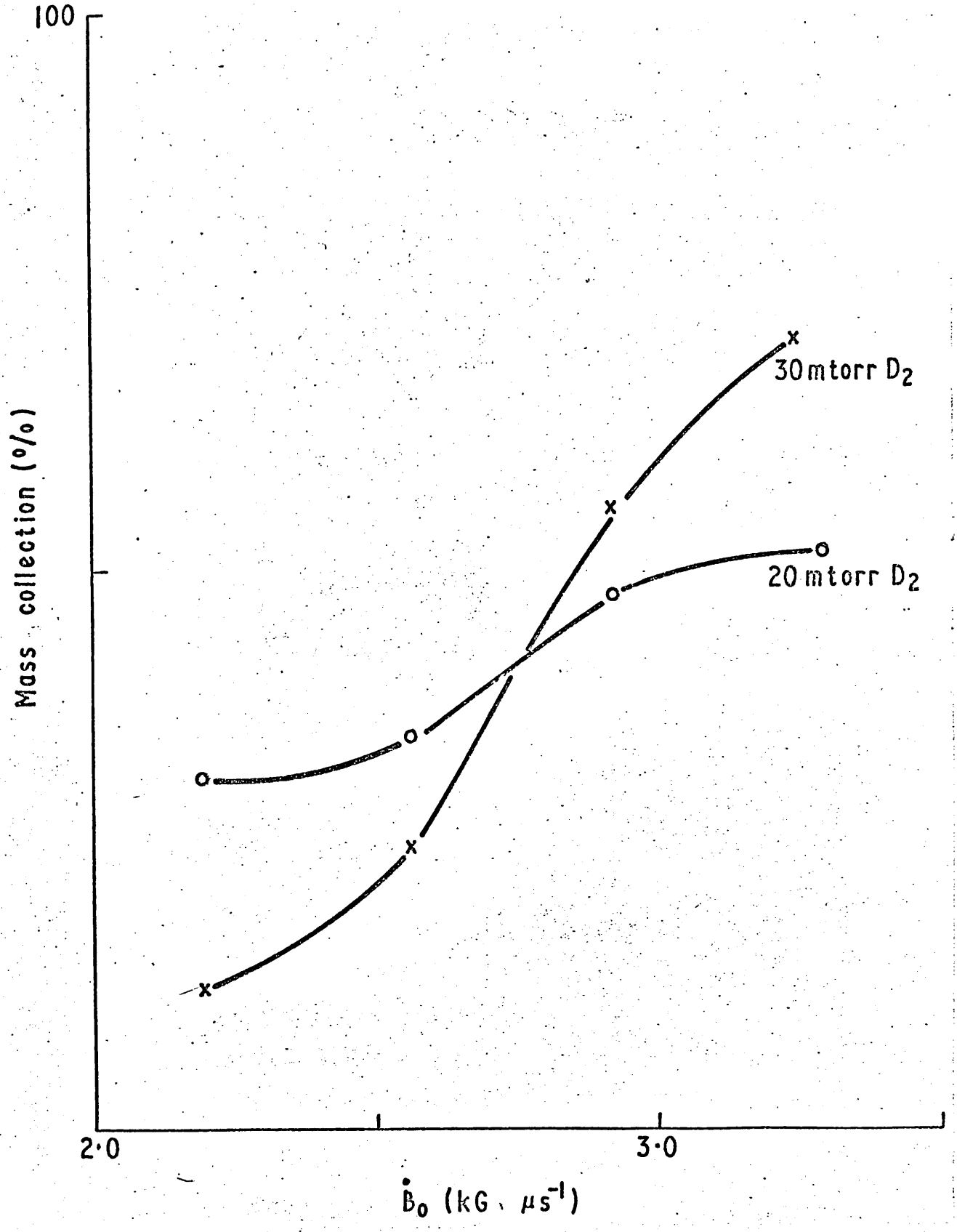

Fig.4.9

Mass collection against pressure and initial rate of rise of external field

CHAPTER V

A COMPARISON BETWEEN THE EXPERIMENTAL HEATING RESULTS AND THE PREDICTIONS OF A COMPUTER CODE

5.1 INTRODUCTION

The predictions of a computer code which simulated the heating and energy loss processes present in a theta pinch are described. A description of the code is given, followed by the computed results of varying the ionization coefficient and impurity content of the preionized gas, and the bias field. These results include a relationship between the heating rate and the initial rate of rise of external magnetic field, $\dot{T} \propto \dot{B}_0^{\frac{3}{2}}$, which agrees with experimental results.

The experimentally observed dependence of temperature on the bias field and preionization to main azimuthal current delay (see Chapter IV) is explained by considering partial ionization. For this purpose an analogy is made between the preionized gas and an afterglow plasma. A concluding section summarises the main results, and considers possible future experiments.

5.2 THE COMPUTER CODE

A radial version of the Hain-Roberts MHD code[60,61] was used to determine the effect of bias fields, partial ionization and impurities on a theta pinch. This programme solves the MHD equations for a three fluid plasma of ions, electrons and neutrals in an infinitely long cylinder. All temperatures can relax towards one another by elastic collisions except for ion and neutral particle temperatures; here charge exchange is assumed to dominate. Both ions and electrons are shock heated. Joule heating and radiation losses are confined to the electrons. Frictional heating between ions and electrons is included.

Recombination of ions and electrons, and line radiation, are not included. The coefficients in the programme were chosen to suit the Culham 8 m theta pinch; that is, for a high temperature theta pinch[62].

The variables used were

α the ionization coefficient of the preionized gas
γ the percentage of impurity, taken as oxygen
B_1 the bias field
$\hat{B}$ the peak external magnetic field
ω the magnetic field oscillation frequency ($B = \hat{B} \sin \omega t$)
r the vacuum tube wall radius
p the initial filling pressure
the initial particle distribution.

Each computer run was started by defining the preionized gas temperature $T_i = T_e = 2\,eV$. The initial particle distributions were either planar or parabolic.

5.3 THE COMPUTATIONAL RESULTS

5.3.1 The Effect of Varying the Ionization Coefficient (see Section 2.6.2)

The code was run with the ionization coefficient $\alpha = 1.0$ and 0.1, with

$\gamma = 0$

$B_1 = 0$ G

$\hat{B} = 7$ to 77 kG

$\omega \simeq 2 \times 10^5$ rad s^{-1}

$r = 4$ cm

$p = 20$ mtorr of D_2.

The radially averaged electron temperature T_e is shown in Fig.5.1 for $\dot{B}_o = 2.44\,kG\,\mu s^{-1}$ and $7.85\,kG\,\mu s^{-1}$, $\alpha = 1.0$ and 0.1. With $\dot{B}_o = 2.44\,kG\,\mu s^{-1}$ the heating rate was reduced by 85% by decreasing the ionization coefficient from 1.0 (fully ionized) to 0.1 (10% ionized). With $\dot{B}_o = 7.85\,kG\,\mu s^{-1}$, the heating rate was reduced by 30%. Fig.5.2 shows the heating rate $\dot{T}$

as a function of $\dot{B}_0$ and α; in all the cases considered there was less than 5% difference between T_e and T_i. The two curves shown for $\alpha = 1.0$ and 0.1 converge for $\dot{B}_0 \geqslant 10\,kG\,\mu s^{-1}$. With $\alpha = 1.0$ the heating rate is described by $\dot{T} \propto \dot{B}_0^{\frac{3}{2}}$. With $\alpha = 0.1$ there is a value of $\dot{B}_0 \simeq 1\,kG\,\mu s^{-1}$ below which no heating occurs. The points marked A to E are discussed in Section 5.4.5.

5.3.2 The Effect of Varying the Impurity Content (see Section 2.6.3)

The code was run with the impurity content γ = 0, 0.1 and 1.0% of oxygen, with

α = 1.0
B_1 = 0 G
$\hat{B}$ = 14 kG
ω = 1.75×10^5 rad s^{-1}
r = 4 cm
p = 20 mtorr D_2

The resulting radially averaged electron temperatures are shown in Fig.5.3. With 0.1% of oxygen the heating rate was reduced by 50%. With 1% of oxygen the maximum temperature was reached at 2 μs; after this time the energy losses due to bremsstrahlung radiation were greater than the energy input, and the plasma cooled. These curves relate to the 2 m thetatron described in Section 3.7.

5.3.3 The Effect of Varying the Bias Field

The code was run with the bias field B_1 = 0, ± 0.5, ± 1.0 and ± 1.5 kG, with

α = 1.0
γ = 0
$\hat{B}$ = 20 kG
ω = 2.15×10^5 rad s^{-1}
r = 4 cm
p = 20 mtorr D_2.

Fig.5.4 shows the total line energy at 2.3 μs, derived from the particle

density, temperature and magnetic field, as a function of the bias field. The results are normalised to the line energy with $B_1 = 0\,G$. Positive bias decreased the energy, and negative bias increased the energy up to twice that for $B_1 = 0\,G$. Temperatures were found to depend on the bias field in a similar manner (see Section 5.3.4).

5.3.4 Simulations of the Experimental Conditions

The code was run with

$\alpha = 0.1$, 0.5 and 1.0
$\gamma = 0$
$B_1 = 0, \pm 250, -500$ and $-1000\,G$
$\hat{B} = 17\,kG$
$\omega = 1.9 \times 10^5$ rad s^{-1}
$r = 4.3$ cm
$p = 30$ mtorr D_2,

to simulate the initial conditions used in the heating experiments described in Chapter IV. Radial temperature profiles showed that both T_i and T_e were constant to within 20% across the plasma. For times $< 2\,\mu s$ T_e was greater than T_i, but after this time the temperatures relaxed to within 5% of each other. Electron density profiles were Gaussian except when negative bias fields were used; then hollow profiles were found. In all cases the trapped negative flux diffused out of the plasma with an e-folding time $\leq 1\,\mu s$; this justified the assumption that all trapped flux was positive in the derivation of average temperature from the diamagnetism (see Section A.2.10, equation A.2.20).

The computed average temperatures at $4\,\mu s$ are plotted in Fig.4.7 as two curves, for $\alpha = 0.5$ and 1.0. Allowing for the experimental errors (see Fig.A2.2) the experimentally determined temperatures lie between the computational curves.

Calculations of the line mass showed that at least 80% of the initial filling mass was collected, even with $\alpha = 0.1$. Changing the

initial particle distribution from planar to parabolic changed the line mass by less than 5%. No indication of a line mass dependence on $\dot{B}_o$, as observed experimentally (see Fig.4.9), was found.

In Fig.5.5 computational and experimental diamagnetisms and temperatures are compared. Fig.5.5(a) shows that the first peak of the diamagnetic signal was well predicted, but a strong damping of the oscillations was found. The average diamagnetic signal was well predicted. Fig.5.5(b) shows the computed and experimental average temperatures as a function of time; they were found to agree, within the experimental errors.

5.4 A COMPARISON BETWEEN THE EXPERIMENTAL AND COMPUTATIONAL RESULTS

5.4.1 Introduction

The experimental observations described in Chapter IV are discussed with reference to the computational results. Explanations are suggested for the following phenomena

(1) The dependence of temperature on the preionization to main azimuthal current delay (see Section 4.4.2 and 4.4.5).

(2) The dependence of temperature on the bias field (see Sections 4.4.4 and 4.4.5).

(3) The dependence of line mass on $\dot{B}_o$ (see Section 4.4.6)

(4) The damping of the radial oscillations (see Section 5.3.4)

(5) The dependence of the heating rate on $\dot{B}_o$ (see Section 4.4.5).

5.4.2 Temperature and Preionization to Main Azimuthal Current Delay

It was found that increasing the delay τ_{pI} between the preionization and main azimuthal current decreased the diamagnetism and temperature of the plasma (see Section 4.4.2). This was expected because a longer delay allows the preionized plasma to cool and the ions and electrons to recombine. The ionization coefficient is reduced; therefore the final temperatures obtained in the theta pinch are reduced (see Fig.5.1 and 5.2).

However, many theta pinches have operated with $\tau_{pI} \geq 50\,\mu s$ without a large temperature reduction[42]. This can be explained with reference to Fig.5.2. The heating rate, $\dot{T}_{Av}$, is a function of $\dot{B}_o$ and the ionization coefficient α. For $\dot{B}_o \geq 10\,kG\,\mu s^{-1}$, reducing α from 1.0 to 0.1 has little effect on the heating rate. The 3.5 m thetatron operated with $\dot{B}_o \leq 3.3\,kG\,\mu s^{-1}$ (the points marked A on Fig.5.2). In this case the heating rate, and consequently the final plasma temperatures obtained, are greatly reduced as α is decreased. Therefore the computations show that the 3.5 m theta pinch temperatures were strongly dependent on the ionization coefficient α, and consequently on the delay time τ_{pI}, as was found experimentally.

Fig.4.7 shows that, for a plasma without a bias field, the temperature after $4\,\mu s$ was increased from 25 eV to 44 eV if the delay τ_{pI} was reduced from $0\,\mu s$ to $-2\,\mu s$. These two temperatures correspond, within the experimental errors, to the computed temperatures with the ionization coefficient $\alpha = 0.5$ and 1.0. If the temperature dependence on τ_{pI} is a consequence of the ionization coefficient's dependence on τ_{pI}, a mechanism must be found which predicts a decrease in α from 1.0 to 0.5 in $2\,\mu s$.

An analogy is made between the preionized gas and an afterglow plasma. Long and Newton[63] have computationally analysed a hydrogen afterglow in 20 mtorr of hydrogen, with densities and temperatures similar to those expected in the preionized gas. These computations showed that a rapid cooling at the plasma edges occurred for the first few microseconds, caused by wall contact. To maintain pressure balance the plasma expanded. Therefore the electron temperatures and densities, which were linked by three body recombination (see Section A1.3) were reduced in the central region, and a dense atomic layer formed close to the wall. After the initial sharp decrease in electron density a slow fall was found, with an e-folding time of $20\,\mu s$. These computed predictions were found to agree

well with experimental results[64], although the rapid expansion to the walls, producing a sharp initial decrease in electron density, was a computational effect due to the initial lack of thermodynamic equilibrium.

The preionization system used for the 3.5 m theta pinch produced a rapid contraction and expansion (see Fig.4.2(a)). Therefore the neutral particle density should increase rapidly, as computed by Long and Newton, with a corresponding decrease in the ionization coefficient. This mechanism would explain the dependence of α on the delay τ_{pI} which is necessary to explain the temperature dependence on τ_{pI}. Any impurities introduced into the preionized gas by plasma wall contact would also reduce the final theta pinch temperatures obtained (see Section 5.3.2).

5.4.3 Temperature and Bias Field

Fig.4.7 shows the experimental and computed temperatures at $4\,\mu s$ for a theta pinch plasma with $\dot{B}_0 = 3.3\,kG\,\mu s^{-1}$ and bias field B_1 between -500 and $+500$ gauss. As the bias field was increased, either positive or negative, the experimental temperature with the delay $\tau_{pI} = 0$ approached the temperature with $\tau_{pI} = -2\,\mu s$; both were then in agreement with the computed temperature for the ionization coefficient $\alpha = 1.0$.

Fig.4.2(a) shows a streak photograph of the preionization gas with and without a bias field; the bias field was found to inhibit the concontraction and expansion associated with the z pinch preionization. The combination of an axial field and a z pinch is called a stabilized pinch; the axial magnetic field reduces the plasma radial velocity. By restricting the radial expansion to the wall, the sharp decrease in the electron density and the ionization coefficient (see Section 5.4.2) would not occur. Therefore bias fields would increase the ionization coefficient and consequently explain the temperature dependence shown in Fig.4.7.

5.4.4 The Line Mass

The experiments to determine the line mass showed that the percentage of the initial filling mass collected was a function of the filling pressure and the initial rate of rise of external magnetic field, $\dot{B}_0$, but not a function of the delay τ_{pI} or the bias field B_1 (see Section 4.4.6). The computed results predicted at least an 80% mass collection; this value was changed less than 5% by varying the bias field, ionization coefficient and impurity content.

Both the experiments and the computations showed that the mass collection was insensitive to the preionized gas conditions. It is suggested that recombination processes, excluded from the computer code, may be important in determining the line mass. During the early stages of the theta pinch the plasma periphery would be cold; recombination of ions and electrons would allow the resulting neutral particles to escape from the plasma and reduce the mass collection. As $\dot{B}_0$ was increased the heating rate would increase, so that fewer neutral particles would be produced and the mass collection would increase. A dense layer of neutral atoms outside the plasma column might help to damp the radial mass oscillations, and explain the discrepancy between the experimental and computed diamagnetism (see Fig.5.5(a)).

5.4.5 The Heating Rates

Experimental determinations of the heating rate $\dot{T}$ showed that increasing $\dot{B}_0$ decreased $\dot{T}$, (see Fig.4.8), contrary to the computational results (see Fig.5.2). This is explained by considering the plasma line mass; as $\dot{B}_0$ was decreased the line mass decreased, so that the available energy was used to heat fewer particles, producing higher temperatures.

An analytic formula derived by Mewe[11] (equation (2.4.2)) predicts that the final plasma temperature is a function of the filling pressure p :

$$\hat{T} \propto \frac{1}{p^{\frac{2}{3}}} \quad . \qquad \ldots (5.4.1)$$

It was assumed that all the gas was collected by the implosion. Experiments on the Culham 8 m theta pinch were performed to determine the dependence of temperature on the initial filling pressure, using laser light scattering techniques[42]. The results agreed with the predictions of the Hain-Roberts MHD code; in all cases the mass collection was $\simeq 100\%$. Both the experimental and computational results can be fitted to an expression in the form of equation (5.4.1).

If the percentage of mass collected is m_p, equation (5.4.1) can be used to predict the dependence of the heating rate on the mass collection and the pressure:

$$\dot{T} \propto \frac{1}{(m_p p)^{\frac{2}{3}}} \quad . \qquad \ldots (5.4.2)$$

The experimentally measured heating rates were converted to the equivalent heating rate for 100% mass collection using equation (5.4.2); the results are shown in Fig.5.6. Also shown are the computational heating rates, with approx. 100% mass collection. With $\tau_{pI} = -2\,\mu s$ the experimental heating rates lie between the computational curves for the ionization coefficient $\alpha = 0.5$ and 1.0. With $\tau_{pI} = 0\ \mu s$ the heating rates lie between the curves for $\alpha = 0.1$ and 0.5. The equivalent heating rates increase with increasing $\dot{B}_o$, and increase for decreasing τ_{pI}, in accordance with the process suggested to explain the experimentally determined dependence of temperature on τ_{pI} (see Section 5.4.2).

To derive a general expression for the heating rate, equation (5.4.2) is combined with the computational heating rate, $\dot{T} \propto \dot{B}_o^{\frac{3}{2}}$, to give

$$\dot{T} \propto \frac{\dot{B}_o^{\frac{3}{2}}}{(m_p p)^{\frac{2}{3}}} \quad . \qquad \ldots (5.4.3)$$

The vacuum tube wall radius r can be accounted for by replacing $\dot{B}_o$ by the azimuthal electric field at the tube wall, E_θ (see equation (2.3.1)). Then

$$\dot{T} \propto \frac{(r\dot{B}_o)^{\frac{3}{2}}}{(m_p p)^{\frac{2}{3}}} . \qquad \ldots (5.4.4)$$

Equation (5.4.4) was used to scale the experimental heating rates (see Fig.4.8) to a theta pinch with a 4 cm tube wall radius, and 100% mass collection of 20 mtorr of deuterium. The results are shown in Fig.5.2 as the experimental ranges marked A. The ranges marked B are the scaled heating rates of the Culham HBTX [103] for a range of preionized gas conditions, obtained from the diamagnetism[65]. Range C corresponds to the scaled heating rates of the Culham 8 m theta pinch, obtained by laser light scattering experiments[42]. Again the results are shown for a range of preionized gas conditions. Point D corresponds to the German ISAR I theta pinch[43]. In this experiment the electron temperature, obtained from the continuum light emission, was larger than the ion temperature, obtained from the neutron emission. Because all the computed values of T_e were within 5% of T_i, the experimental heating rate was plotted as an average heating rate. Similarly the point E was derived for the American SCYLLA IV theta pinch[66], where T_e was obtained from the soft X-ray emission and T_i deduced from pressure balance considerations.

The scaled heating rates lie between the computed heating rates with the ionization coefficient $\alpha = 1.0$ and 0.1, confirming the heating rate equation, equation (5.4.4), over a range $1.5 \leq \dot{B}_o \leq 60\,\mathrm{kG\,\mu s^{-1}}$, $10 \leq p \leq 30$ mtorr and $4 \leq r \leq 6$ cm. None of the experiments considered were affected by end losses; these were not included in the computer code calculations.

A comparison can be made between equation (5.4.4) and Mewe's analytic expression for the peak temperature of a theta pinch (see equation (2.4.2)). If it is assumed that the temperature has a sinusoidal time dependence, Mewe's expression gives

$$\dot{T} \propto \omega^{\frac{1}{3}} \left(\frac{r}{p}\right)^{\frac{2}{3}} \dot{B}_o^{4/3} \qquad \ldots (5.4.5)$$

where ω is the frequency of the sinusoidal magnetic field. This expression agrees with equation (5.4.4) over the parameter ranges considered.

A scaling law used at Los Alamos[67] supposes that the plasma is shock heated by an amount proportional to the azimuthal electric field E_θ for a time proportional to $E_\theta^{-\frac{1}{2}}$, and is then adiabatically heated;

$$T \propto E_\theta^{\frac{3}{2}} B \, . \qquad \ldots (5.4.6)$$

If it is assumed that the temperature dependence on time is sinusoidal, then

$$\dot{T} \propto r^{\frac{3}{2}} \dot{B}_o^{\frac{5}{2}} \, . \qquad \ldots (5.4.7)$$

This dependence of $\dot{T}$ on $\dot{B}_o^{\frac{5}{2}}$ is much greater than that found either computationally or experimentally.

5.5 CONCLUSIONS

5.5.1 Summary

Computational simulations of the heating and energy loss processes in a theta pinch showed that, with the initial rate of rise of external field $\dot{B}_o \leqslant 10\,\mathrm{kG\,\mu s^{-1}}$, the ionization coefficient and impurity content of the preionized gas governed the final plasma temperature. When the preionized gas was 10% ionized, a value of $\dot{B}_o \simeq 1\,\mathrm{kG\,\mu s^{-1}}$ was found below which the plasma did not heat. A scaling law was found which predicted the plasma maximum heating rate $\dot{T}$;

$$\dot{T} \propto \frac{(r\dot{B}_o)^{\frac{3}{2}}}{(m_p p)^{\frac{2}{3}}},$$

where

r is the vacuum tube wall radius

p is the filling pression

m_p is the percentage of mass collected.

Results from five separate experiments were shown to be well described by this formula.

The heating experiments performed on the 3.5m theta pinch, summarised in Section 4.5, showed that a reprcducible, MHD stable plasma could be produced with a temperature above 50 eV, suitable for the experiments on perturbed motion (see Chapter VII). Negative bias fields increased the plasma temperature and reduced the temperature dependence on the time delay between the preionization current and the compression current. This dependence was accredited to the ionization coefficient of the preionized gas; the rapid radial expansion cooled the plasma, increased the atom density and reduced the ionization coefficient. Bias fields inhibited the expansion, and increased the coefficient.

Experiments showed that the line mass M was a function of $\dot{B}_o$; this was not found computationally. It was suggested that particle loss processes not included in the computer code, in particular the recombination of ions and electrons, would allow neutral atoms to escape from the plasma and reduce the line mass. Larger values of $\dot{B}_o$, producing larger heating rates, would increase the line mass because recombination rates decrease as the temperature increases. A layer of neutral particles outside the plasma might explain the damping of the diamagnetic signal oscillations observed experimentally.

5.5.2 Applications and Future Work

Theta pinch design (see Section 2.9) should include a consideration of the preionized gas. The reduced heating rates produced by partial preionization can be overcome using small bias fields; alternatively the compression coil inductance and the capacitor bank should be chosen so that $\dot{B}_0 \geq 10\,\mathrm{kG}\,\mu\mathrm{s}^{-1}$; then the heating rate is large enough to overcome the energy losses.

An analogy was made between the preionized gas and an afterglow plasma to explain the temperature dependence on the delay τ_{pI} and the bias field. Interferometric and spectroscopic studies would determine the ionization coefficient, and check the validity of the analogy.

The Hain-Roberts MHD code should be adapted to include recombination of electrons and ions. The dependence of the line mass and the damping of the radial oscillations might then be explained. Line radiation should also be included; the effect of impurities on the plasma parameters could then be compared with computational predictions.

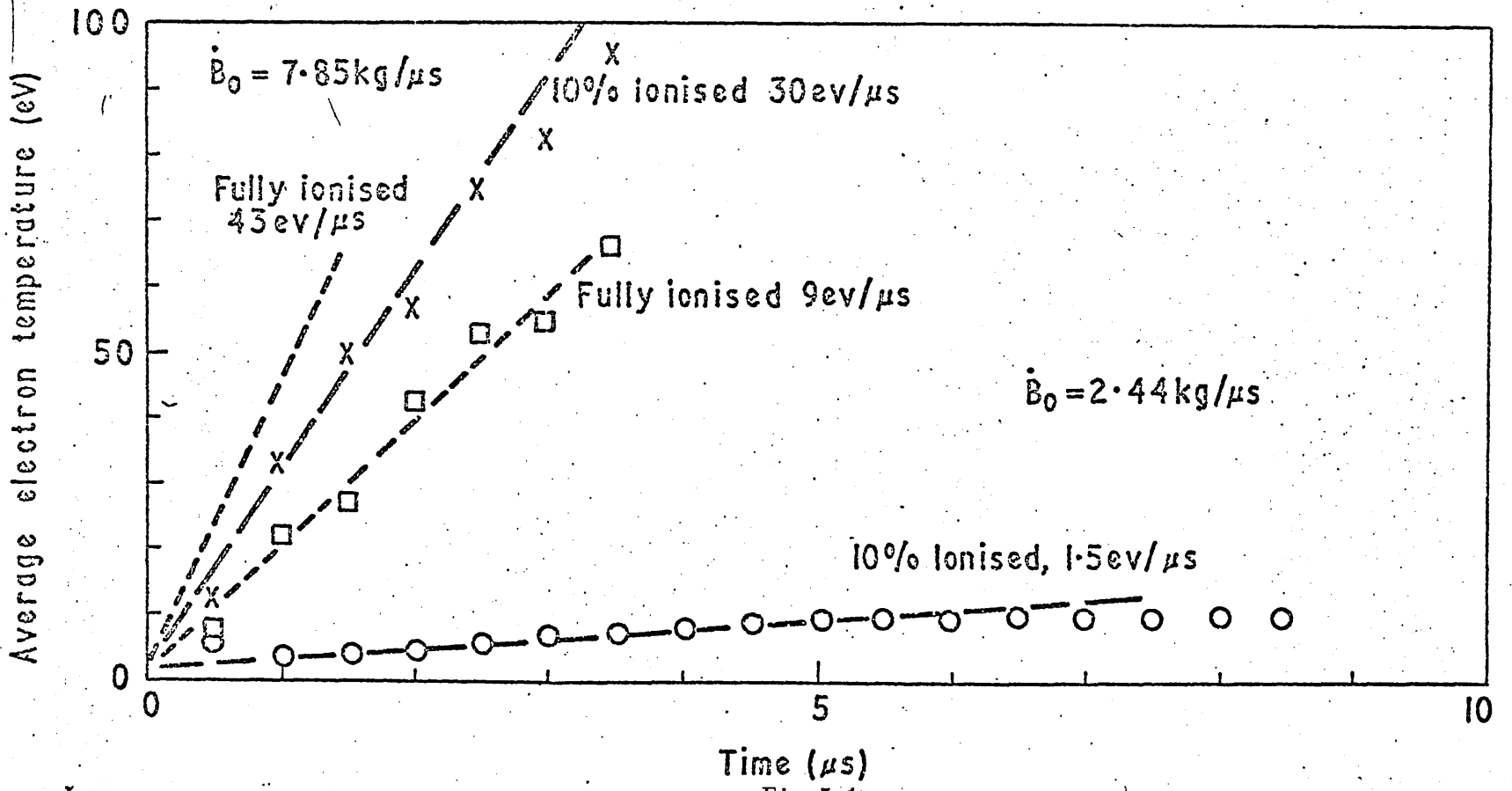

Fig.5.1

The temperature as a function of the ionization coefficient

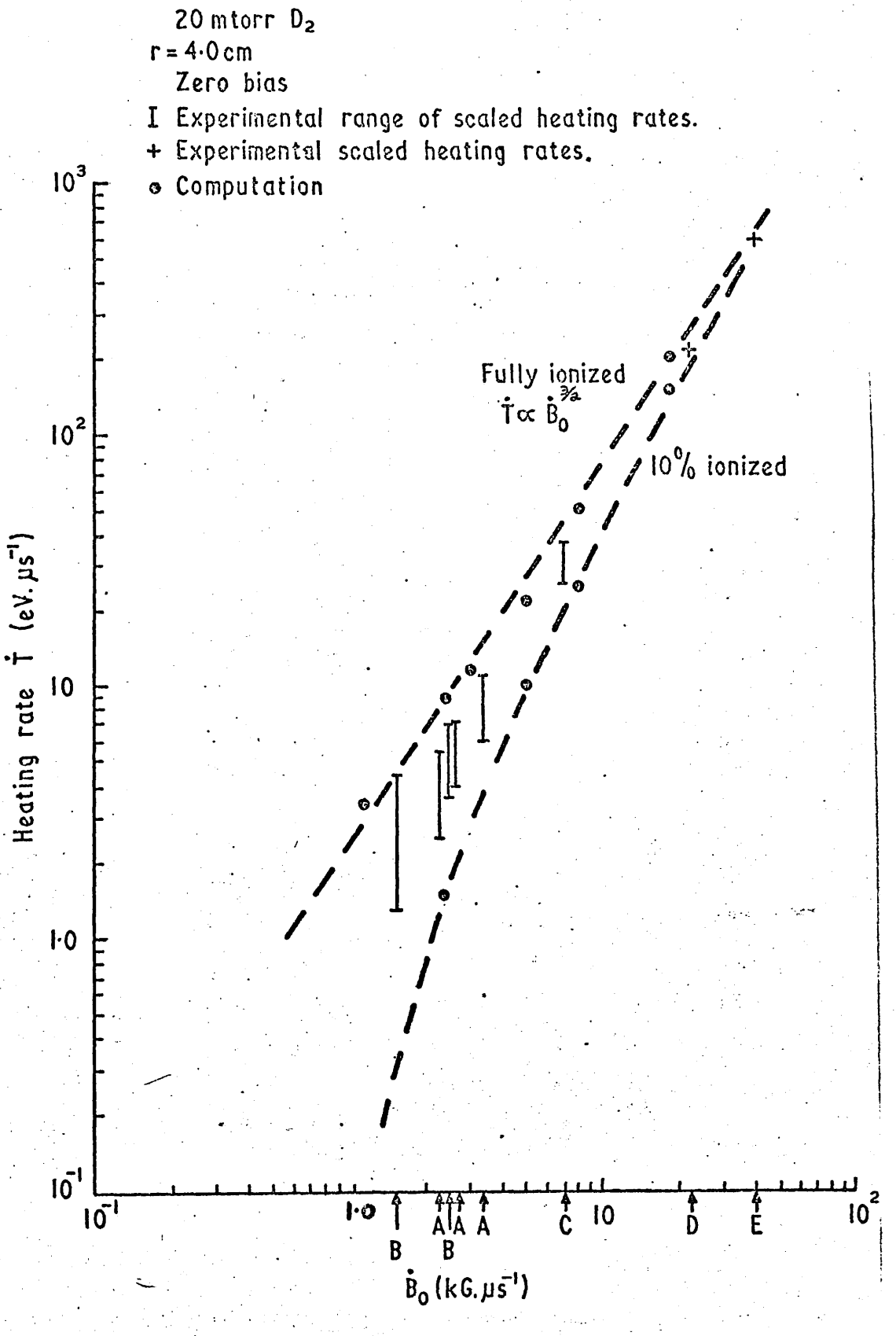

Fig.5.2

Experimental and computed heating rates

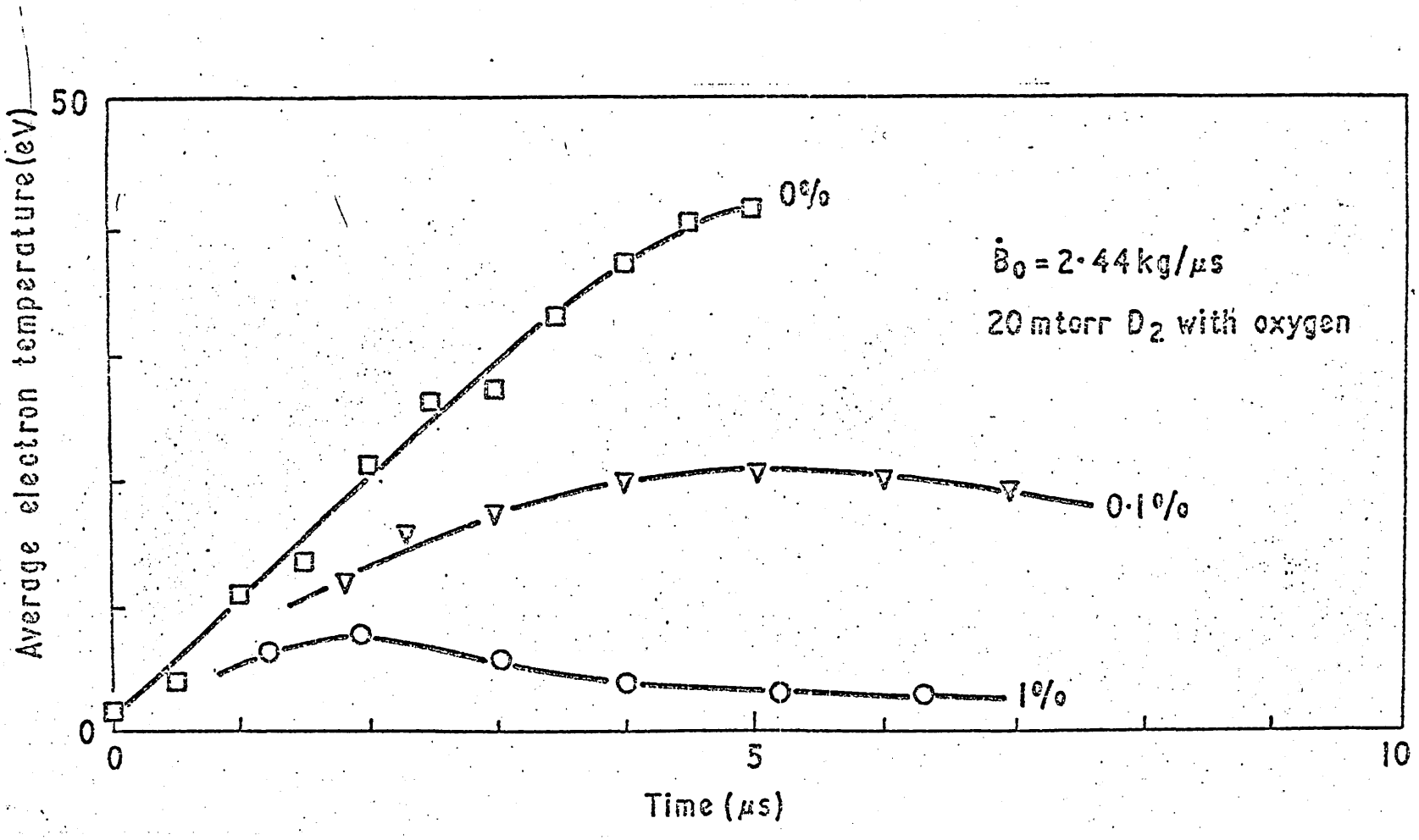

Fig.5.3
The temperature as a function of the impurity concentration

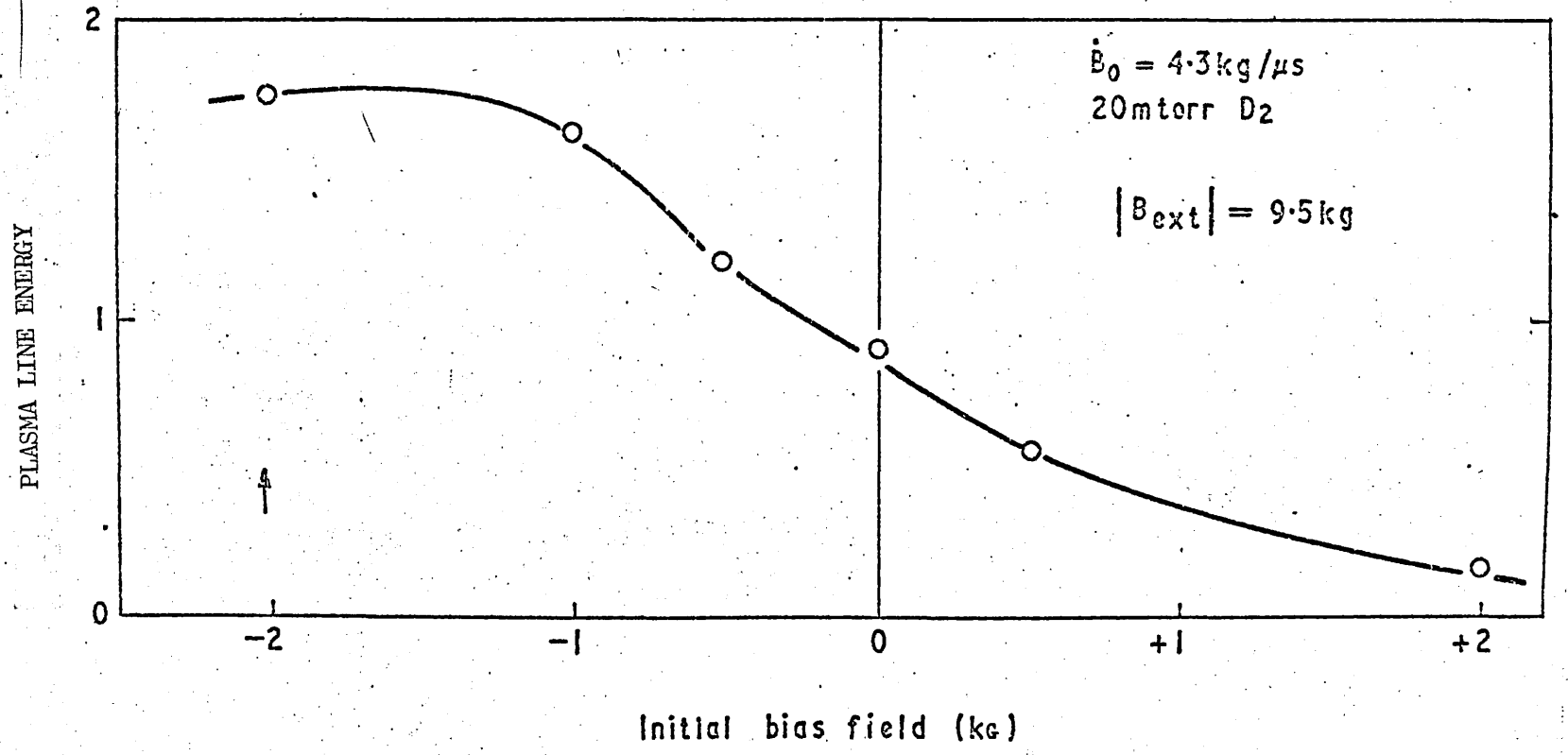

Fig.5.4
Line energy against bias field

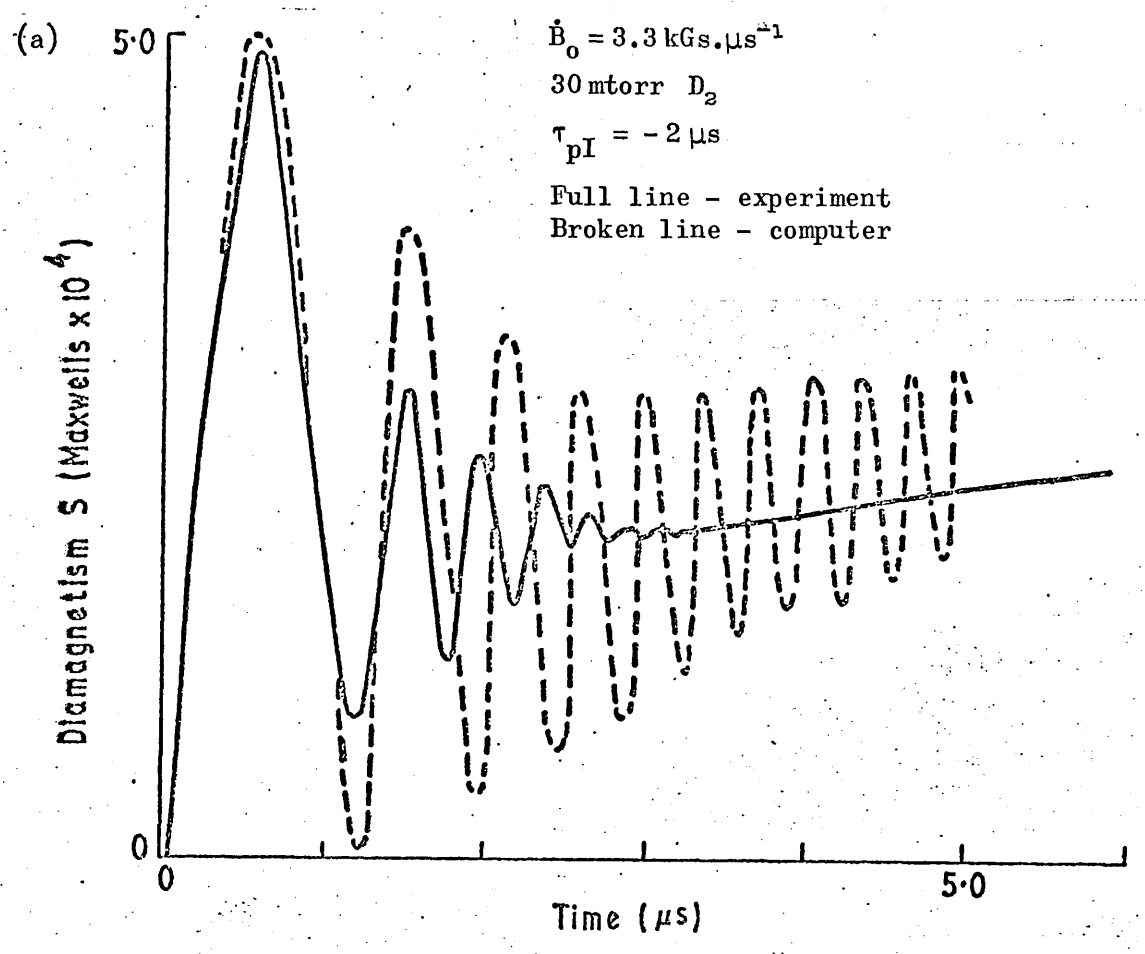

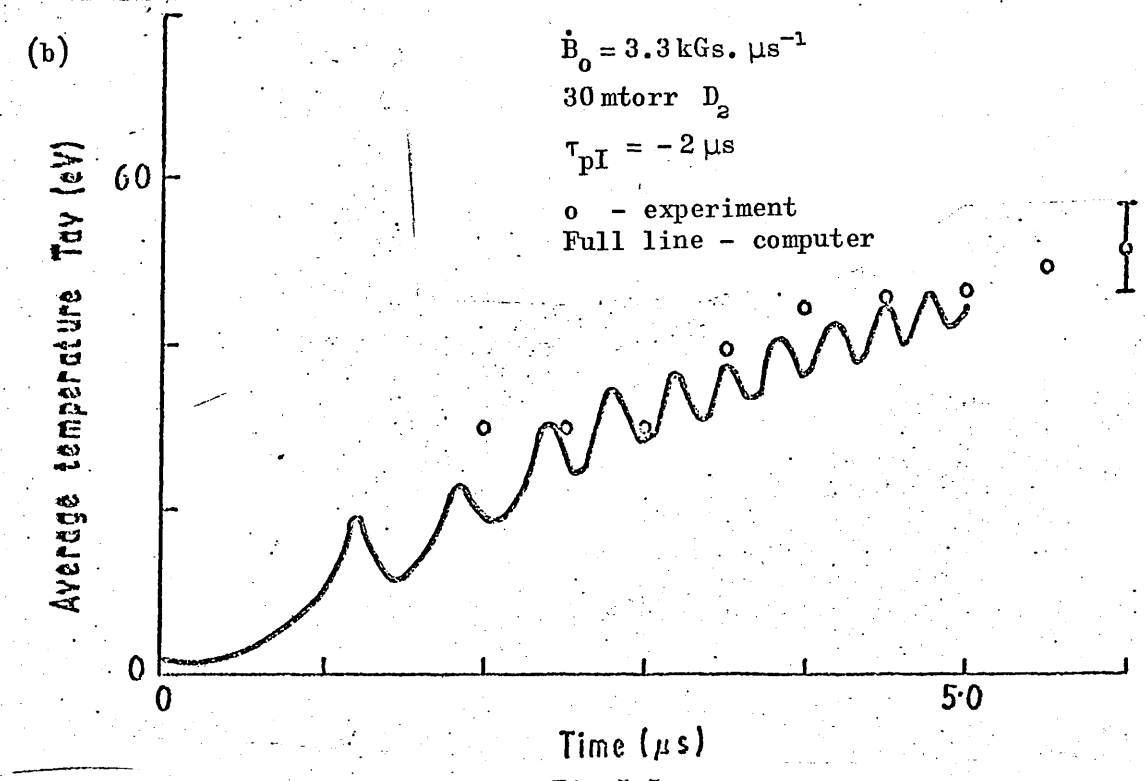

Fig.5.5

(a) Experimental and computed diamagnetism

(b) Experimental and computed temperature

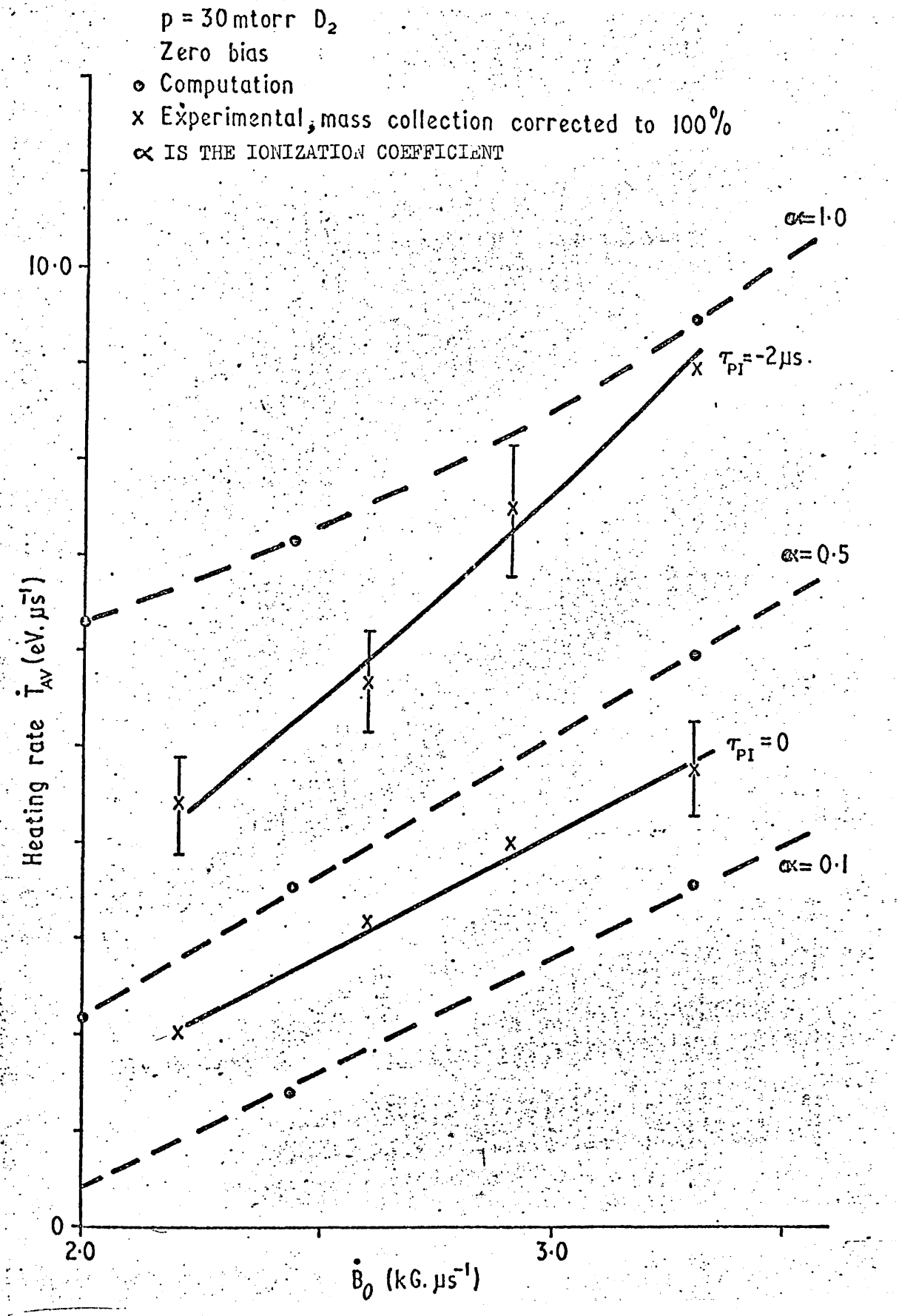

Fig.5.6

Experimental and computed heating rates

CHAPTER VI

A THEORY FOR PLASMA DISPLACEMENTS DUE TO A LOCAL PERTURBING MAGNETIC FIELD

6.1 INTRODUCTION

A theory describing the motion of a long, straight theta pinch in the presence of a nearby current loop with its axis parallel to the plasma is presented[79]. Theoretical predictions of the model will be used for a comparison with experimental results in Chapter VIII.

The disturbance of the plasma equilibrium position due to a time dependent current in the loop is used to calculate the restoring forces on the plasma. For this purpose the method of Haas and Wesson[33], reviewed in Section 6.2, is adapted. The resulting equation of motion is analysed using two methods.

An alternative theory[68], based on the integration of the $\bar{j} \times \bar{B}$ force over the plasma volume, leads to a similar equation of motion. This equation is analysed, and the results compared with those of the first model. The applicability of each model to the experiments described in Chapter VII is considered in Chapter VIII.

6.2 THE THETA PINCH EQUATION OF MOTION

Haas and Wesson[33], and Morse[35], have analysed the stability of an infinitely long, axisymmetric theta pinch to long wavelength, $m = 1$ motion (see Section 2.8.4). The Haas and Wesson theory is summarised here.

Consider a perfectly conducting, compressible plasma with a trapped magnetic field B_i, separated from a vacuum region with a field B_e by a sharp boundary. It is assumed that no currents flow within the plasma body, implying no pressure gradients.

The equilibrium is obtained by a small parameter expansion in ϵ, the ratio of the plasma radius R to the axial distance along the plasma over which quantities vary. The hydromagnetic energy principle[69] is applied to the model, assuming that the characteristic lengths of linear perturbations are of the same order as the equilibrium characteristic lengths.

The axial (z) motion and the distortion in the (r,θ) plane are assumed to be negligible, so that the displacement is of the form $\bar{\xi} = \bar{\xi}_{r,\theta}(z)$, where $\bar{\xi}_{r,\theta}$ is the displacement in the (r,θ) plane.

Using the above assumptions the kinetic energy T of the plasma can be written;

$$T = \frac{\pi}{2} \int R^2 \rho \left(\frac{\partial \xi}{\partial t}\right)^2 dz \ . \qquad \ldots (6.2.1)$$

The potential energy change δW caused by the displacement ξ is

$$\delta W = \delta W_s + \delta W_v + \delta W_f \qquad \ldots (6.2.2)$$

where the surface energy δW_s is given by

$$\delta W_s = \frac{\pi}{2\mu_o} \int \xi^2 B_e^2 \beta \frac{d^2R}{dz^2} R dz \qquad \ldots (6.2.3)$$

the vacuum energy δW_v is given by

$$\delta W_v = \frac{\pi}{2\mu_o} \int B_e^2 \left[\frac{d}{dz}(R\xi) - 2\xi \frac{dR}{dz}(1-\beta)\right]^2 \cdot \frac{(1+(R/R_W)^2)}{(1-(R/R_W)^2)} dz \qquad \ldots (6.2.4)$$

and the fluid energy δW_v is given by

$$\delta W_f = \frac{\pi}{2\mu_o} \int B_i^2 \left[R \frac{d\xi}{dz} - \xi \frac{dr}{dz}\right]^2 dz \ , \qquad \ldots (6.2.5)$$

where R_W is the conducting wall radius. The Lagrangian is given by[70]

$$\mathcal{L} = \int L \, dz = T - \delta W \ . \qquad \ldots (6.2.6)$$

From Hamilton's principle the equation of motion is

$$\frac{\partial L}{\partial \xi} - \frac{\partial}{\partial z}\left(\frac{\partial L}{\partial(\partial\xi/\partial z)}\right) - \frac{\partial}{\partial t}\left(\frac{\partial L}{\partial(\partial\xi/\partial t)}\right) = 0 \qquad \ldots (6.2.7)$$

Explicitly this is[34]

$$(\mu_o R^2 \rho)\frac{\partial^2 \xi}{\partial t^2} = \frac{\partial}{\partial z}\left((2-\beta+\alpha)\, B_e^2 R^2 \frac{\partial \xi}{\partial z}\right)$$

$$+\left(4B_e^2\left(\frac{dR}{dz}\right)^2\left((1-\beta^2)+\frac{\alpha\beta}{2}(3-2\beta)\right)\right.$$

$$\left.-2B_e^2 R\frac{d^2R}{dz^2}\left(1-\beta-\frac{\alpha}{2}(2\beta-1)\right)\right)\xi \qquad \ldots (6.2.8)$$

where

$$\alpha = \frac{2R^2}{R_W^2 - R^2} .$$

For a straight pinch, $R \neq R(z)$. If the conducting wall radius is much larger than the plasma radius ($R_W \gg R$), then $\alpha \to 0$ and equation (6.2.8) becomes

$$\frac{\partial^2 \xi}{\partial t^2} - V_A^2 (2-\beta)\frac{\partial^2 \xi}{\partial z^2} = 0 , \qquad \ldots (6.2.9)$$

where

$$V_A = \frac{B_e}{\sqrt{\mu_o \rho}}$$

an Alfven velocity (see Section A1.3, under hydromagnetic waves). If $\xi = \xi_{r,\theta} \exp i(\omega t + kz)$, equation (6.2.9) becomes

$$\omega^2 = V_A^2 (2-\beta) k^2 . \qquad \ldots (6.2.10)$$

Therefore long wavelength $m=1$ perturbations to the magnetic fields of a straight theta pinch produce transverse hydromagnetic waves, which propagate along the field lines with a phase velocity given by

$$V_{m=1} = V_A \sqrt{2-\beta} . \qquad \ldots (6.2.11)$$

If motion in a non-inertial frame of reference is considered, the Langrangian, equation (6.2.6), must be replaced by[70]

$$\mathcal{L} = \int L\, dz = T - \delta W - mw(t) \cdot \xi , \qquad \ldots (6.2.12)$$

where m is the mass and $w(t)$ is the acceleration of the frame of reference. If the reference frame is described by $\eta(z,t)$, the extra term becomes:

$$mw(t) \cdot \xi = \int \rho \ddot{\eta}\, \xi\, dV = \pi \int R^2 \rho \eta \xi\, dz . \qquad \ldots (6.2.13)$$

Using Hamilton's principle, the equation of motion for a straight theta pinch becomes

$$\frac{\partial^2 \xi}{\partial t^2} - V_A^2 (2-\beta) \frac{\partial^2 \xi}{\partial z^2} + \frac{\partial^2 \eta}{\partial t^2} = 0 \ . \qquad \ldots (6.2.14)$$

6.3 THE PLASMA EQUILIBRIUM IN THE PRESENCE OF A PERTURBING FIELD[79]

The momentum equation for a plasma in static equilibrium is

$$\nabla p = \bar{j} \times \bar{B} \ . \qquad \ldots (6.3.1)$$

Multiplying equation (6.3.1) by $\bar{B}$ gives

$$\bar{B} \cdot \nabla p = 0 \ . \qquad \ldots (6.3.2)$$

Therefore in static equilibrium the plasma pressure is constant along a line of force. Consider a line plasma, where the plasma radius R is small compared with other characteristic radial lengths. When a theta-pinch is produced the plasma axis corresponds to the central line of force inside the compression coil. This line of force is then the static equilibrium position, by equation (6.3.2). If a perturbing field $\bar{B}_1$ is applied the central line of force, and consequently the equilibrium position, will move.

The equation defining a line of force can be written[71]:

$$d\bar{\ell} = \bar{B} \lambda \qquad \ldots (6.3.3)$$

where $d\ell$ is an element of the line of force, λ is a constant. In cylindrical coordinates this becomes

$$\frac{dr}{B_r} = r \frac{d\theta}{B_\theta} = \frac{dz}{B_z} \ . \qquad \ldots (6.3.4)$$

A magnetic field $\bar{B}\left[B_r, B_\theta, B_z\right]$ can be expressed in terms of the vector potential $\bar{A}\left[A_r, A_\theta, A_z\right]$, where

$$\bar{B} = \nabla \times \bar{A} \ . \qquad \ldots (6.3.5)$$

Assuming axial symmetry, equation (6.3.4) can then be written in terms of the vector potential as[72]

$$r A_\theta(r, z) = \lambda \ , \qquad \ldots (6.3.6)$$

where λ is a constant.

Consider the case when a straight theta pinch is perturbed by an n turn current loop, area A_d and current I_d, with its axis parallel to, and a distance b from, the plasma (see Fig.6.1(a)). If any image currents produced in the conducting compression coil walls are negligible, and the distance b is much larger than the loop radius r_d, the vector potential of the perturbing field $\bar{B}_1$ is[73]

$$\bar{A}_\theta^1 = \frac{\mu_o}{4\pi} \frac{n I_d \bar{A}_d r_1}{(r_1^2 + z^2)^{\frac{3}{2}}} \qquad \ldots (6.3.7)$$

where r_1 is the radial coordinate with respect to the loop. This is the vector potential of a magnetic dipole of moment M:

$$M = n A_d I_d \qquad \ldots (6.3.8)$$

The vector potential of the field inside the compression coil without a plasma can be written in cylindrical coordinates (r_1, θ, z) as[74]

$$\bar{A}_\theta^o = (r_1 - b) \frac{\bar{B}_e}{2} . \qquad \ldots (6.3.9)$$

Equation (6.3.9) describes the unperturbed plasma vector potential if the plasma does not perturb the vacuum field significantly; that is, if the plasma has a low β value or a small radius.

The field lines in the coordinate system (r_1, θ, z) are axisymmetric; therefore equation (6.3.6) can be applied to describe the motion of the field lines and consequently the plasma equilibrium position. With no perturbing field the vector potential is given by equation (6.3.9) and the equilibrium position is defined by $r_1 = b$. Equation (6.3.6) then gives

$$r_1 (r_1 - b) \frac{B_e}{2} = \lambda , \qquad \ldots (6.3.10)$$

with $r_1 = b$. Therefore the plasma equilibrium is defined by $\lambda = 0$.

When the perturbing field $\bar{B}_1$ is applied, the equilibrium position is described by equation (6.3.6) with $\lambda = 0$:

$$r_1 (A_\theta^o + A_\theta^1) = 0 . \qquad \ldots (6.3.11)$$

Explicitly this is:

$$r_1 \left((r_1 - b) \frac{B_e}{2} + \frac{\mu_o}{4\pi} \frac{n A_d I_d r_1}{(r_1^2 + z^2)^{\frac{3}{2}}} \right) = 0. \qquad \ldots (6.3.12)$$

Equation (6.3.12) has a solution of the form

$$r_1 = \eta + b \ , \qquad \ldots (6.3.13)$$

with $\frac{\eta}{b} \ll 1$. Substituting for r_1 from equation (6.3.13) in equation (6.3.12) gives

$$\eta = - \frac{\mu_o}{4\pi} \frac{2 n A_d I_d}{b^2 B_e (1 + (z/b)^2)^{\frac{3}{2}}} \ . \qquad \ldots (6.3.14)$$

Therefore η, $= r_1 - b$ (see equation (6.3.13)), is the equilibrium position with respect to the initially straight plasma.

If $I_d = I_o f(t)$ and B_e is constant, equation (6.3.14) can be written as

$$\eta_n = - g(z_n) f(t) \ , \qquad \ldots (6.3.15)$$

where

$$\eta_n = \frac{\eta}{k} \qquad \ldots (6.3.16)$$

$$k = \frac{\mu_o 2 n A_d I_o}{4\pi b^2 B_e} \qquad \ldots (6.3.17)$$

$$z_n = \frac{z}{b} \qquad \ldots (6.3.18)$$

and

$$g(z_n) = (1 + z_n^2)^{-\frac{3}{2}} \ . \qquad \ldots (6.3.19)$$

The function $g(z_n)$ describes the spatial dependence of the equilibrium position, and is shown in Fig.6.2.

The assumptions in the derivation of the equilibrium position equation (equation (6.3.14)) are

(1) The plasma does not significantly perturb the vacuum fields; that is, the plasma radius is small or $\beta \ll 1$.

(2) The plasma can be considered as a line plasma; that is, the plasma radius is small.

(3) The current loop magnetic fields can be considered as magnetic dipole fields; that is, $b \gg r_d$.

(4) The conducting walls do not produce image currents; that is, $R_W \gg b$.

(5) The equilibrium displacement is small; that is, $\eta \ll b$.

Each of these assumptions is justified before the model is applied to explain the experimental results (see Chapter VIII).

6.4 PLASMA MOTION IN THE PRESENCE OF A PERTURBING FIELD (79)

6.4.1 The Equation of Motion

Consider the two dimensional situation illustrated in Fig.6.1(b), where the equilibrium position η has been displaced, and the plasma is following the equilibrium. Let $\bar{\xi}$ be the plasma displacement from the equilibrium. Then

$$\bar{y} = \bar{\eta} + \bar{\xi} \qquad \ldots (6.4.1)$$

where $\bar{y}$ is the plasma displacement vector in the coordinate system defined by the straight plasma, and

$\bar{\xi}$ is the plasma displacement in the coordinate system defined by the equilibrium.

If $\left|\frac{\partial \eta}{dz}\right|$ and $\left|\frac{\partial y}{\partial z}\right| \ll 1$, the two coordinate systems are equivalent, and the plasma displacement y is given by

$$y = \eta + \xi \, . \qquad \ldots (6.4.2)$$

Equation (6.2.14) describes the plasma motion about a non-inertial equilibrium. Substituting for ξ from equation (6.4.2) in equation (6.2.14) gives

$$\ddot{y} - V_{m=1}^2 \, y'' + V_{m=1}^2 \, \eta'' = 0 \, , \qquad \ldots (6.4.3)$$

where $V_{m=1} = V_A \sqrt{2-\beta}$, and η is given by equation (6.3.14).

Equation (6.4.3) is the equation of motion of a theta pinch plasma in the presence of the perturbing field produced by a magnetic dipole. It is the wave equation with an additional forcing term $F(z,t)$:

$$\frac{F(z,t)}{M} = - V_{m=1}^2 \, \eta''(z,t) \, , \qquad \ldots (6.4.4)$$

where M is the plasma line mass. An analogy can be made between the plasma and a string under a tension $T = V_{m=1}^2 M$ with a distributed driving force $F(z,t)$. The solution of equation (6.4.3) will represent a wave motion, with displacements propagating along the plasma column. These waves have been called $m=1$ Alfven waves because they are MHD transverse $m=1$ waves, propagating with a phase velocity $V_{m=1} = V_A \sqrt{2-\beta}$.

6.4.2 Plasma Motion with an Oscillating Current

Consider the plasma motion produced when the current in the loop is given by $I_d = I_o \sin \omega t$. The equation of motion, equation (6.4.3) becomes

$$\ddot{y} - V_{m=1}^2 y'' = - \frac{6V_{m=1}^2 \mu_o n A_d I_o (1 - 4(z/b)^2)}{4\pi b^4 B_e (1 + (z/b)^2)^{\frac{7}{2}}} \sin \omega t \quad \ldots (6.4.5)$$

Using the normalising equations, equation (6.3.17) to equation (6.3.19), together with the definitions

$$y_n = \frac{y}{k} \quad \ldots (6.4.6)$$

$$V_n = \frac{V_{m=1}}{\omega b} \quad \ldots (6.4.7)$$

$$t_n = \omega t \ , \quad \ldots (6.4.8)$$

and

$$f(z_n) = - \frac{1}{3} \frac{\partial^2 g(z_n)}{\partial z_n^2} = \frac{(1 - 4 z_n^2)}{(1 + z_n^2)^{\frac{7}{2}}} \quad \ldots (6.4.9)$$

equation (6.4.5) can be written

$$\frac{\partial^2 y_n}{\partial t_n^2} - V_n^2 \frac{\partial^2 y_n}{\partial z_n^2} = - 3 V_n^2 f(z_n) \sin t_n \ . \quad \ldots (6.4.10)$$

The function $f(z_n)$, shown in Fig.6.2, represents the spatial distribution of the equivalent forcing term $F(z,t)$, defined by equation (6.4.4). It has a maximum value when $z_n = 0$, and a minimum value when $z_n = \pm \sqrt{3/2}$. For $|z_n| \gg 1$, $f(z_n) \to 0$. The characteristic length, defined as the distance over which $f(z_n)$ changes sign, is of order $z_n = 1$.

Equation (6.4.10) has a solution $y_n = y_n(z_n, t_n, V_n)$. The peak displacement $\hat{y}_n$ can be obtained for certain limiting conditions. These are

	$V_n \ll 1$	$V_n \gg 1$
$z_n \ll 1$:	$\hat{y}_n = 0$	$\hat{y}_n = - 1$
$z_n \ll 1$:	$\hat{y}_n = 0$	$\hat{y}_n = 0$.

The parameter V_n characterises the solutions (see equation (6.4.7)). For $V_n \ll 1$ the displacements propagate quickly from the region $z_n = 0$.

For $V_n \ll 1$ the displacements are localised in the region $z_n = 0$.

The equation of motion, equation (6.4.10), was solved using two different methods. Appendix A3 describes the operational calculus approach, and Appendix A4 the numerical approach. Both methods gave solutions to within 5% of each other. Results quoted below are for constant velocity and external magnetic field; that is, k and $V_{m=1}$ are constant.

Fig.6.3 shows the solution of equation (6.4.10) at $z_n = 0$ as a function of the normalised velocity V_n. As V_n is increased the modulus of the first peak displacement, $|\hat{y}_n|$, increases. At the same time the delay between the current peak, at $t_n = \pi/2$, and the peak displacement, is reduced. In Fig.6.4 the peak displacement $\hat{y}_n$ is shown as a function of V_n. For $V_n = 0$, $\hat{y}_n = 0$. For $V_n \geq 3$, $\hat{y}_n \simeq -1$. Fig.6.5 shows the delay φ_n, in units of t_n, between the current and displacement peaks. For $V_n \ll 1$, $\varphi_n \to \infty$. For $V_n \gg 1$, $\varphi_n \to 0$.

The peak equilibrium displacement, given by equation (6.3.15) with $f(t) = \sin t_n$, is -1, reached in a time $t_n = \pi/2$. Fig.6.3 to Fig.6.5 show that as the normalised velocity is increased the plasma displacement approaches the equilibrium displacement; for $V_n \geq 3$ the two displacements are coincident.

Fig.6.6 shows the displacement y_n, as a function of z_n, for $V_n = 2$. The time between the peak displacements at $z_n = 0$ and $z_n = 0.67$ corresponds to a propagation velocity $V_n = 2$. At distances $z_n > 0.67$ the apparent velocity is complicated by the spatial distribution of the driving force ($f(z_n)$ in Fig.6.2).

Fig.6.7 shows the spatial dependence of the displacement y_n at different times. $t_n = 0.23$ corresponds to the time of peak displacement at $z_n = 0$. As t_n is increased the displacement spreads in distance

z_n, so that the wavelength increases. For early times the displacement follows the spatial distribution of the driving force ($f(z_n)$ in Fig.6.2).

6.4.3 Plasma Motion with a Crowbarred Current

The equation of motion, equation (6.4.3), was solved for the case of a crowbarred current in the loop producing the perturbing magnetic field:

$$I_d = I_o \sin \omega t ; \qquad t < t_c \qquad \ldots (6.4.11)$$

$$I_d = I_o \sin(\omega t_c) \exp\left(-\frac{(t - t_c)}{t_d}\right) ; \qquad t \geq t_c \qquad \ldots (6.4.12)$$

where t_c is the crowbar time and t_d is the decay time. Using the normalising equations, (6.3.17) to (6.3.19) and (6.4.6) to (6.4.9), the equation of motion can be written as

$$\frac{\partial^2 y_n}{\partial t_n^2} - V_n^2 \frac{\partial^2 y_n}{\partial z_n^2} = \begin{cases} -3 V_n^2 f(z_n) \sin t_n & t_n < t_{nc} \quad (6.4.13) \\ -3 V_n^2 f(z_n) \sin t_{nc} \exp\left(-\left(\frac{t_n - t_{nc}}{t_{nd}}\right)\right) ; & t_n \geq t_{nc} \quad (6.4.14) \end{cases}$$

where $t_{nc} = \omega t_c$ and $t_{nd} = \omega t_d$.

Fig.6.8 shows the displacement y_n as a function of time t_n, at $z_n = 0$ and 1.0, for a sinusoidal and crowbarred current. A time dependent external magnetic field, $B_e = \hat{B}_e \cos t_{no}$, is included, which affects the normalisation. For the cases shown,

$$\frac{t_{no}}{t_n} = 0.14 . \qquad \ldots (6.4.15)$$

This value was chosen as representing experimental conditions (see Section 7.6). The displacements produced by a sinusoidal current are shown as dashed lines. For the crowbarred current, with $t_n = \pi/2$ and $t_d = \infty$; that is,

$$I_d = I_o \sin \omega t ; \qquad t < t_c \qquad \ldots (6.4.16)$$

$$I_d = I_o ; \qquad t \geq t_c \qquad \ldots (6.4.17)$$

the displacements are shown as a full line. The equilibrium displacement $\eta_n(z_n, t_n)$ (see equation (6.3.15)) is also shown. For the crowbarred current case the plasma displacement approaches the equilibrium displacement

for $t_n \geqslant 2.5$. Because of the time varying external field B_e (see equation (6.4.15)), $|\eta_n|$ increases with time.

6.5 A THEORY FOR PLASMA MOTION DERIVED FROM THE $\bar{j}\times\bar{B}$ FORCES (THE MUTUAL INDUCTANCE THEORY)[68]

6.5.1 Introduction

An alternative model for calculating the plasma motion produced by a local perturbing magnetic field has been proposed by Junker et al[68]. A current I_d in the loop external to the plasma induces a current density j_2 in the plasma. If the plasma diamagnetic current density is j_0, the force per unit length acting on the plasma is

$$F = F_1(j_0, I_d) + F_2(j_0, j_2) + F_3(j_2, I_d) \qquad \ldots (6.5.1)$$

F_1 and F_2 are linear functions of I_d, but F_3 is quadratic in I_d because $j_2 \propto I_d$. The force F_1 is assumed to dominate; this is the force obtained by integrating $\bar{j}_0 \times \bar{B}_1$ ($\bar{B}_1$ is the perturbing field produced by the current I_d in the loop). A mutual inductance argument is used to evaluate this integral.

6.5.2 The Equation of Motion

Consider the geometry shown in Fig.6.1, but with rectangular coordinates (x,y,z). The force per unit length, F^1, acting on the plasma in a direction perpendicular to the axis, is

$$F^1 = j_0 \, I_d \frac{\partial M}{\partial x}, \qquad \ldots (6.5.2)$$

where M is the mutual inductance between the plasma and the current loop. If the perturbing field B_1 completely penetrates the plasma, then

$$M I_d = A_p \, B_{1z} \qquad \ldots (6.5.3)$$

where A_p is the plasma cross sectional area

B_{1z} is the axial component of the perturbing field on the plasma axis.

Using equation (6.5.3) the force F^1 (equation (6.5.2)) can be written

$$F^1 = j_o A_p \frac{\partial B_{z1}}{\partial x} \qquad \ldots (6.5.4)$$

If no currents flow within the plasma body, Maxwell's equation $\nabla \times \bar{B} = \mu_o \bar{j}$ gives

$$\frac{\partial B_{1z}}{\partial x} = \frac{\partial B_{1x}}{\partial z} \qquad \ldots (6.5.5)$$

The plasma diamagnetic current j_o can be expressed in terms of the internal and external fields as

$$\mu_o j_o = -(B_e - B_i)$$

$$= -B_e(1 - \sqrt{1-\beta}) \qquad \ldots (6.5.6)$$

Using equations (6.5.6), (6.5.5) and (6.5.4) the force F^1 can be written

$$F^1(z,t) = -\frac{A_p B_e}{\mu_o}\left(1 - \sqrt{1-\beta}\right)\frac{\partial B_{1x}}{\partial z} \; . \qquad \ldots (6.5.7)$$

The magnetic field at a distance b from an n turn current loop of area A_d and current I_d can be derived from the vector potential A^1_θ in equation (6.3.7), using $\bar{B} = \nabla \times \bar{A}$:

$$B_{1x} = \frac{3\mu_o n A_d I_d \, bz}{4\pi (b^2 + Z^2)^{\frac{5}{2}}} \; . \qquad \ldots (6.5.8)$$

Substituting for B_{1x} from equation (6.5.8) into equation (6.5.7) gives

$$F^1(z,t) = -\frac{3 n I_d A_d A_p B_e (1-\sqrt{1-\beta})\,(1 - 4(z/b)^2)}{4\pi b^4 \qquad (1 + (z/b)^2)^{\frac{7}{2}}} \ldots (6.5.9)$$

The plasma equation of motion is then given by the equation for a straight theta pinch (equation (6.2.9)) with an additional forcing term:

$$\frac{\partial^2 y^1}{\partial t^2} - V^2_{m=1} \frac{\partial^2 y^1}{\partial z^2} = \frac{F^1(z,t)}{M} \qquad \ldots (6.5.10)$$

where y^1 is the displacement

M is the line mass

$V_{m=1} = V_A \sqrt{2-\beta}$.

The assumptions of the theory are:

(1) The field B_1 completely penetrates the plasma.

(2) $\nabla \times \bar{B}_1 = 0$; that is the plasma does not perturb the vacuum field.

(3) The loop can be considered to produce a magnetic dipole field; that is, $b \gg r_d$, where r_d is the loop radius.

6.5.3 The Solution of the Equation of Motion

The equation of motion, equation (6.5.10), can be written in normalised units. For a sinusoidal loop current $I_d = I_o \sin \omega t$, equation (6.5.10) becomes:

$$\frac{\partial^2 y_n^1}{\partial t_n^2} - V_n^2 \frac{\partial^2 y_n^1}{\partial z_n^2} = -3 f(z_n) \sin t_n \qquad \ldots (6.5.11)$$

where

$$y_n^1 = \frac{y^1}{k^1} \qquad \ldots (6.5.12)$$

$$k^1 = \frac{n I_o A_d A_p B_e (1 - \sqrt{1-\beta})}{4\pi M b^4 \omega^2} \qquad \ldots (6.5.13)$$

$$z_n = \frac{z}{b} \qquad \ldots (6.5.14)$$

$$t_n = \omega t \qquad \ldots (6.5.15)$$

$$f(z_n) = \frac{(1 - 4(z/b)^2}{(1 + (z/b)^2)^{\frac{7}{2}}} \qquad \ldots (6.5.16)$$

The spatial distribution of the driving force $F^1(z,t)$, described by $f(z_n)$, is the same as that for the equilibrium model, and is shown in Fig.6.2. Equation (6.5.11) was solved using the methods given in Appendix A3 and Appendix A4. Fig.6.9 shows the first peak displacement, $\hat{y}_n^1$, at $z_n = 0$, as a function of the normalised velocity V_n. For $V_n \ll 1$, $\hat{y}_n^1 \to -6\pi$. For $V_n \gg 1$, $\hat{y}_n^1 \propto V_n^{-2}$. Therefore the theory predicts a finite displacement with no propagation velocity; the displacement decreases as the velocity increases.

6.6 A COMPARISON BETWEEN THE EQUILIBRIUM AND THE MUTUAL INDUCTANCE THEORY PREDICTIONS

Both theories (see Sections 6.4 and 6.5) result in an equation of motion which can be written as the wave equation with an additional distributed driving force $F(z,t)$. For the equilibrium theory (see equation (6.4.4))

$$\frac{F(z,t)}{M} = - \frac{6\mu_o n A_d I_d V_{m=1}^2}{4\pi b^4 B_e} \cdot \frac{(1-4(z/b)^2)}{(1+(z/b)^2)^{\frac{7}{2}}} \qquad \ldots (6.6.1)$$

For the mutual inductance theory (see equation (6.5.9))

$$\frac{F^1(z,t)}{M} = - \frac{3 n A_d I_d A_p B_e(1-\sqrt{1-\beta})}{4\pi b^2 M} \cdot \frac{(1-4(z/b)^2)}{(1+(z/b)^2)^{\frac{7}{2}}} \qquad \ldots (6.6.2)$$

The ratio of the two forcing terms is

$$\frac{F(z,t)}{F^1(z,t)} = \frac{2 V_{m=1}^2 \mu_o M}{A_p B_e^2 (1-\sqrt{1-\beta})} = \frac{2(2-\beta)}{(1-\sqrt{1-\beta})} . \qquad \ldots (6.6.3)$$

The main differences between the predictions of the two models are

(1) $V_n = 0$. The equilibrium theory predicts no displacement. The mutual inductance theory predicts a normalised peak displacement $\hat{y}_n^1 = -6\pi$ (see Fig.6.9).

(2) $V_n \gg 1$. The equilibrium theory predicts $\hat{y}_n \to -1$ (see Fig.6.4). The mutual inductance theory predicts $\hat{y}_n^1 \propto V_n^{-2}$ (see Fig.6.9).

(3) $\beta \ll 1$. The equilibrium theory predicts a finite displacement. The mutual inductance theory predicts $\hat{y}_n^1 \to 0$.

6.7 SUMMARY

Two theories which describe the plasma motion produced by the field of a nearby current loop have been described. Both were based on the Haas and Wesson stability analysis of a theta pinch.

The equilibrium theory[79] estimated the restoring force on the plasma when the equilibrium position was displaced. An expression for the equilibrium position was derived in terms of the vector potentials of the perturbing and unperturbed fields. Allowing small oscillations about

the equilibrium resulted in an equation of motion, which was solved analytically and numerically. The plasma displacement, a function of the axial position, time and propagation velocity, was found to follow the equilibrium for large velocities. As the velocity was reduced the plasma displacement decreased, until for zero velocity, zero displacement was found.

The mutual inductance theory[68] estimated the $\bar{j}\times\bar{B}$ forces acting on the plasma by considering the field coupling between the loop and the plasma. An equation of motion similar to that of the equilibrium theory was derived. For zero propagation velocity a finite displacement was predicted; this displacement varied as V_n^{-2} for large velocities V_n. No displacements were predicted for a low β plasma, where the diamagnetic current approaches zero.

a) THE CURRENT LOOP (DIPOLE) GEOMETRY

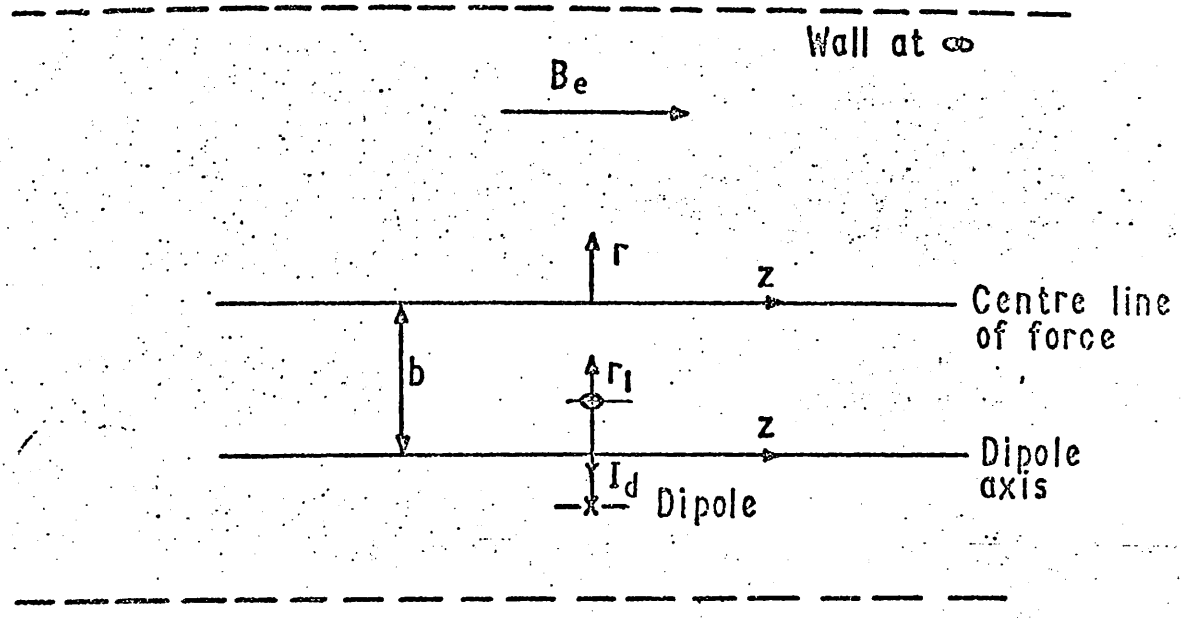

b) THE PLASMA AND EQUILIBRIUM COORDINATES

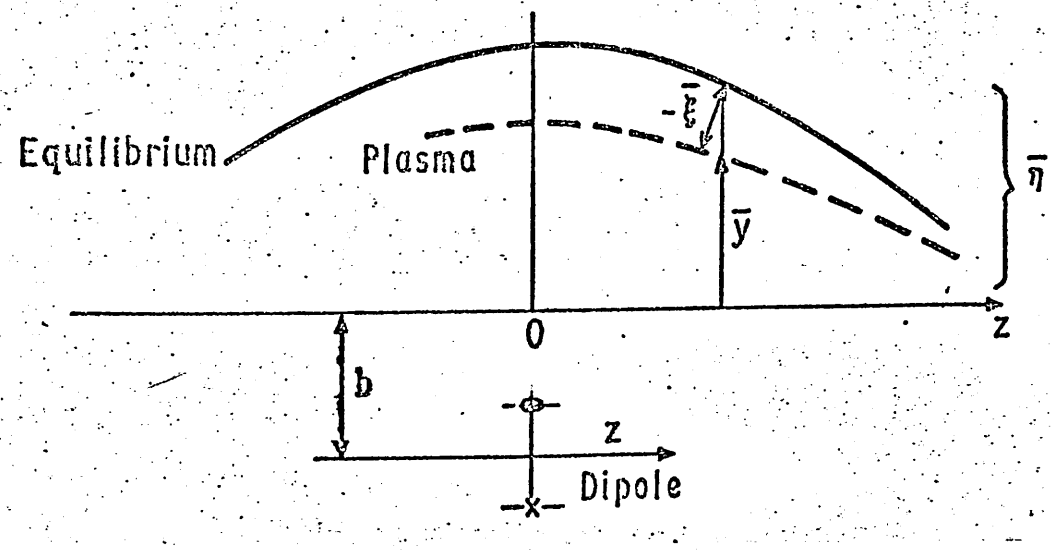

Fig.6.1
The plasma and equilibrium geometry

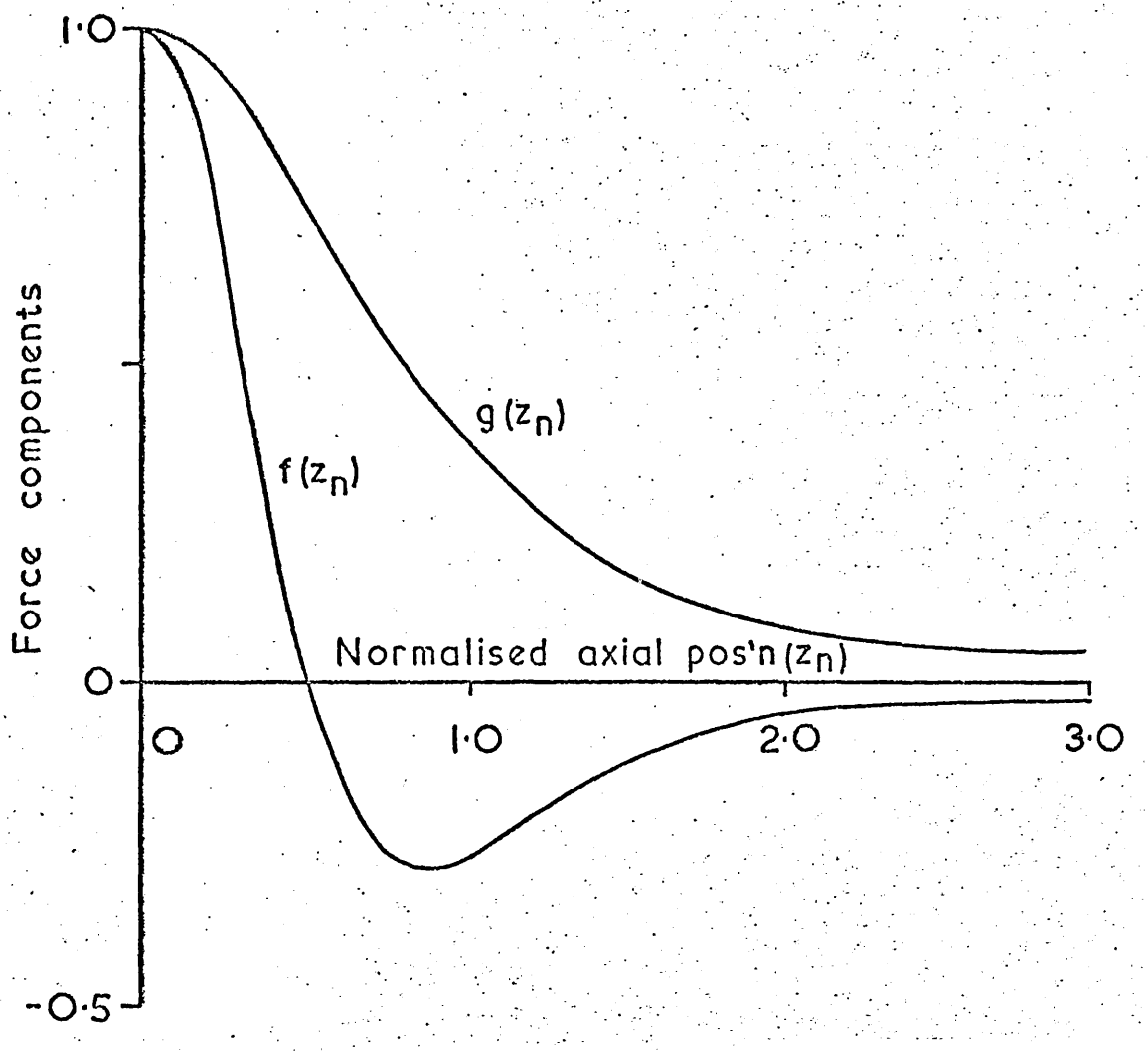

Fig.6.2

The spatial dependence of the equilibrium position $g(z_n)$ and the forcing function $f(z_n)$

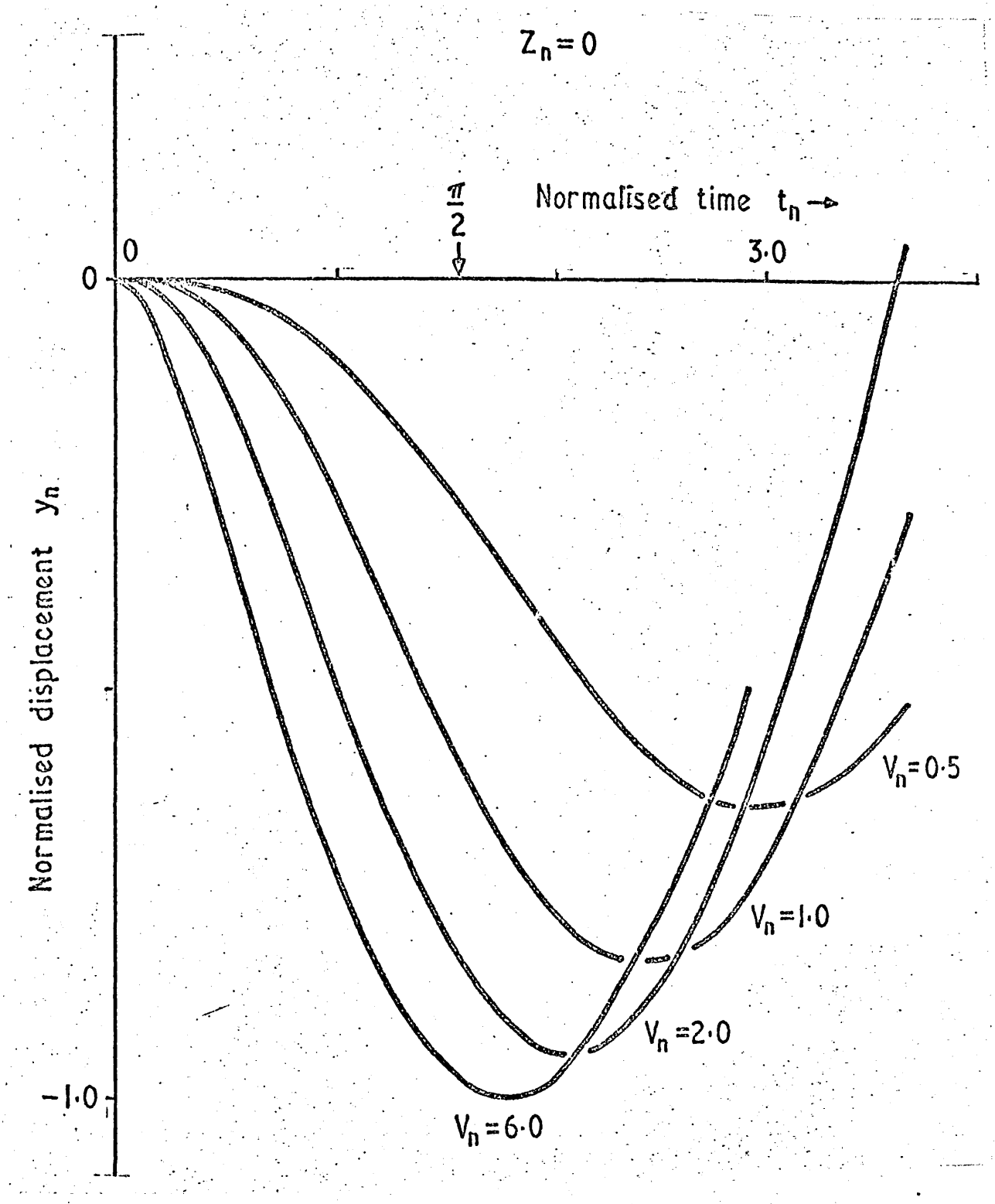

Fig.6.3

The normalised displacement as a function of the normalised time t_n and normalised velocity V_n

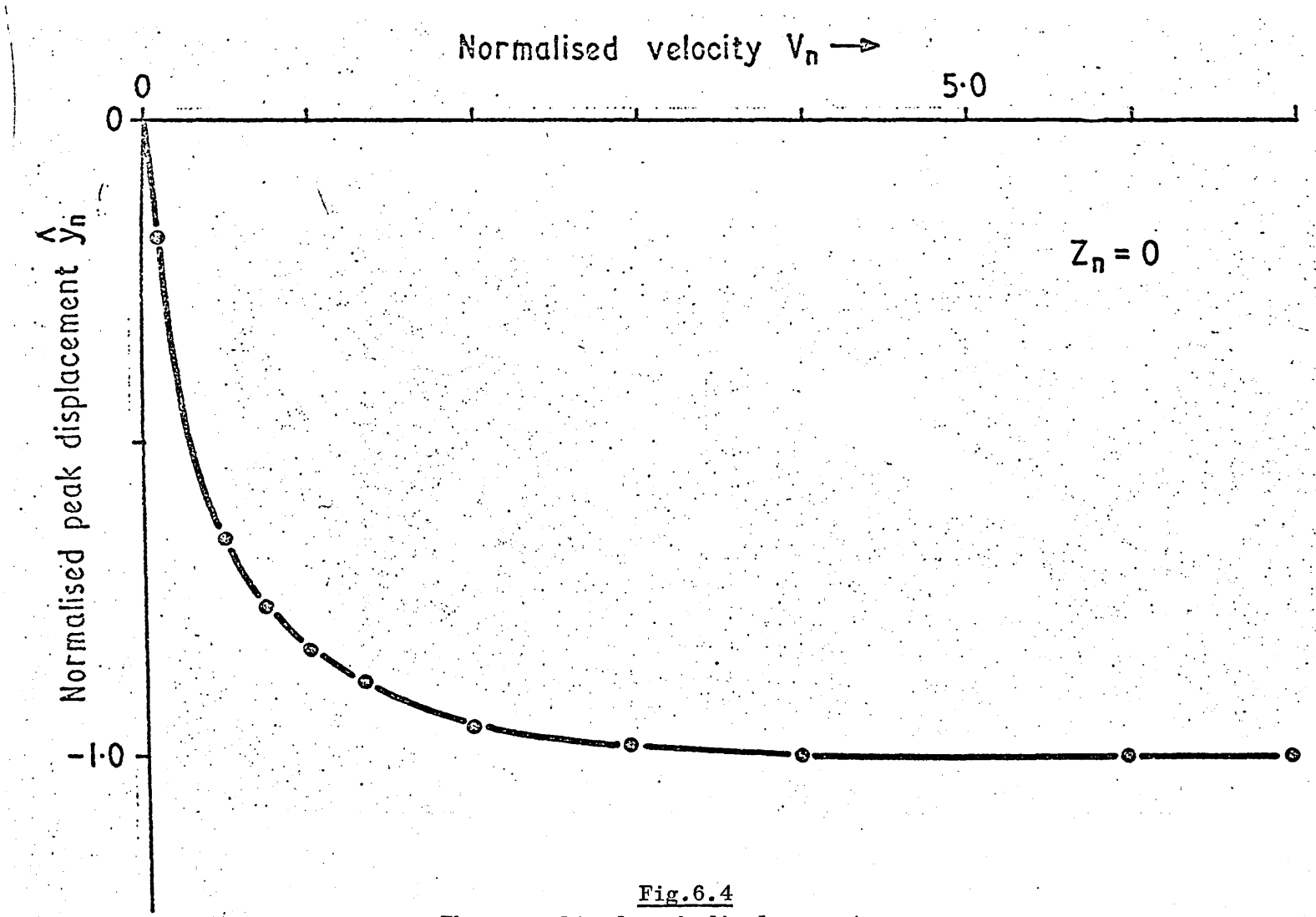

Fig.6.4
The normalised peak displacement as a function of the normalised velocity

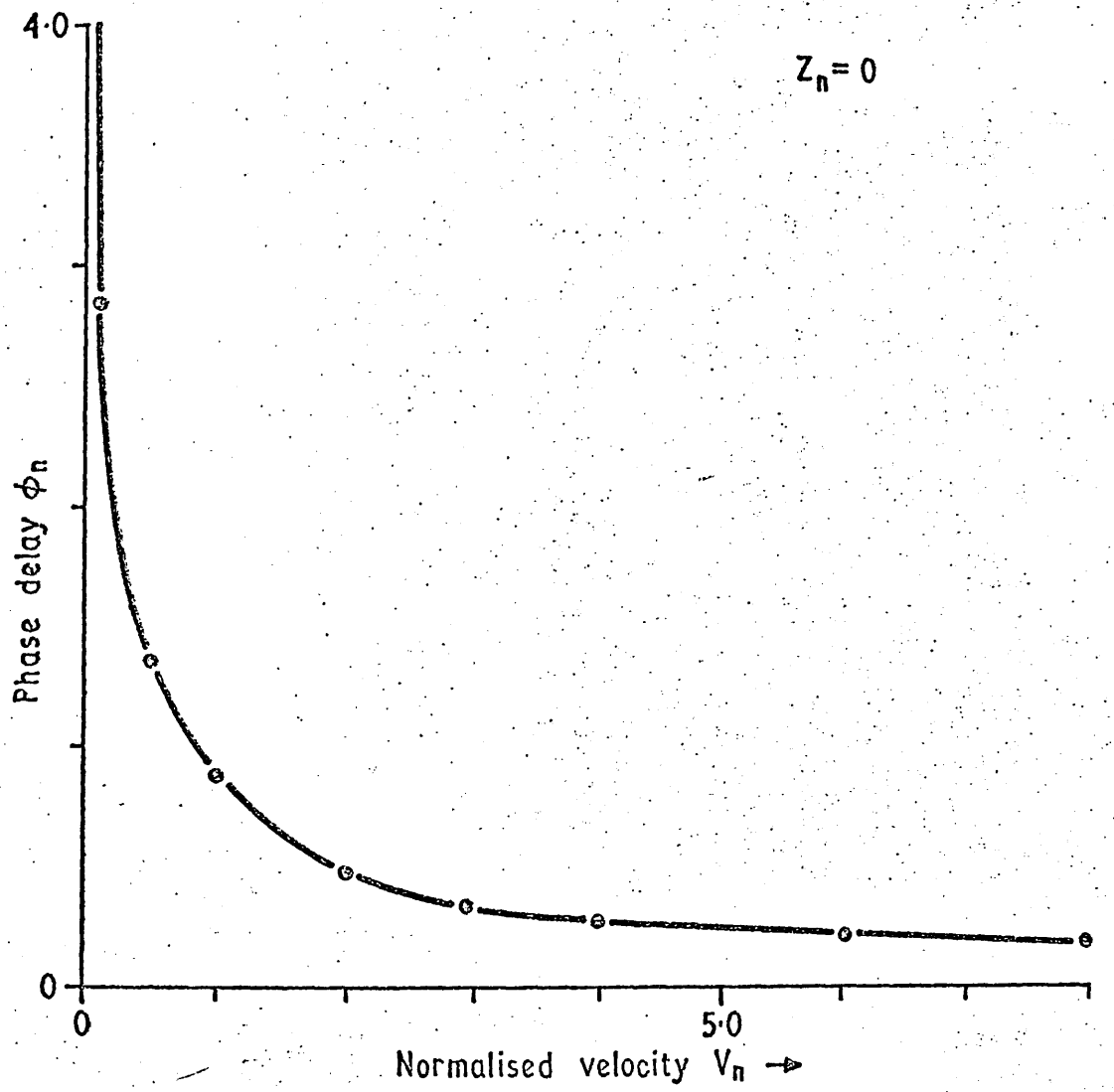

Fig.6.5
The phase delay against the normalised velocity

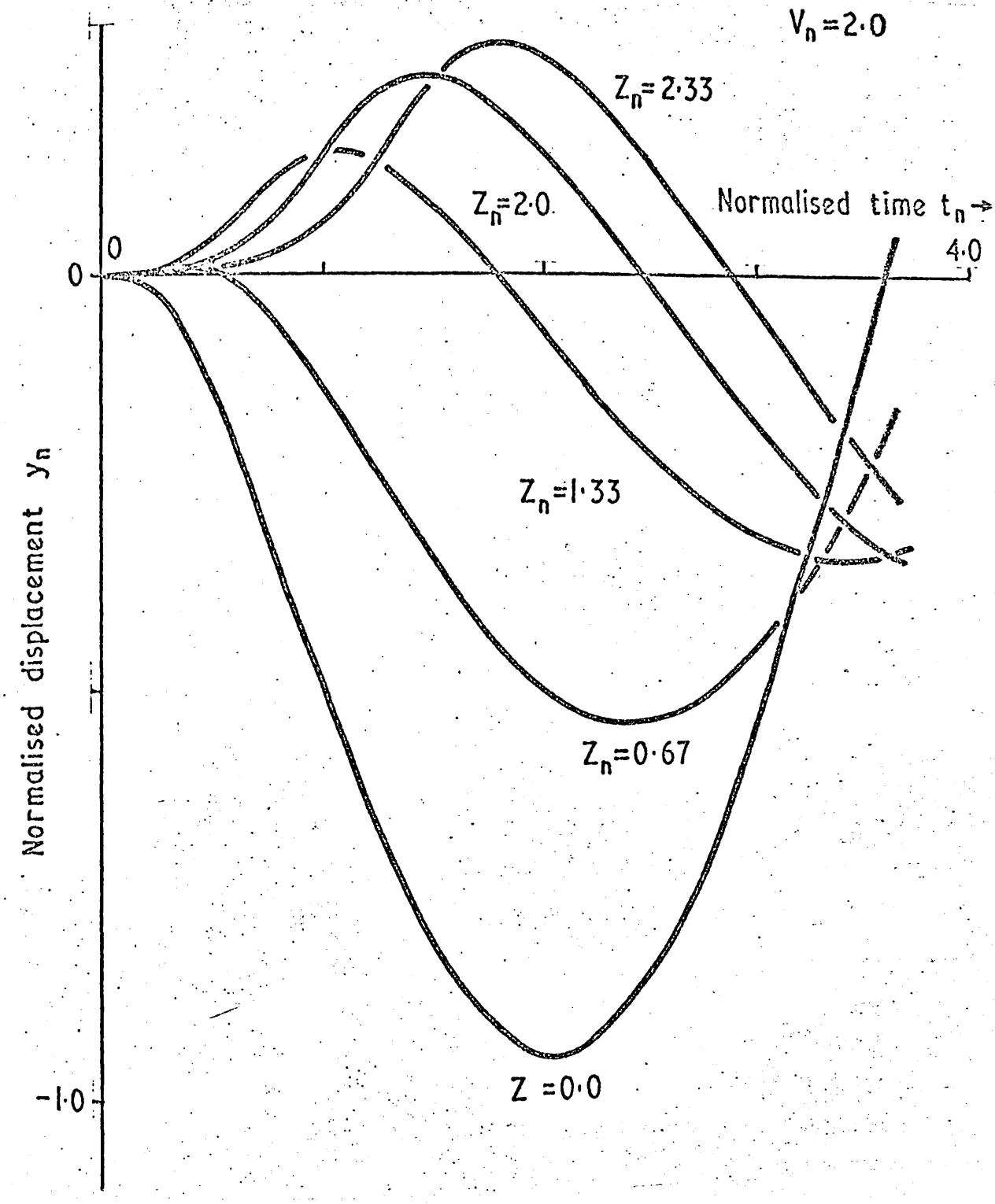

Fig.6.6

The normalised displacement as a function of axial position z_n and time t_n

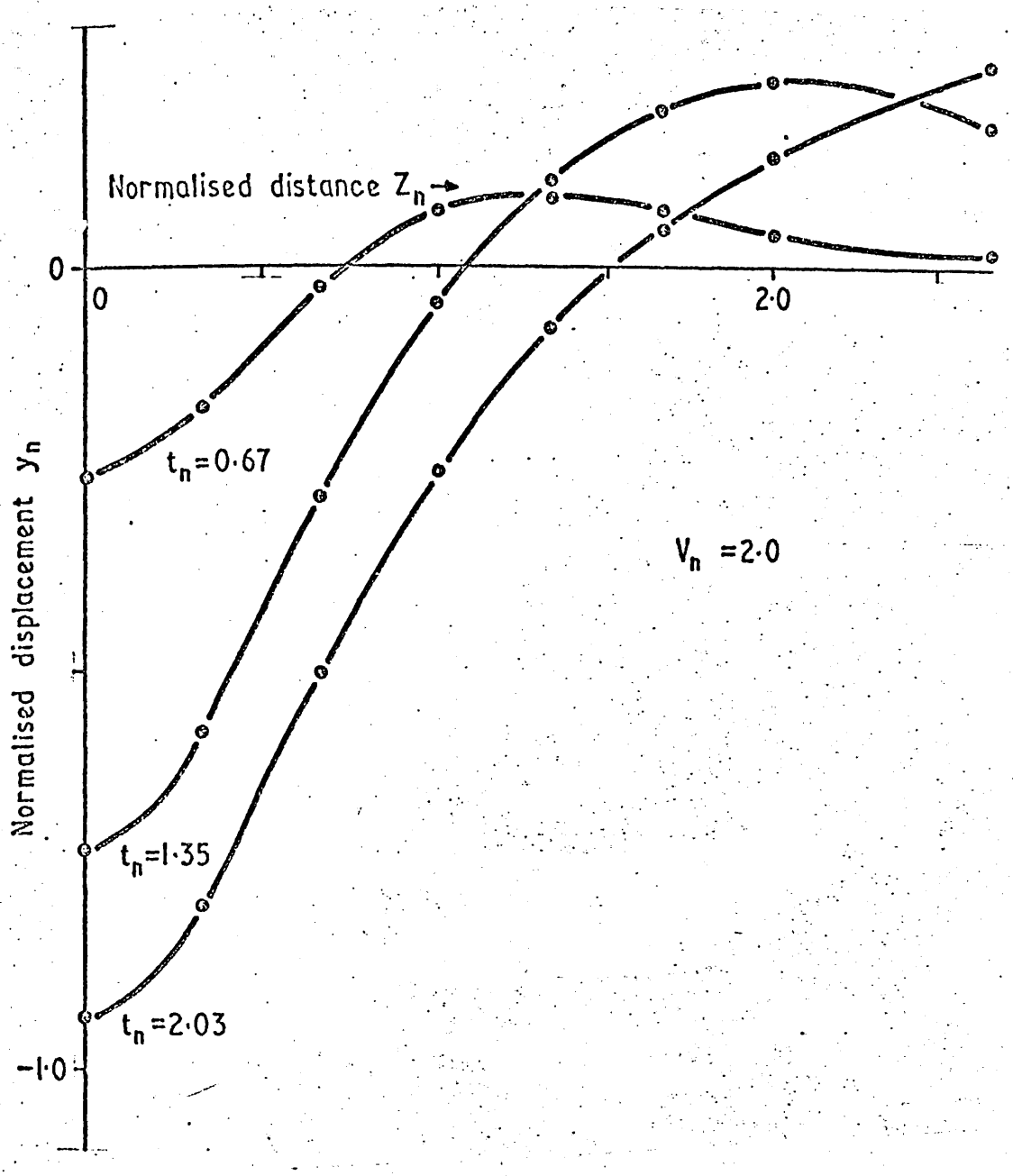

Fig.6.7

The spatial dependence of the normalised displacement as a function of time

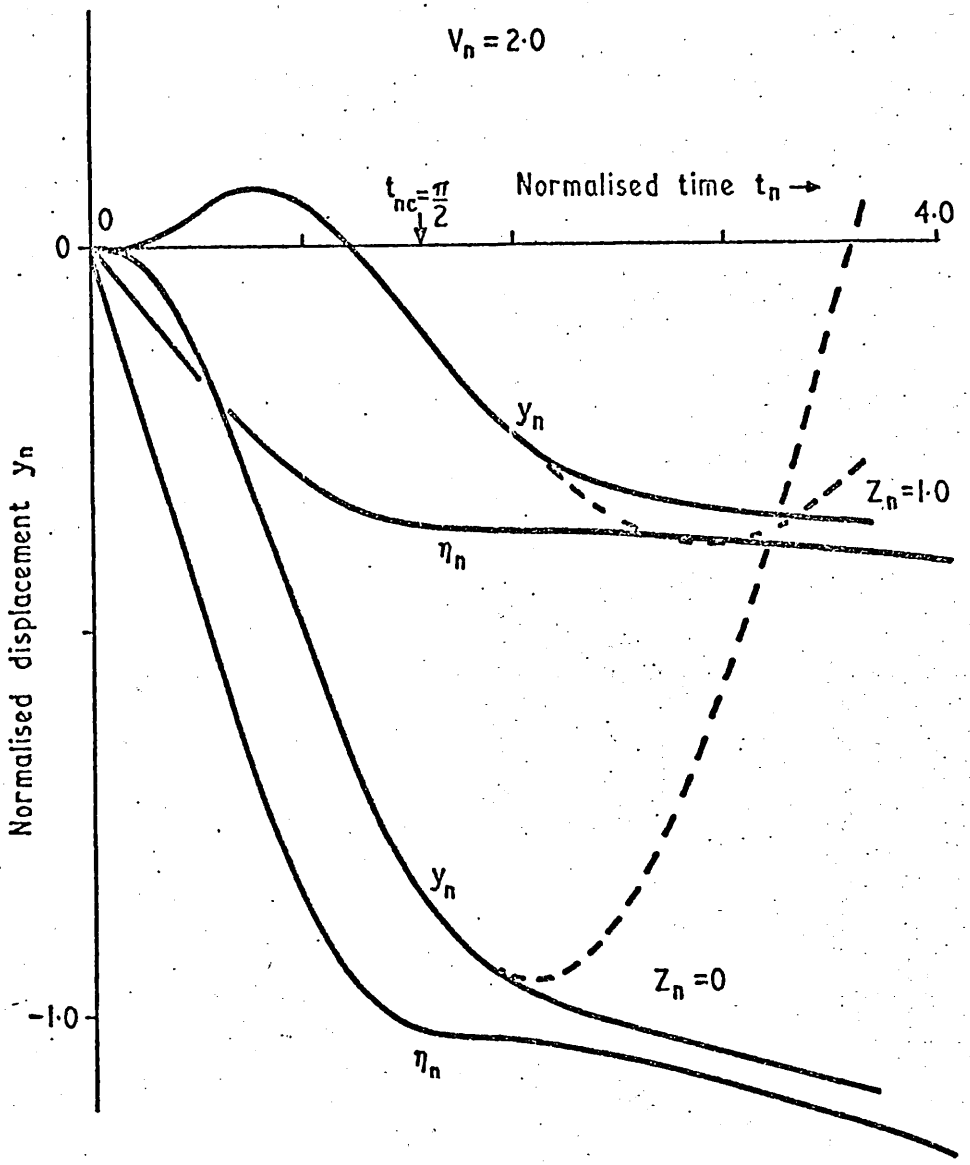

y_n Full line - Plasma displacement, crowbarred current
y_n Broken line - Plasma displacement, sin. current
η_n Full line - Equilibrium displacement, crowbarred current

Fig.6.8
Plasma and equilibrium displacements for sinusoidal and crowbarred loop currents

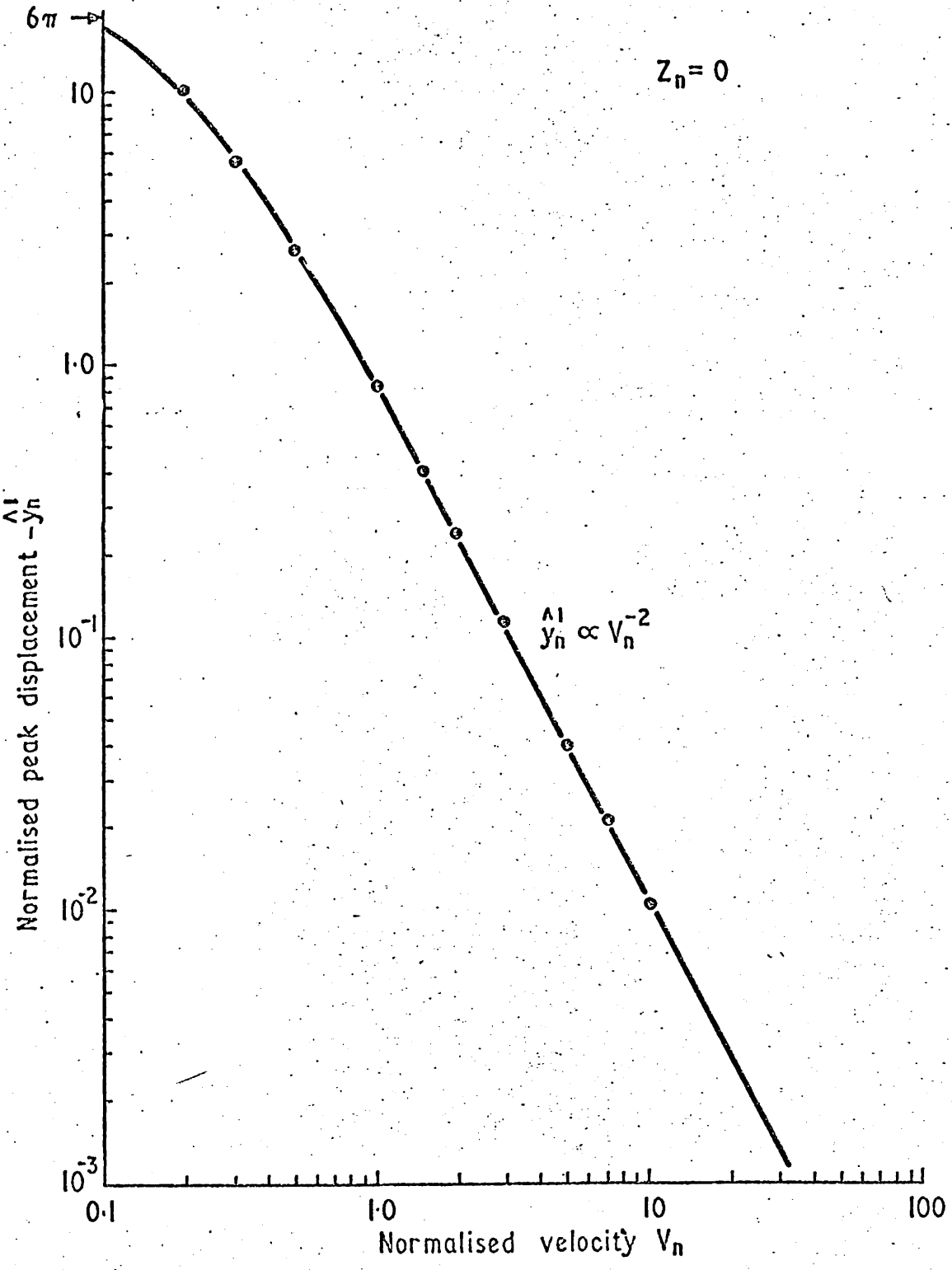

Fig.6.9

The peak displacement as a function of the normalised velocity (the mutual inductance theory)

CHAPTER VII

AN EXPERIMENTAL STUDY OF THE PLASMA MOTION PRODUCED BY A PERTURBING MAGNETIC FIELD

7.1 INTRODUCTION

The experiments performed on two theta pinch plasmas to determine the effect of a perturbing magnetic field produced by a current carrying coil are described. The coil design and the fields produced are described. High speed photographic techniques were used to measure the plasma displacement, propagation velocity and spatial damping. Results are presented for a high beta[79] (the 3.5 m thetatron) and a low beta[68] (the 2 m thetatron) plasma.

7.2 THE DIAGNOSTIC TECHNIQUES

The standard diagnostic techniques used are described in Appendix A2. Plasma properties were obtained from diamagnetic signals and intensity profiles. Plasma motion was measured as the movement of the maximum light intensity position, recorded on a streak photograph (see Section A2.6) and measured with a microdensitometer to an accuracy $\pm$ 0.05 cm. Other experimental errors are given in Fig.A2.2.

7.3 THE SECTOR COIL

A small coil, called a sector coil, was placed between the compression coil and the vacuum tube at the midplane of the 2 m and 3.5 m thetatrons (see Chapter III). Fig.7.1(a) and 7.1(b) show a front view and cross section of the sector coil inside the thetatron. The flux guide in the 3.5 m thetatron did not extend into the central region (see Fig.3.2(a)), so that the sector coil area was not restricted.

Both theories presented in Chapter VI predict that an n turn current loop, area A_d and current I_o, produces a force F on a plasma (see equations (6.6.1) and (6.6.2)) :

$$F \propto n A_d I_o \quad . \qquad \ldots (7.3.1)$$

Certain sector coil design criteria can be derived, assuming that equation (7.3.1) is valid.

If a sector coil of inductance L is energised by a capacitor bank of capacitance C charged to a voltage V, the maximum current in the coil, I_o, is

$$I_o = V\sqrt{\frac{C}{L}} \quad . \qquad \ldots (7.3.2)$$

The inductance of an n turn coil can be expressed approximately as

$$L = n^2 L_o \qquad \ldots (7.3.3)$$

where L_o is the inductance of 1 turn. Substituting for L from equation (7.3.3) and I_o from equation (7.3.2) into equation (7.3.1) gives

$$F \propto A_d V\sqrt{\frac{C}{L_o}} \quad . \qquad \ldots (7.3.4)$$

Therefore the maximum force produced by an n turn coil is independent of the number of turns, but directly proportional to the area. The number of turns controls the period of oscillation. At least two complete current oscillations were required for the experiments described in Section 7.5 and 7.6. Because the plasma lifetime was restricted to 15 μs the number of turns was restricted to 5 or less.

Two 3 turn sector coils were wound from SWG 16 copper wire, insulated with polythene. Each coil was 0.7 cm wide, and occupied one quarter of the area between the compression coil and the vacuum tube (see Fig.7.1(b)) at the midplane. Five capacitor banks were used to energise the coils; two on the 2 m thetatron and three on the 3.5 m thetatron. The sector coil circuit parameters are tabulated in Fig.7.2. Typical currents were 20 kA, with periods of 5 μs.

7.4 THE SECTOR COIL MAGNETIC FIELDS

The magnetic fields produced by sector coil circuit 4 (see Fig.7.2) were measured using small search coils (see Section A2.4). Fig.7.3 shows the experimental values of B_z and $B_\perp$, the components of field along and perpendicular to the tube axis, as functions of the axial distance z from the coil. (Coordinates z and x in Fig.7.1(a).) The solid lines represent the analytic solution for the fields produced on the compression coil axis by a magnetic dipole of moment M:

$$M = n A_d I_d . \qquad \ldots (7.4.1)$$

These fields can be derived from the vector potential (see equation (6.3.7)), and are

$$B_z(z) = \frac{\mu_o}{4\pi} \frac{M(2z^2 - b^2)}{(z^2 + b^2)^{\frac{5}{2}}} \qquad \ldots (7.4.2)$$

$$B_\perp(z) = \frac{3\mu_o}{4\pi} \frac{M z b}{(z^2 + b^2)^{\frac{5}{2}}} \qquad \ldots (7.4.3)$$

where b is the distance between the dipole axis and the compression coil axis, = 5.6 cm. The analytic expressions underestimated the fields produced; this is discussed in Section 8.2.7. The characteristic axial length was about 5 cm.

7.5 THE EXPERIMENTS WITH A LOW BETA PLASMA[68]

The 2 m thetatron, described in Section 3.7, was operated with filling pressures of 10 and 20 mtorr of hydrogen, and a main capacitor bank voltage of 34 kV. This produced a peak axial magnetic field of 14 kG in 9 μs. Fig.7.4 tabulates the plasma average beta, temperature and area as functions of the filling pressure and time. At both filling pressures the peak temperature was about 10 eV, and the average beta $\leqslant 0.1$. The plasma radius reached a minimum before the magnetic field reached a maximum; therefore the plasma diffused across the field lines. These characteristics were thought to be caused by impurities (see Section 5.3.2). Each plasma used for experiments was reproducible and MHD stable for 10 μs.

The effect of energising sector coil system 1 (see Fig.7.2) 1.0 μs after the start of the azimuthal compression current is shown in Fig.7.5. Fig.7.5(a) shows the sector coil and compression coil current waveforms. Fig.7.5(b) shows a stereoscopic streak picture, taken at 45° above and 55° below the compression coil axis (see Fig.7.1(b)), with no sector coil current. The plasma was straight. Fig.7.5(c) shows a stereoscopic streak photograph when the sector coil was energised. A gross plasma motion was found in the $\pm x$ direction (see Fig.7.1(a)). No rotation occurred. Sector coil currents in the $-\theta$ direction produced plasma displacements in the $+x$ direction; currents in the $+\theta$ direction produced displacements in the $-x$ direction.

Fig.7.6 shows streak pictures taken of the plasma motion in the $\pm x$ direction when sector coil system 2 (see Fig.7.2) was energised 1.0 μs after the compression current. The motion at 3 axial positions, $z = 0$, 5.3 and 10.8 cm, is shown for the 10 mtorr and 20 mtorr plasmas (see Fig.7.4). A maximum displacement of about one plasma radius was produced at $z = 0$ cm by a sinusoidal sector coil current of 16 kA. At $z = 5.3$ cm the displacement was about 10% of that at $z = 0$ cm. No motion was detected at 10.8 cm. These streak pictures were taken on a shot to shot basis; each photograph was reproducible to within the experimental errors.

For times less than 1 μs after the implosion the intensity profiles were flat, making analysis of the motion difficult. The delay between the compression coil and sector coil currents was increased to 4.0 μs; the plasma intensity profiles were then more peaked (see Fig.4.3) so that the displacement, measured by a microdensitometer, was more accurate. Fig.7.7 shows the measured displacement at $z = 0$ cm when sector coil system 2 was energised 4.0 μs after the compression current, for a 20 mtorr plasma (see Fig.7.4). A 16 kA sinusoidal current produced a 0.4 cm oscillating plasma displacement approximately in phase with the sector coil current.

7.6 THE EXPERIMENTS WITH A HIGH BETA PLASMA[79]

The 3.5 m thetatron (see Chapter III) was used to produce a high β plasma for experiments on perturbed motion. Fig.7.8 tabulates the measured plasma parameters as functions of the initial conditions (see Chapter IV). Four different plasmas were used. With no bias field (see Section 2.7) the compression current was initiated 2 μs before the end of the axial preionization current, with the main capacitor bank charged to 35, 40 and 45 kV. The plasmas produced had values of $\langle\beta\rangle \simeq 0.4$, and temperatures $\simeq 50$ eV. Decreasing the charging voltage increased the temperature (see Section 5.4.5). A negative bias field $B_1 = -350$ G was used, with the compression current initiated at the preionization current zero, to produce a plasma with an approximately time independent beta value. Each plasma used was MHD stable and reproducible for at least 15 μs.

Sector coil systems 3, 4 and 5 (see Fig.7.2) were used to excite plasma motion. Stereoscopic streak pictures showed that the plasma motion was always in the $\pm x$ direction (see Fig.7.1(a)), and that the plasma radial density profiles were not distorted.

The three plasmas produced without a bias field (see Fig.7.8) were perturbed using sector coil systems 3 and 4 (see Fig.7.2), with delays between the compression current and sector coil current of 1.0 and 4.0 μs. Plasma displacements were measured at four axial positions, $z = 0, 4, 8$ and 12 cm, as functions of the sector coil current and plasma parameters.

Fig.7.9 shows streak photographs of the plasma motion in the $\pm x$ direction when sector coil system 4 was energised 1 μs after the compression current, with the main capacitor bank charged to 45 kV (plasma 1, Fig.7.8). Pictures a to d were recorded at $z = 0$ to 12 cm, with a peak sector coil current of -15.5 kA. A time delay between the displacement maxima at different axial positions showed that propagation occurred.

Fig.7.10 shows the measured plasma displacements obtained by scanning the photographs in Fig.7.9 with a microdensitometer. The peak displacement at $z = 0$ cm was 0.6 cm. A propagation velocity of 16 cm μs^{-1} was measured over an axial distance of 8 cm.

The peak displacement at $z = 0$ cm, and the propagation velocity, obtained using sector coil systems 3 and 4 (see Fig.7.2) on plasmas 1, 2 and 3 (see Fig.7.8), are tabulated in Fig.7.11. Peak displacements decreased as the main capacitor bank voltage was increased; that is, when the external axial field was increased. Increasing the sector coil current delay from 1.0 μs to 4.0 μs reduced the displacement but increased the propagation velocity. Changing from sector coil circuit 3 to 4 increased the sector coil current from 10.5 to 20.6 kA, and decreased the frequency from 2.7 to 1.35 rad μs^{-1} (see Fig.7.2). The displacements obtained with circuit 4 were twice those obtained with circuit 3; the propagation velocity was changed less than the experimental errors of 15%.

The peak displacement at $z = 0$, $\hat{y}$, was measured as a function of the sector coil current I_0, frequency ω, and the plasma parameters. Fig.7.12 shows $\hat{y}$ as a function of I_0 for sector coil circuit 4, with plasmas 1, 2 and 3 (see Fig.7.8). A linear relationship was found between $\hat{y}$ and I_0 for constant plasma conditions; that is, for fixed voltage and delay. Fig.7.13 shows $\hat{y}$ as a function of I_0 for sector coil circuit 3; again $\hat{y}$ was linearly dependent on I_0 for constant plasma conditions. Changing the direction of the sector coil current reversed the direction of $\hat{y}$, but did not change its absolute value.

Plasma 4 (see Fig.7.8), produced with a negative bias field, was excited by sector coil circuit 5 (see Fig.7.2) energised 5 μs after the compression current. The sector coil current ($I_0 = 22$ kA, $\omega = 1.25$ rad μs^{-1}) was either allowed to oscillate, or was crowbarred at current maximum by a

metal to metal switch to produce an approximate step current waveform. Fig.7.14 shows the streak photographs taken at $z = 0$ cm and the current waveforms with (a) no sector coil current, (b) a sinusoidal current, and (c) a crowbarred current. Fig.7.15 shows the measured plasma displacements at $z = 0$ cm and 4 cm. With the crowbarred current, which decayed with an e-folding time of 15 μs, the plasma moved outwards to a position equal to that when a sinusoidal current was used, and then relaxed towards the axis in a time greater than the remaining plasma lifetime of 8 μs. Peak displacements of 0.6 cm and velocities of 30 cm μs^{-1} were observed.

A spatial damping of the propagating plasma displacements was found (see Fig.7.9). Measurements of the displacement produced by a sinusoidal sector coil current were used to derive an e-folding damping length. The results, tabulated in Fig.7.16, show that doubling the current frequency reduced the damping length, typically 15 cm, by about 10%. Decreasing the main capacitor bank voltage decreased the damping length.

7.7 SUMMARY

A current loop (sector coil) near a theta pinch produced gross plasma displacements in the plane of the loop axis and the compression coil axis. No plasma rotation or distortion of the radial density profile was observed.

A 3 turn sector coil current of 16 kA produced a peak displacement of 0.4 cm in a low beta, 10 eV plasma. At axial positive greater than 5 cm from the plane of the sector coil the plasma displacement was less than 10% of the maximum displacement.

A 3 turn sector coil current of 21 kA produced a peak displacement of 0.6 cm in a high beta, 50 eV plasma, which propagated axially away from the plane of the coil[79]. The peak plasma displacement was proportional to the coil current, and decreased as the external axial magnetic field was increased. Sinusoidal currents produced oscillating displacements; a

step current caused the plasma to move to an equilibrium position which was displaced from the initial unperturbed equilibrium position.

Propagation velocities measured with high beta plasmas were between 15 and 30 cm μs^{-1}; they increased as the delay between the compression current and the sector coil current was increased. A spatial damping of the propagating displacements was measured; typical e-folding lengths were 15 cm. This length was reduced by 10% when the sector coil current frequency was doubled.

(a) FRONT VIEW

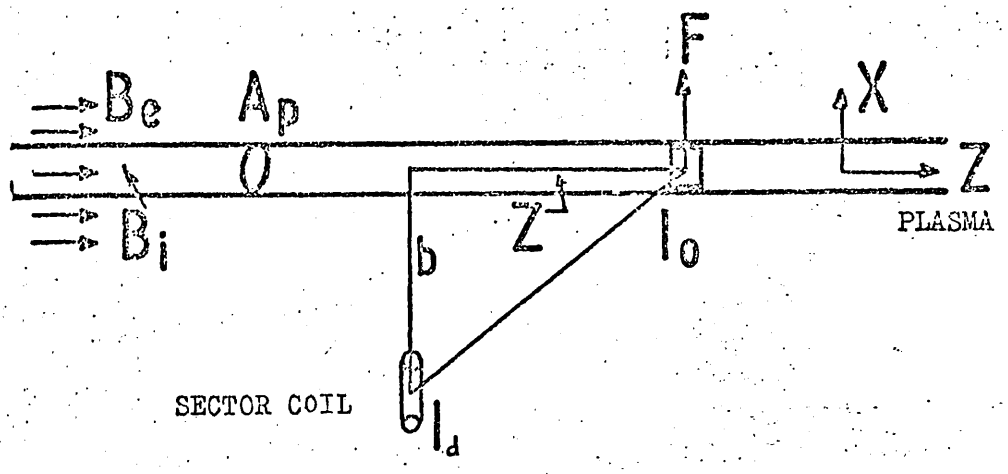

(b) CROSS SECTION

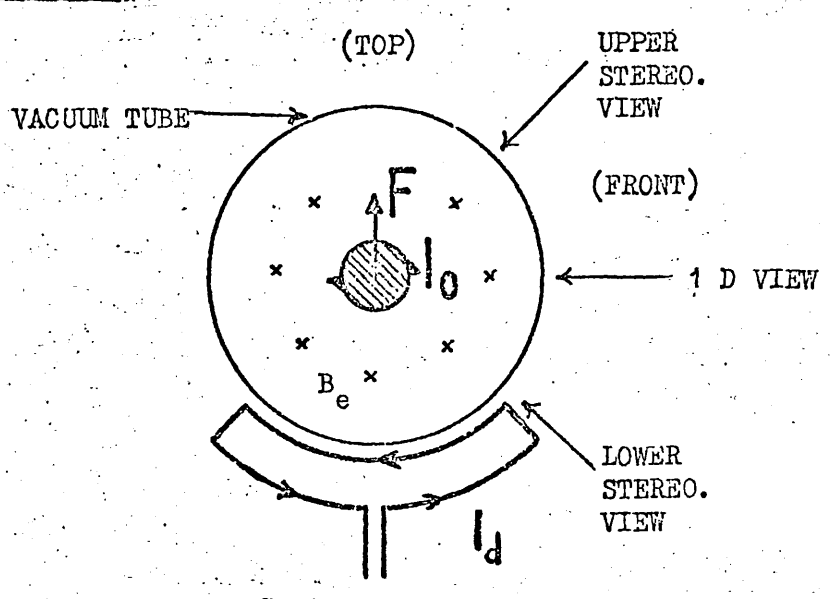

Sector coil with current in $-\theta$ direction

Fig.7.1

Diagrams of the sector coil geometry

Thetatron	2 m		3.5 m		
Text Ref. No.	1	2	3	4	5
C (μF)	0.1	0.4	0.1	0.4	0.5
V (kV)	40	40	40	40	40
Ad (cm^3)	28	28	16	16	16
b (cm)	6.0	6.0	5.6	5.6	5.6
n	3	3	3	3	3
I_o (kA)	8.4	16.0	10.5	20.6	22.0
ω(rad μs^{-1})	2.2	1.1	2.7	1.35	1.25
L_T (μH)	2.15	2.15	1.37	1.37	1.37
L_c (μH)	1.8	1.8	1.1	1.1	1.1
Q	20	10	34	16.7	15

L_T is the total circuit inductance

L_c is the inductance of the coil

Fig.7.2

The sector coil circuit parameters

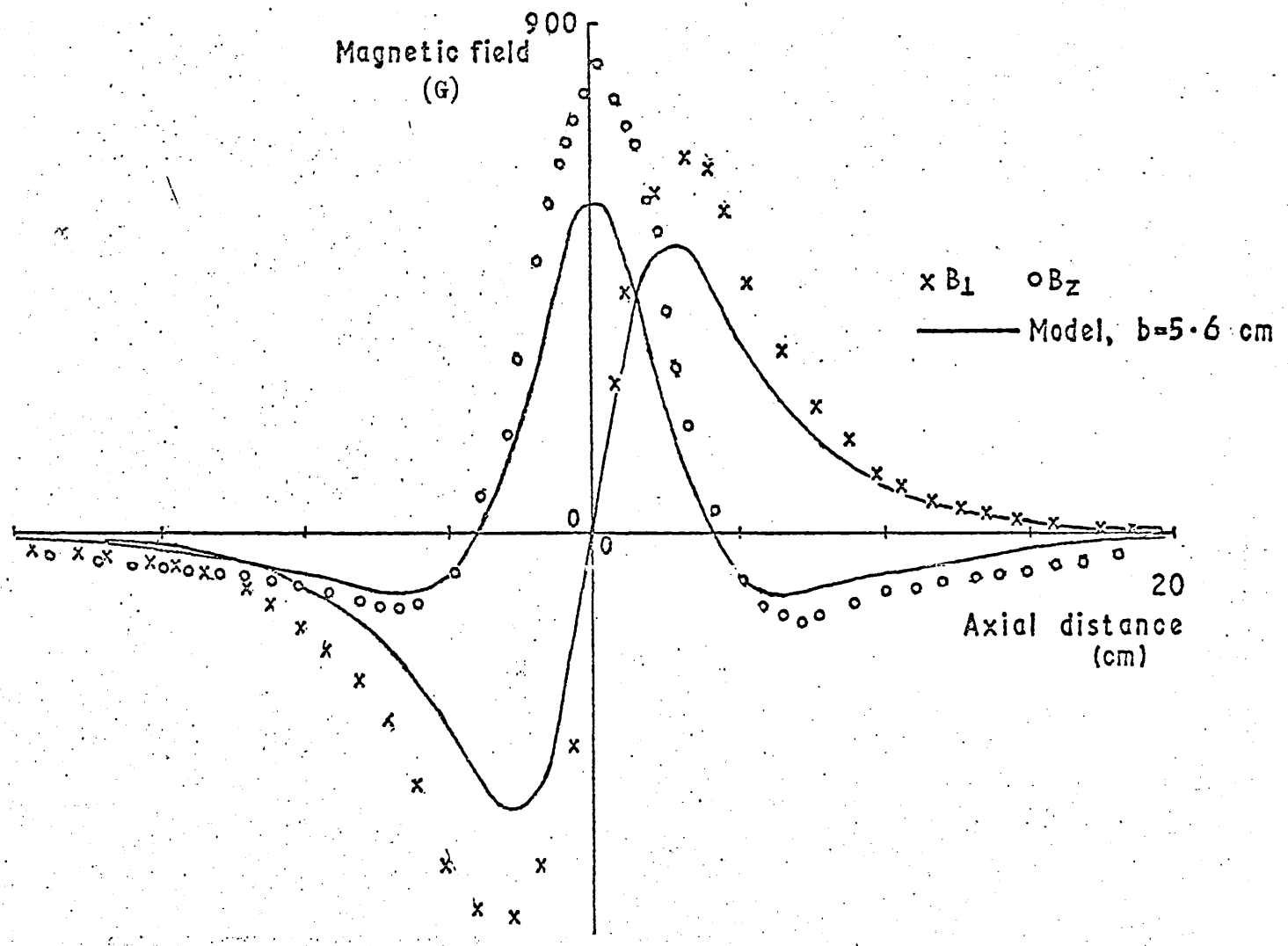

Fig.7.3
The sector coil field components
Sector coil circuit 4 (see Fig.7.2)

Pressure		20 mtorr H_2			10 mtorr H_2		
t(μs)	B_e(kG)	⟨β⟩	T*(eV)	A_p(cm^2)	⟨β⟩	T*(eV)	A_p(cm^2)
0	0		~ 1			~ 1	
1	2.5	0.17	5	16.0	0.2	12	12.5
2	4.8	0.15	7	7.0	0.07	6.5	5.3
3	7.0	0.05	5	6.0	0.03	5.0	4.8
4	9.0	0.02	3.5	5.2	0.015	3.5	4.3
5	10.7	0.01	2	5.2	0.01	0.7	4.2
6	12.0	0.005	2	5.4	0.01	0.4	4.2
9	14.0	0.002	1.4	6.0	0.005	0.4	4.9
Line Mass (gm. cm^{-1})		5.6×10^{-8}			4.3×10^{-8}		
Mass Collection		45%			70%		

* Temperatures obtained from diamagnetism and impurity line radiation history (see Section A2.11).

Fig.7.4

The 2 m theta pinch parameters

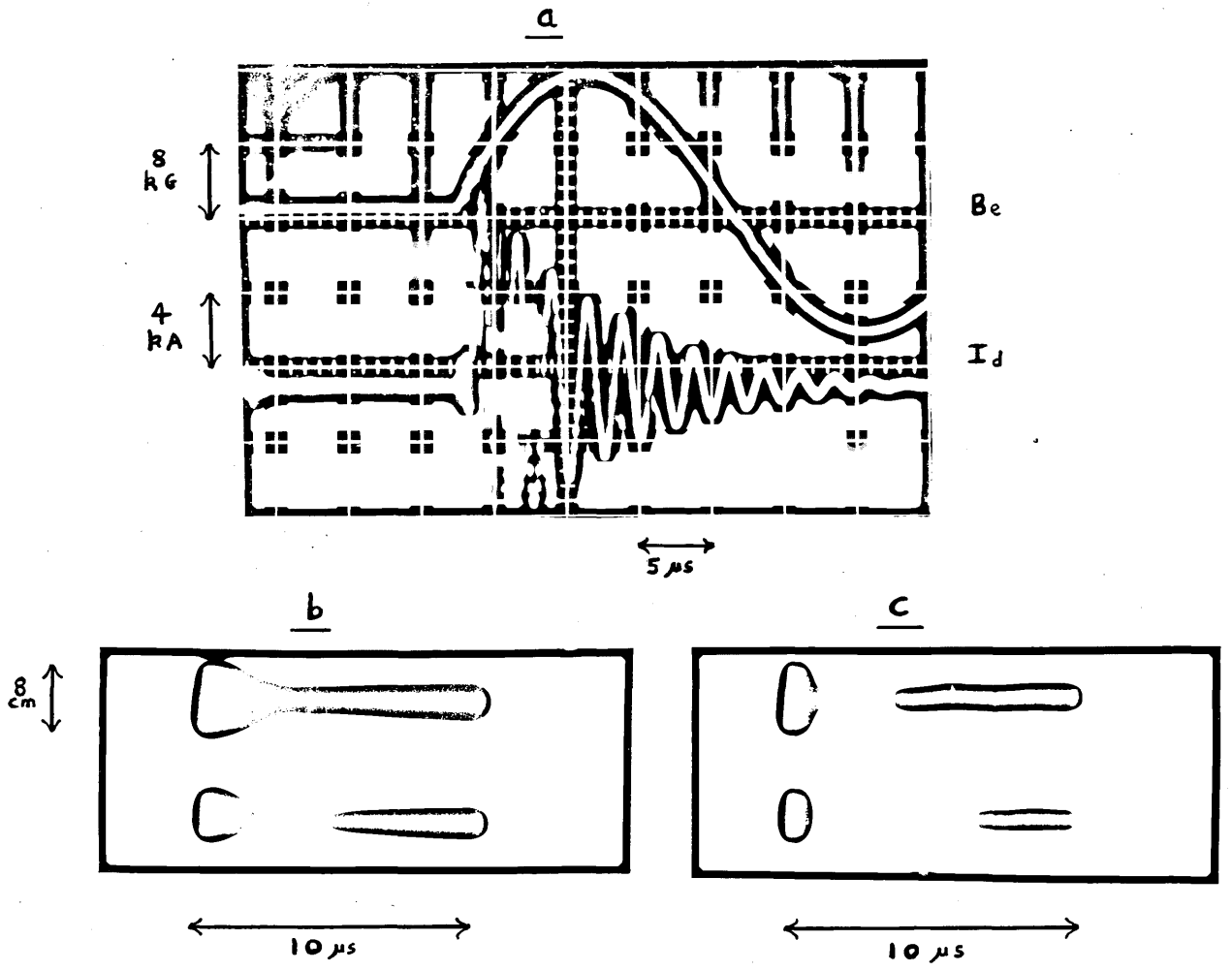

Fig.7.5

(a) External field and sector coil current waveforms
(b) Stereoscopic streak photograph with no sector coil current
(c) Stereoscopic streak photograph with sector coil current

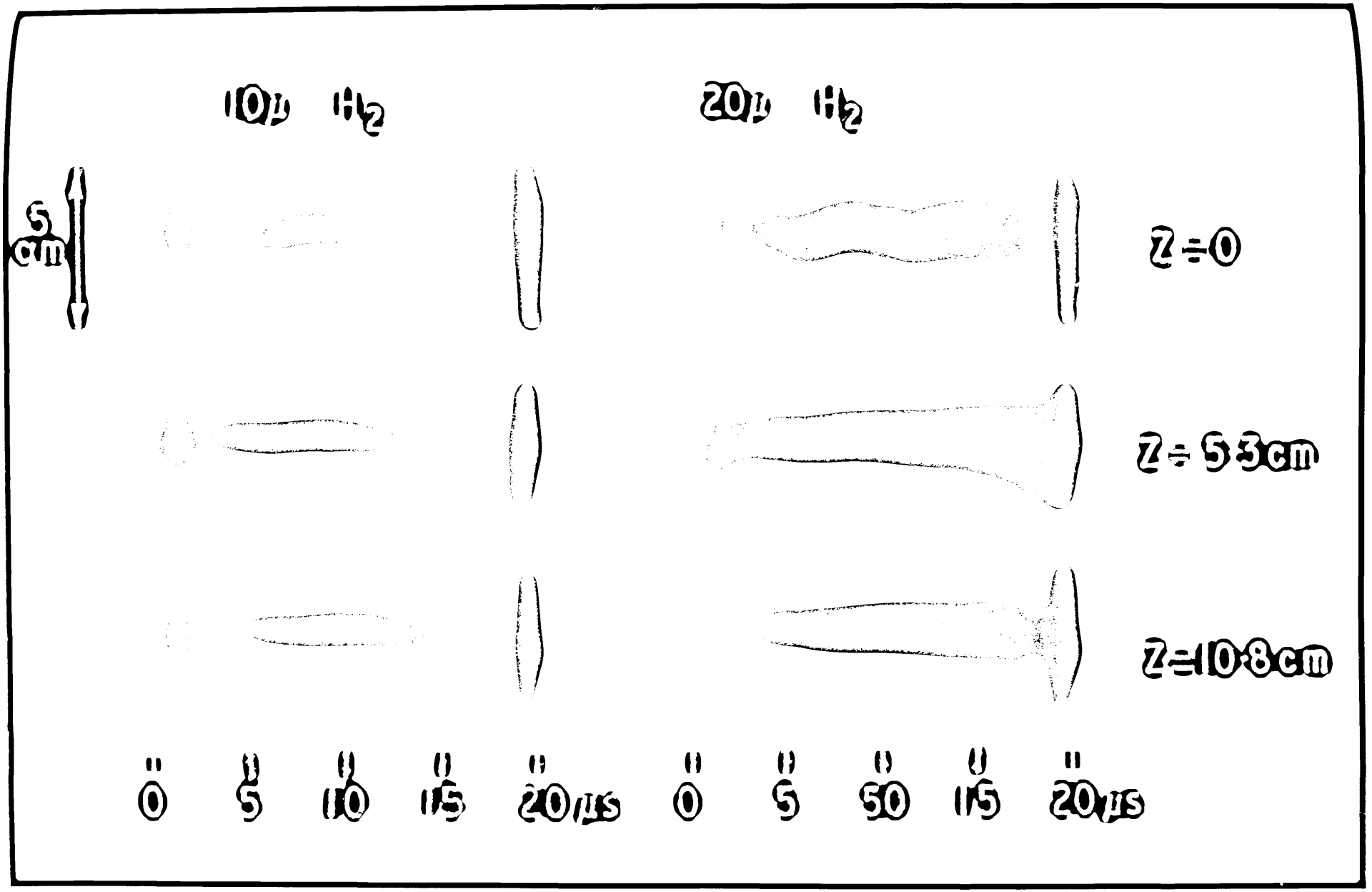

Fig.7.6 Plasma displacement in the 2 m thetatron

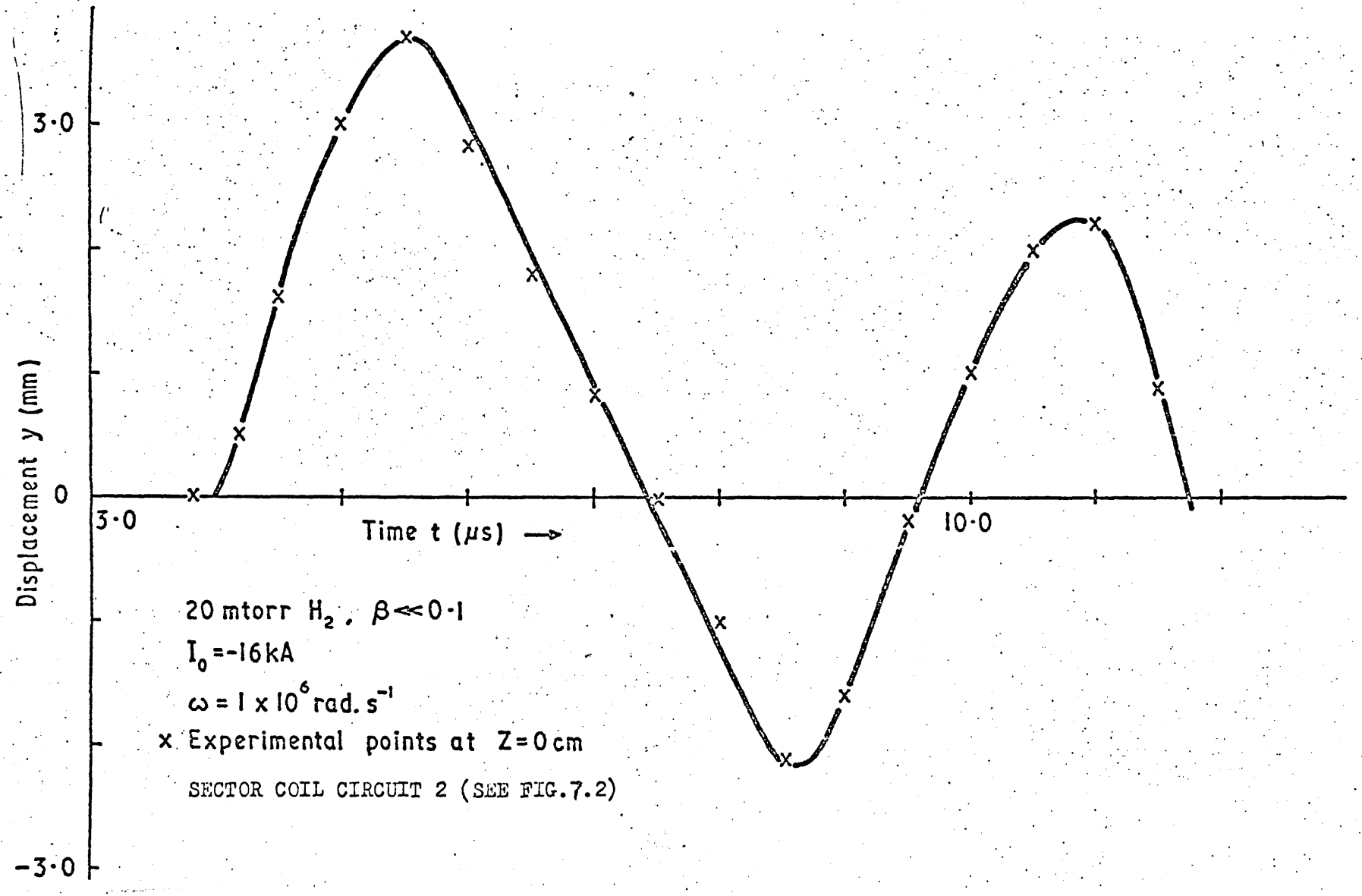

Fig.7.7

The low beta plasma displacement at z = 0 cm

Text Ref. No.	1				2				3				4			
Bank Voltage	45 kV				40 kV				35 kV				45 kV, -350 G bias			
t(μs)	B_e(kG)	⟨β⟩	T(eV)	r_p(cm)	B_e(kG)	⟨β⟩	T(eV)	r_p(cm)	B_e(kG)	⟨β⟩	T(eV)	r_p(cm)	B_e(kG)	⟨β⟩	T(eV)	r_p(cm)
0	0		~1		0		~1		0		~1		0		~1	
2	6.5	0.5	26	1.75	5.8	0.5	30	1.7	5.0	0.5	35	1.7	6.3	0.5	22	2.6
4	12.3	0.42	44	1.25	11.0	0.45	45	1.2	9.6	0.4	66	1.2	12.0	0.48	48	1.8
6	16.0	0.35	53	1.1	14.3	0.33	55	1.1	12.5	0.2	75	1.1	15.5	0.47	55	1.5
8	17.5	0.30	61	1.1	15.6	0.20	60	1.1	13.6	0.1	86	1.1	17.0	0.45	65	1.4
10	17.0	0.27	60	1.2	15.0	0.16	60	1.1	13.0	0.05	85	1.2	16.5	0.43	65	1.6
12	13.3	0.25	45	1.3	11.8	0.13	43	1.3	10.0	0.05	62	1.3	13.0	0.42	50	1.7
Line Mass (gm. cm^{-1})	2.5×10^{-7}				2.0×10^{-7}				9.5×10^{-8}				2.5×10^{-7}			
Mass Collection	68%				55%				26%				68%			

Temperatures obtained from diamagnetism, $T = (T_e + T_i)/2$

Fig.7.8
The 3.5 m theta pinch parameters

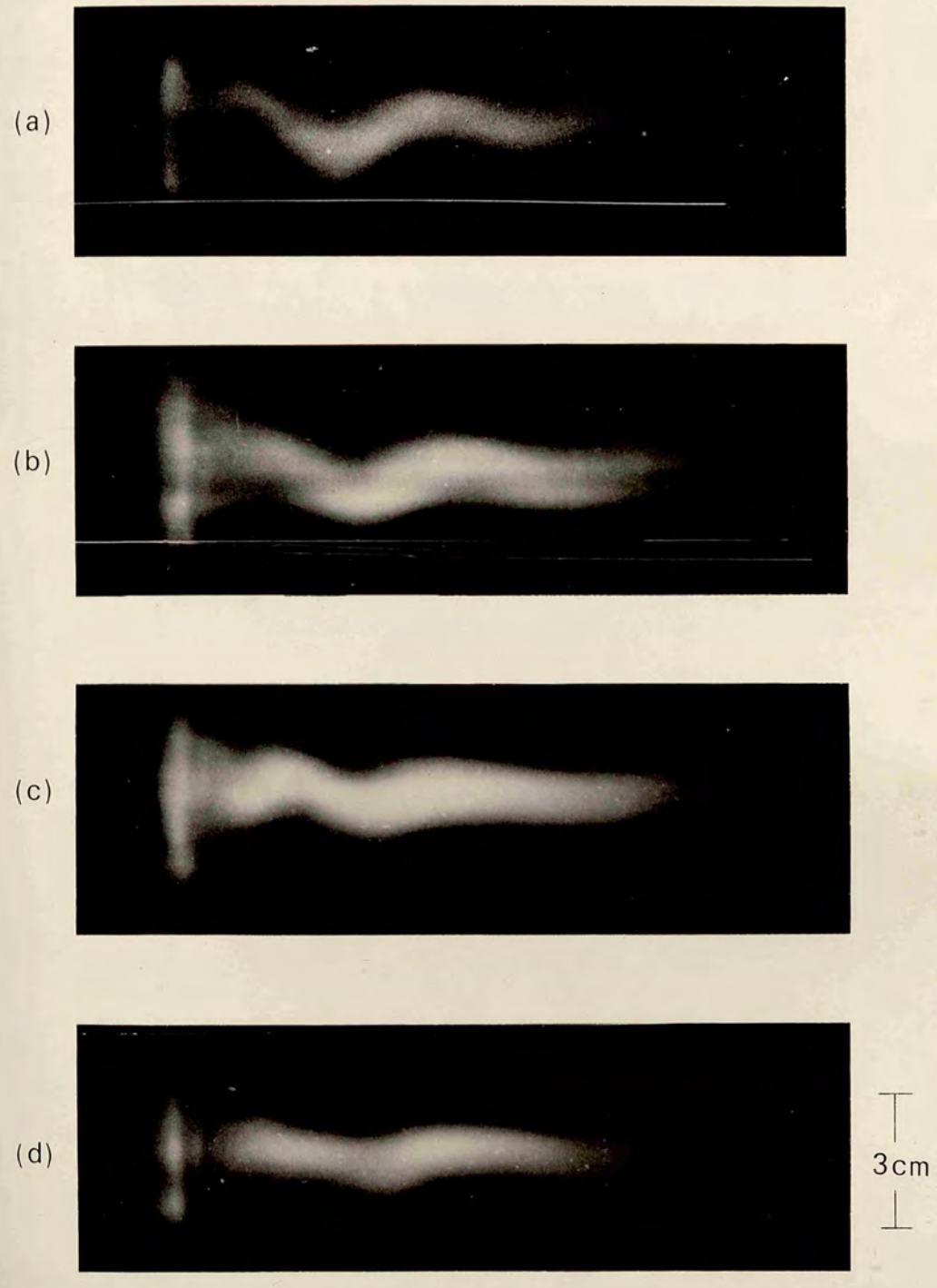

Fig.7.9

Streak photographs of the 3.5 m theta pinch
(a) z = 0 cm ; (b) z = 4 cm ; (c) z = 8 cm ; (d) z = 12 cm

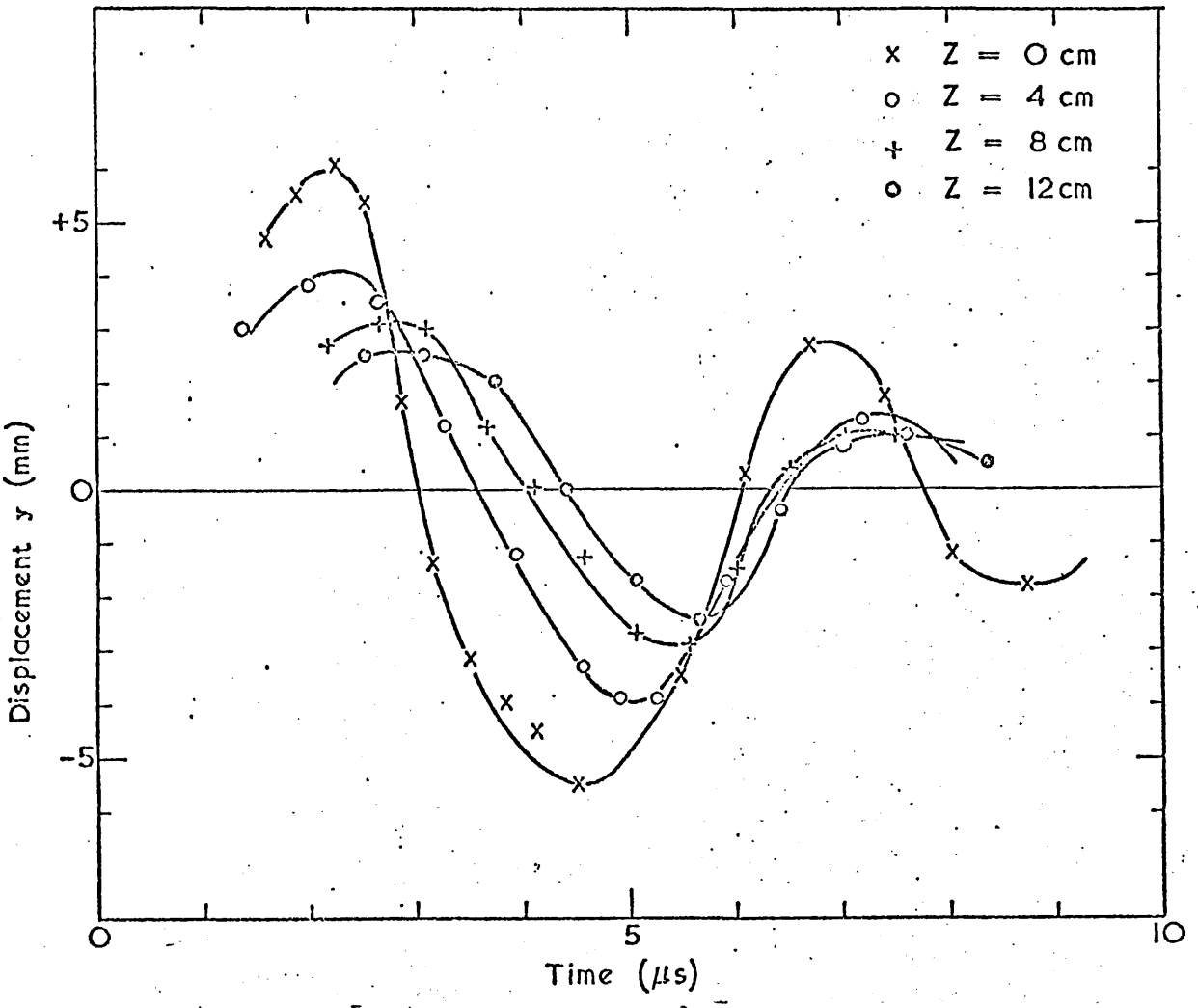

Plasma 1 (see Fig.7.8),
Sector coil circuit 4 (see Fig.7.2),
I_o =- 15.5kA .

Fig.7.10
The high beta plasma displacement

Sector coil circuit 4 ($I_o = 20.6\,kA$, $\omega = 1.35\,rad\,\mu s^{-1}$)

Delay (μs)	Voltage (kV)	45	40	35
1	$\hat{y}$ (cm)	0.8	0.95	1.0
	V(cm. μs^{-1})	16	16	20
4	$\hat{y}$ (cm)	0.5	0.55	0.65
	V(cm. μs^{-1})	23	24	30

Sector coil circuit 3 ($I_o = 10.5\,kA$, $\omega = 2.7\,rad\,\mu s^{-1}$)

Delay (μs)	Voltage (kV)	45	40	35
1	$\hat{y}$ (cm)	0.4	0.45	0.5
	V(cm. μs^{-1})	15	16	22
4	$\hat{y}$ (cm)	0.25	0.3	0.35
	V(cm. μs^{-1})	22	23	28

Delay - the compression to sector coil current delay

Voltage - the main capacitor bank charging voltage

$\hat{y}$ - the first peak displacement at $z = o$ cm

V - the propagation velocity measured over $z = 0$ to $z = 8$ cm

Fig.7.11

The peak displacements and propagation velocities

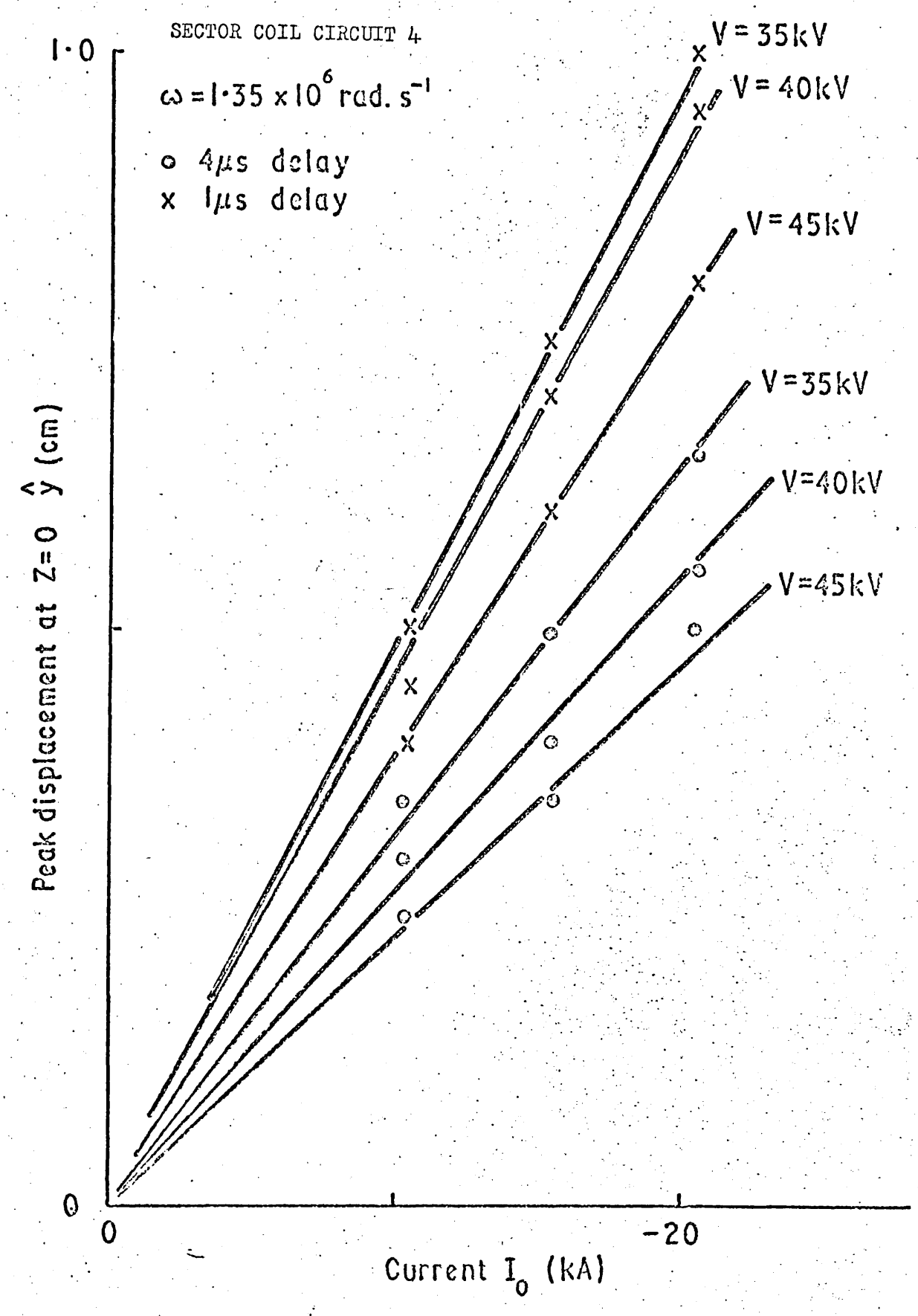

Fig.7.12

Peak displacement against current

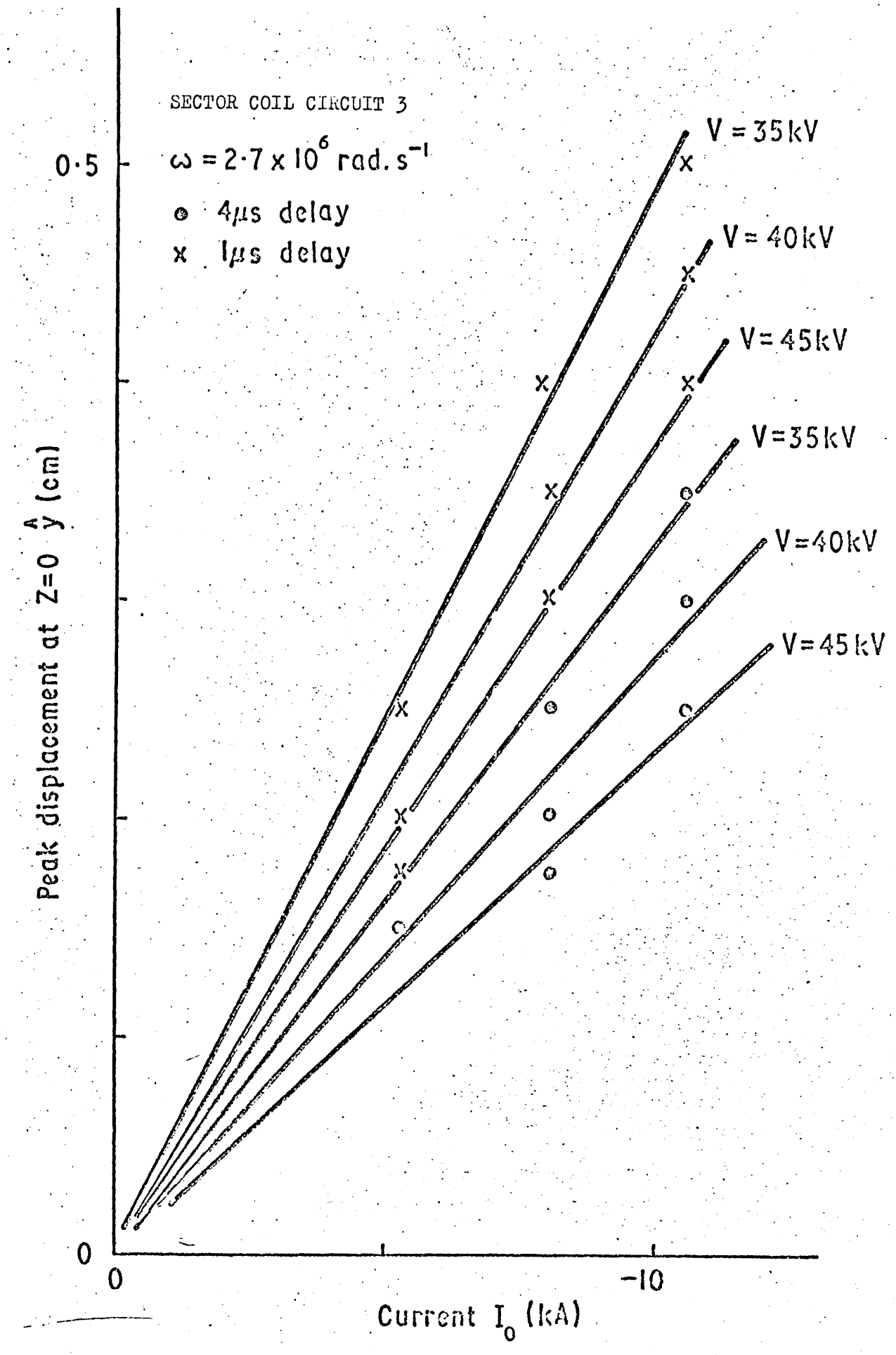

Fig.7.13

Peak displacement against current

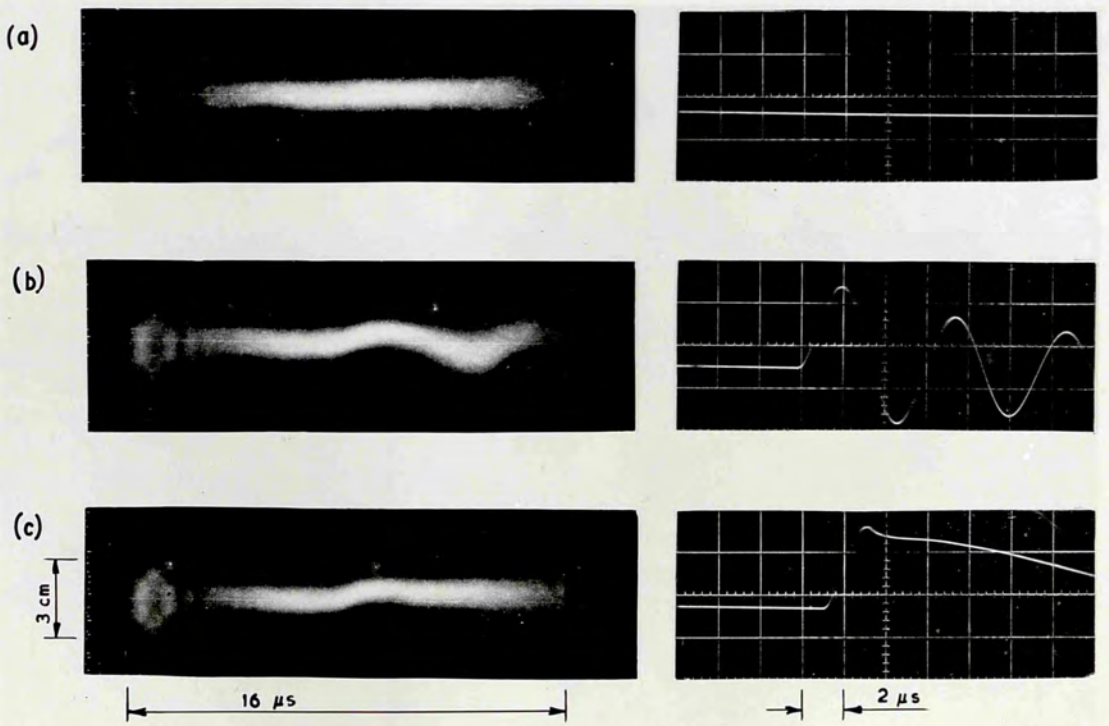

Fig.7.14

Streak photographs with
(a) No sector coil current
(b) A sinusoidal sector coil current
(c) A crowbarred sector coil current

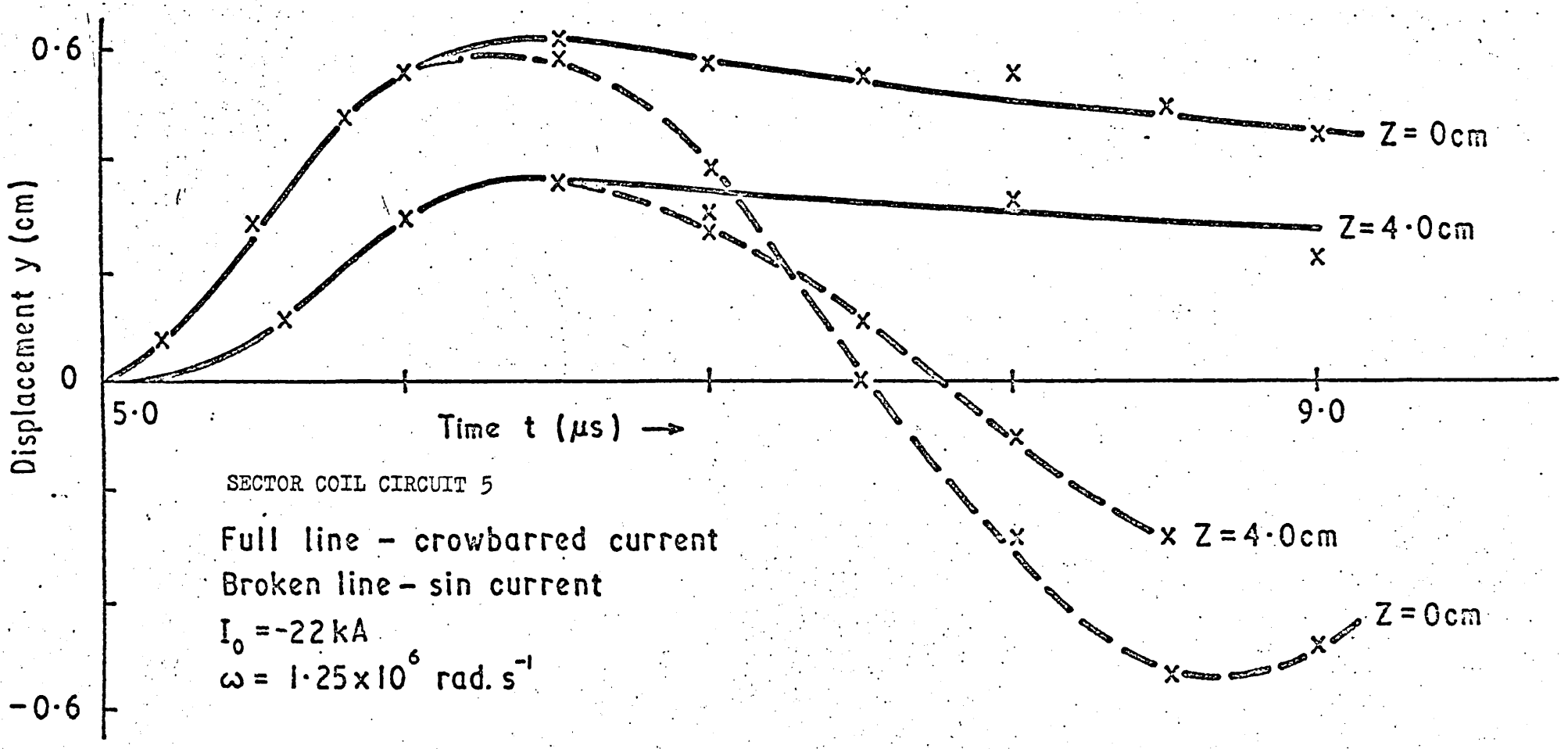

Fig.7.15

Plasma displacements with a sinusoidal and crowbarred sector coil current

Main Bank Charging voltage (kV)		45	40	35
Sector Coil Circuit 4 ($\omega = 1.35\,\text{rad}\,\mu\text{s}^{-1}$)	1 μs Delay	15 cm	20 cm	8 cm
	4 μs Delay	17 cm	15 cm	7 cm
Sector Coil Circuit 3 ($\omega = 2.7\,\text{rad}\,\mu\text{s}^{-1}$	1 μs Delay	13 cm	18 cm	8 cm
	4 μs Delay	15 cm	12 cm	6 cm

Plasma 4 (see Fig.7.8): Sector coil circuit 5 (see Fig.7.2)
ω = 1.25 rad μs , Delay = 5 μs . Damping length = 10 cm.

Delay - The compression to sector coil current delay

Fig.7.16

Damping Lengths

CHAPTER VIII

A DISCUSSION OF THE EXPERIMENTAL RESULTS

8.1 INTRODUCTION

The experimental results reported in Chapter VII are compared with the predictions of the two theories presented in Chapter VI. The assumptions of the equilibrium theory (see Section 6.3) are compared with the experimental conditions; resistivity, viscosity and image currents in the compression coil walls are shown to be important.

Plasma displacements and propagation velocities are explained as forced, m = 1 Alfven waves, as predicted by the equilibrium theory. The spatial damping observed is explained by making an analogy between the experimental waves and Alfven waves[47] in an infinite, dissipative plasma.

The predictions of the mutual inductance theory (see Section 6.5) are shown to disagree with the experimental results; this disagreement is discussed.

8.2 THE ASSUMPTIONS IN THE EQUILIBRIUM THEORY

8.2.1 Introduction

The mathematical assumptions used in the equilibrium theory are justified before applying the theory to explain the experimental results reported in Chapter VII. In deriving the Haas and Wesson equation of motion for a theta pinch (see Section 6.2) the following assumptions were made[33,34]:

(1) The plasma was collision dominated.

(2) Dissipative effects were negligible.

(3) There was a sharp boundary between the plasma and the external magnetic field, with no currents flowing in the plasma body.

(4) The plasma was infinitely long.

(5) Distortion in the (r,θ) plane was negligible.

(6) The conducting walls could be neglected.

When the Haas and Wesson theory was applied to a time varying equilibrium position (see Section 6.3) to derive an equation describing plasma motion (see Section 6.4), the following assumptions were made:

(7) The plasma did not perturb the vacuum fields.

(8) $\left|\frac{\partial \eta}{\partial z}\right|$, $\left|\frac{\partial y}{\partial z}\right|$, and $\left|\frac{\eta}{b}\right| \ll 1$

where $\eta\,(z,t)$ is the equilibrium position

$y\,(z,t)$ is the plasma position

b is the distance between the sector coil axis and the plasma axis.

(9) The magnetic fields produced by the sector coil could be described by the fields of a magnetic dipole.

Each of these assumptions is compared with the experimental conditions. Two test plasmas are used to estimate the experimental plasma parameters, with densities of 10^{16} particles cm^{-3} and temperatures of 10 eV (hydrogen) and 60 eV (deuterium), corresponding to the 2 m (see Fig.7.4) and the 3.5 m theta pinches (see Fig.7.8).

8.2.2 Collisions

The Haas and Wesson analysis[33] is based on the MHD equations for a collisional, fully ionized plasma , where the pressure tensor is isotropic. In the experimental plasma, electron-electron collisions produced a Maxwellian electron velocity distribution and ion-ion collisions a Maxwellian ion velocity distribution; electron-ion collisions then produced an equipartition of energy. For the MHD equations to apply the characteristic experimental time, typically 1 μs , must be greater than the longest self collision time[87] (the ion-ion collision time, t_{ci}).

For the 2 m theta pinch (hydrogen, 10^{16} particles cm^{-3}, 10 eV), $t_{ci} \simeq 5 \times 10^{-9}$ s . For the 3.5 m theta pinch (deuterium, 10^{16} particles cm^{-3}, 60 eV) , $t_{ci} \simeq 1 \times 10^{-7}$ s . Therefore all self collision times were less than the characteristic time.

The characteristic time must also be greater than the equipartition time t_{eq} [88] if the MHD equations are to apply. The longest equipartition time occurs when the electrons are heated, but the ions are cold. For the 2 m theta pinch, $t_{eq} \simeq 1 \times 10^{-7}$ s. For the 3.5 m theta pinch, $t_{eq} \simeq 2 \times 10^{-6}$ s. Therefore the experiments were performed with a characteristic time $t \geqslant t_{eq}$, so that both plasmas were collision dominated.

8.2.3 Dissipation

The MHD equations used by Haas and Wesson do not include resistivity or viscosity. To estimate the relative importance of these two dissipative processes in the experimental plasmas, the Reynolds number R_m [48] and the Prandtl number p_m [48] are calculated for the two test plasmas in a 10 kG field.

The product of the self collision time t_c and the cyclotron frequency ω_c characterises the dissipative coefficient formulae. For the test plasmas

$$\omega_{ci}\, t_{ci}\ (10\ \text{eV}) \simeq 0.5$$
$$\omega_{ce}\, t_{ce}\ (10\ \text{eV}) \simeq 20$$
$$\omega_{ci}\, t_{ci}\ (60\ \text{eV}) \simeq 5$$
$$\omega_{ce}\, t_{ce}\ (60\ \text{eV}) \simeq 270\ .$$

Both plasmas have $\omega_{ci}\, t_{ci} \leqslant 1$ and $\omega_{ce}\, t_{ce} \gg 1$; under these conditions Spitzer's formula for resistivity η [89] and Braginskii's formula for viscosity μ [90] may be used. The Reynolds number and Prandtl number can then be calculated for plasmas with a characteristic velocity $V = 1 \times 10^7$ cm s^{-1} and a characteristic length $L = 5$ cm (typical experimental velocities and lengths), to give

2 m plasma (10 eV)

$\eta_\perp \simeq 3 \times 10^6$ emu
$\mu \simeq 1 \times 10^{-3}$ emu
$\Big\}$ $p_m \simeq 0.2$ $\quad R_m \simeq 1.5 \times 10^2$

3.5 m plasma (60 eV)

$$\left.\begin{array}{l}\eta_\perp \simeq 2\times10^{5} \quad \text{emu} \\ \mu \simeq 1\times10^{-1} \quad \text{emu}\end{array}\right\} p_m \simeq 2.5\times10^{2} \qquad R_m = 2.5\times10^{3} \ .$$

The relative importance of p_m and R_m can be estimated by considering the damping of Alfven waves[47] in an infinite plasma with the same density, temperature, field, characteristic velocity and characteristic length as the test plasma. These waves are spatially damped with an e-folding length Z_D (see Section A.1.3, 'hydromagnetic waves')

$$Z_D = \frac{\mu_o V L^2}{2\pi^2\left(\eta + \frac{\mu_o\mu}{\rho}\right)} = \frac{R_m L}{2\pi^2(1+p_m)} \qquad \ldots (8.2.1)$$

where ρ is the mass density. For the 2 m plasma (10 eV) p_m is small, so that resistivity dominates the damping of Alfven waves, and $Z_D \simeq 30$ cm. For the 3.5 m plasma (60 eV) p_m is large, so that viscosity dominates the damping, and $Z_D \simeq 2.5$ cm. Because the test plasmas represent the experimental plasmas (see Figs. 7.4 and 7.8) it was expected that dissipation would be important. The observed damping of the excited $m = 1$ waves (see Section 7.6) is explained by considering dissipation in Section 8.5.

8.2.4 The Plasma Boundary

The plasma model assumed by Haas and Wesson[33] has a square temperature and density profile, and skin currents (see Section 6.2). Because the experimental plasma had a Gaussian density distribution (see Fig.4.3) an average beta, written $\langle\beta\rangle$, and an average radius, r_p, must be used to compare experimental and theoretical results (see Section A2.10).

End effects were not seen at the plasma midplane for at least 10 μs, so that the plasma could be considered infinitely long (see Section 6.2). Because the perturbing fields produced by the sector coil (see Section 7.4) did not distort the density profiles (see Section 7.6), the assumption that the displacements could be written as $\xi = \xi_{r,\theta}(z)$ (see Section 6.2) was valid.

8.2.5 The Conducting Walls and the Plasma Radius

The equation of motion for a straight theta pinch (equation (6.2.9)) does not include the effect of the restoring forces produced by image currents in the compression coil walls. A parameter α,

$$\alpha = \frac{2 r_p^2}{R_W^2 - r_p^2} \qquad \ldots (8.2.2)$$

where R_W is the conducting wall radius, is used to describe these restoring forces (see equation (6.2.8)). Typical experimental values gave $\alpha \simeq 0.1$; under these conditions the restoring forces are negligible. This was verified by modifying the numerical code to include a finite α (see appendix A.4).

It was assumed that the plasma did not perturb the vacuum fields (see Section 6.3). This was considered valid for the small experimental plasma radii, $\simeq$1 cm.

8.2.6 The Coordinate Systems

The solution of the equation describing the equilibrium position η in the presence of a perturbing field (equation (6.3.12)) required $\eta/b \ll 1$. Typical experimental values gave $\eta/b \simeq 0.1$, so that this assumption was valid.

When the Haas and Wesson theory was applied to the moving equilibrium position (see Section 6.4) it was assumed that the plasma coordinate system and the equilibrium coordinate system were equivalent. This required

$$\left|\frac{\partial y}{\partial z}\right| \text{ and } \left|\frac{\partial \eta}{\partial z}\right| \ll 1$$

where y is the plasma position about the z axis and η is the equilibrium position about the z axis (see Fig.6.1(b)). Typical experimental values gave

$$\left|\frac{\partial y}{\partial z}\right| \simeq 0.2 \text{ and } \left|\frac{\partial \eta}{\partial z}\right| \simeq 0.1 .$$

Therefore the assumptions were valid.

8.2.7 The Sector Coil Magnetic Fields

Both theories presented in Chapter VI assumed that the fields produced by the sector coil could be described by the fields of a magnetic dipole. Fig.7.3 shows that the analytic expressions (see equation (7.4.2) and (7.4.3)) underestimated the fields (see Section 7.4).

The sector coil geometry is illustrated in Fig.8.1(a). By considering image currents produced in the compression coil wall (approximated by a plane surface, as shown in Fig.8.1(b)) the fields on the axis ($x = b$) can be written

$$B_{I(x=b)}(z) = B_{(x=b)}(z) + B_{(x=b+2r_d)}(z) \qquad \ldots (8.2.3)$$

where

$B_{(x=b)}$ is the field produced by a magnetic dipole, radius r_d,

$B_{(x=b+2r_d)}$ is the field produced by the image currents at $x = b + 2r_d$.

Fig.8.2 shows that the experimental fields are described by equation (8.2.3) for the 3.5 m thetatron ($b = 5.6$ cm, $r_d = 1$ cm). The magnetic moment M_I used to calculate the fields predicted by equation (8.2.3) was equated to the experimental moment M by using an equivalent number of turns n_I;

$$n_I = \frac{n A_d}{\pi r_d^2} \qquad \ldots (8.2.4)$$

Therefore

$$M_I = n_I \pi r_d^2 I_d = n A_d I_d = M \qquad \ldots (8.2.5)$$

where I_d is the sector coil current

A_d is the sector coil area

n is the number of sector coil turns

The analysis of Chapter VI required that the fields be described by the fields of a magnetic dipole. Fig.8.3 shows that the experimental fields could be described to within 10% (except for $|z| \simeq 10$ cm) by a magnetic dipole of moment $M^1 = 1.8\,M$, and $b = 6$ cm.

8.3 THE PROPAGATION VELOCITY

The equilibrium theory (Section 6.3) predicted that the fields produced by a sector coil with a sinusoidal current should produce $m=1$ Alfven waves with a propagation velocity (see equation (6.4.3))

$$V_{m=1} = V_A \sqrt{2-\beta} = \frac{B_e}{\left(\frac{\mu_o M}{\pi r_p^2}\right)^{\frac{1}{2}}} \cdot \sqrt{2-\beta} \qquad \ldots (8.3.1)$$

where M is the line mass. Propagation in the high beta plasma was observed and measured (see Section 7.6); the small damping lengths observed in the low beta plasma prohibited accurate measurements (see Section 7.5). The experimental propagation velocity V_{prop} was measured as the velocity of the first peak displacement over 8 cm (see Fig.7.11). $V_{m=1}$ was calculated from measured values of external field B_e, line mass M, plasma radius r_p and average beta $\langle\beta\rangle$ (see Section 8.2.4). Average values were used because the plasma properties were time varying. Fig.8.4 shows that

$$V_{prop} = V_{m=1}, \text{ with a probable error of } 0.1 \qquad \ldots (8.3.2)$$

8.4 THE PLASMA DISPLACEMENT

The equilibrium theory predicted the normalised peak plasma displacement in the plane of a current loop, $\hat{y}_n$, as a function of the normalised velocity V_n (see Fig.6.4). For real displacements produced by a sinusoidal current of amplitude I_o and frequency ω (see equation (6.4.6)):

$$\hat{y} = k\, \hat{y}_n(V_n) \qquad \ldots (8.4.1)$$

where (see equation (6.3.17)):

$$k = \frac{2\,\mu_o\, M}{4\pi b^2 B_e} \qquad \ldots (8.4.2)$$

and M, the magnetic dipole moment, is given by

$$M = n A_d I_o \qquad \ldots (8.4.3)$$

where A_d is the current loop area. It was shown in Section 8.2.7 that the moment M should be replaced by M^1, where

$$M^1 = 1.8\,M_{(b = 6\ cm)} \qquad \ldots (8.4.4)$$

Therefore equation (8.4.1) becomes

$$\hat{y} = K\,I_o \qquad \ldots (8.4.5)$$

with

$$K = \frac{0.9\,\mu_o\,n\,A_d\,\hat{y}_n(V_n)}{b^2\,B_e} \qquad \ldots (8.4.6)$$

with $b = 6$ cm, and $V_n = V_{m=1}/\omega b$.

Figures 7.12 and 7.13 show that the experimental peak displacement $\hat{y}$ was proportional to the sector coil current I_o for constant sector coil current delay and frequency, and constant main capacitor bank charging voltage. Values of K_{exp} obtained from Figs.7.12 and 7.13 were compared with values of K_{theory}. derived from equation (8.4.6), using time averaged values of B_e, A_d and $V_{m=1}$. The results, shown in Fig.8.5, show that

$$K_{theory} = 1.2\,K_{exp}, \qquad \ldots (8.4.7)$$

with a probable error of 0.1 .

Therefore the theoretical predictions overestimated the experimental results by about 20%. This discrepancy could be due to the time averaging, or the analytic approximation to the sector coil fields (see Section 8.2.7, and equation (8,4.4)).

To remove the errors introduced by the averaging process, the displacements produced with plasma 4 (see Fig.7.8) were considered (see Fig.7.15). For this plasma the measured parameters were constant to within 20% from 4 μs to 12 μs after the implosion, except for the external field B_e. The numerical code was used, with a sinusoidally varying B_e and plasma parameters measured at 7 μs (see Fig.7.8), to predict the motion produced by a sinusoidal and crowbarred sector coil current. The predictions, compared with the experimental results (see Fig.7.15) in Fig.8.6, show that theory and experiment agree to within the experimental errors ($y \pm 0.05$ cm, $t \pm 0.3$ μs) . Therefore the overestimation of the constant K (see equation (8.4.6)) in Fig.8.5 was accredited to the averaging process used.

Propagation velocities could not be measured in the low beta plasma because of the small damping lengths (see Section 7.5). Theoretical values of $V_{m=1} \geq 40\,\text{cm}\,\mu\text{s}^{-1}$ were derived (see equation (8.3.1)), corresponding to normalised velocities $V_n \geq 4$; therefore normalised peak displacements $\hat{y}_n \simeq -1$ were expected (see Fig.6.4). Peak displacements $\simeq 1.1$ cm were predicted whereas experimental displacements were $\simeq 0.4$ cm. This discrepancy is discussed in Section 8.5.

8.5 THE DAMPING

Damping lengths between 5 cm and 20 cms were measured (see Fig.7.16). These are explained by making an analogy between the excited waves and Alfven waves in an infinite, dissipative plasma. For small damping, the e-folding length is given by equation (8.2.1)

$$Z_D = \frac{\mu_o V \lambda^2}{2\pi^2 \eta \left(1 + \frac{\mu_o \mu}{\rho \eta}\right)} \qquad \ldots (8.5.1)$$

where λ is the plasma wavelength.

The values of Z_D calculated from equation (8.5.1) are compared with the measured damping lengths in Fig.8.7. Time averaged plasma parameters were used to derive values of resistivity η and viscosity μ (see Section 8.2.3). The velocity V was calculated as $V_{m=1}$. The wavelength λ was taken as the characteristic axial length of 5 cm (see Section 7.4), because computations showed that for early times the spatial dependence of the plasma position was determined by the characteristic length of the perturbing fields (see Section 6.4.2, and Fig.6.7). If the wavelength was inversely proportional to the sector coil frequency ω, Z_D would be proportional to $1/\omega^2$. This was not observed.

The values of damping length Z_D(theory) derived from equation (8.5.1) for the high beta plasma were dominated by viscosity, and were in order of magnitude agreement with the experimental results. Reducing the main capacitor bank voltage decreased the mass collection and therefore the

density (see Fig.4.9), so the damping lengths were decreased. For the low beta plasma resistivity dominated the value of Z_D (theory); again the theoretical and experimental values were in order of magnitude agreement.

Although equation (8.5.1) is valid only for Alfven waves in an infinite medium with $Z_D/\lambda \ll 1$, a comparison of the experimental and theoretical damp-lengths shows that there is order of magnitude agreement. Finite resistivity can then explain the damping at low temperatures (10 eV), and finite viscosity the damping at high temperatures (50 eV). The reduced peak displacements observed in the low temperature plasma (see Section 8.4) are consistent with the very small damping lengths measured.

8.6 THE PREDICTIONS OF THE MUTUAL INDUCTANCE THEORY

The mutual inductance theory (see Section 6.5) was based on a calculation of the $\bar{j}\times\bar{B}$ forces over the plasma volume; for a plasma with $\beta \ll 1$ displacements $\simeq 0$ were predicted. Fig.7.7 shows that displacements $\simeq 0.4$ cm were observed in the low beta plasma (see Fig.7.4); the mutual inductance theory predicted displacements $\simeq 5\times10^{-3}$ cm. An expression for the ratio of the two theoretical force terms can be written (see equation (6.6.3))

$$\frac{F\ (\text{equilibrium})}{F^1(\text{mutual inductance})} = \frac{2(2-\beta)}{(1-\sqrt{1-\beta})} \qquad \ldots (8.6.1)$$

For a high beta plasma, where $\beta = \langle\beta\rangle = 0.5$, this ratio is 10. Therefore the mutual inductance theory predicted displacements at least an order of magnitude smaller than the equilibrium theory. Because the equilibrium theory predicted the experimental results to within 20% (see Section 8.4) the mutual inductance theory was inaccurate.

A complete calculation of the $\bar{j}\times\bar{B}$ forces (see equation (6.5.1)) would result in a displacement proportional to the square of the sector coil current for a low beta plasma, because the diamagnetic current I_d

approaches zero for $\beta \ll 1$. The observed displacements were linearly dependent on I_d. Therefore the model described in Section 6.5 cannot apply to the experiments. The displacement of the plasma equilibrium (see Section 6.3) must then dominate the displacement produced by the $\bar{j} \times \bar{B}$ forces.

8.7 SUMMARY

The predictions of the equilibrium theory (see Section 6.3) were compared with the experimental results (see Chapter VII). Each of the assumptions used to derive the equilibrium theory was considered; dissipation and image currents were shown to be important. The sector coil fields could be approximated to the fields produced by a magnetic dipole (as assumed in the theory) if an equivalent dipole moment was used to simulate the effect of image currents.

Propagation velocities measured in the 3.5 m long, high beta plasma were consistent with the predicted propagation velocity $V_A\sqrt{2-\beta}$. Peak plasma displacements, predicted for a sinusoidal sector coil current, were 20% larger than the observed displacements. This discrepancy was accredited to the time averaging procedure used; for constant plasma parameters the theoretical predictions were within the experimental errors. Therefore the peak plasma displacements were proportional to the sector coil current, and inversely proportional to the external axial magnetic field.

Displacements measured on the 2 m long, low beta plasma were 25% of those predicted. The waves were damped with an e-folding length of 5 cm; with this damping it was expected that the peak amplitude would be reduced.

The damping of the waves in both the high and low beta plasmas was accredited to dissipative effects, which were neglected in the theory. An analogy between the experimental waves and Alfven waves in an infinite, dissipative plasma was made. Using a wavelength determined by the spatial distribution of the force, the damping was explained as resistive in the

low temperature (10 eV), low beta plasma and viscous in the high temperature (50 eV), high beta plasma.

The predictions of the mutual inductance theory (see Section 6.5) were shown to underestimate the plasma displacements by at least a factor 10. This showed the importance of considering the effect of the perturbing fields on the plasma equilibrium position.

(a)

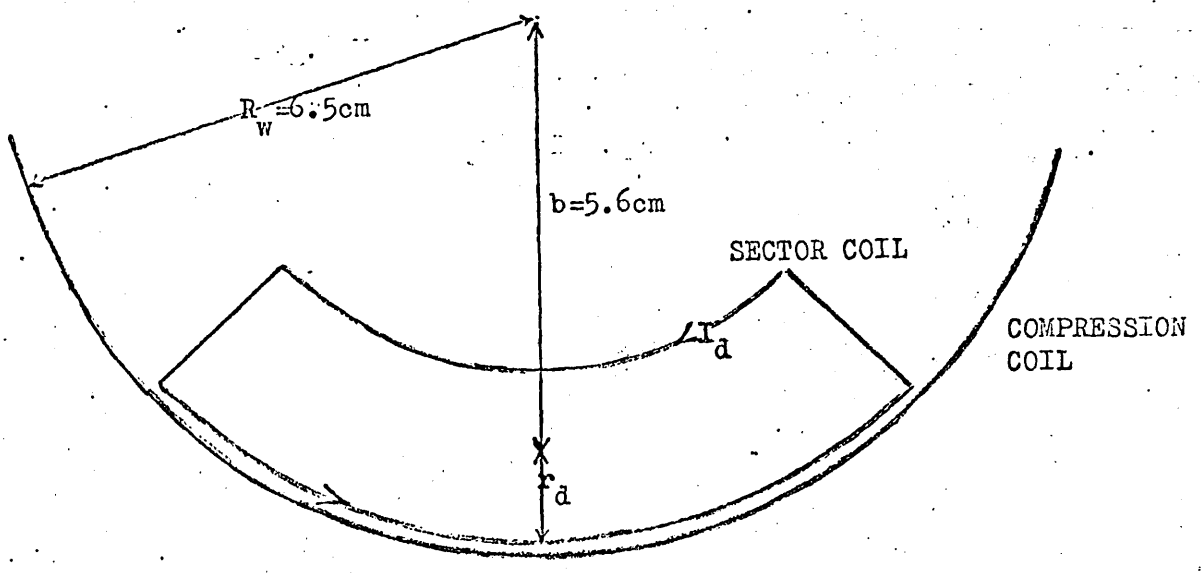

MAGNETIC DIPOLE MOMENT $M = n A_d I_d$

WHERE A_d = SECTOR COIL AREA

n = NUMBER OF TURNS

(b)

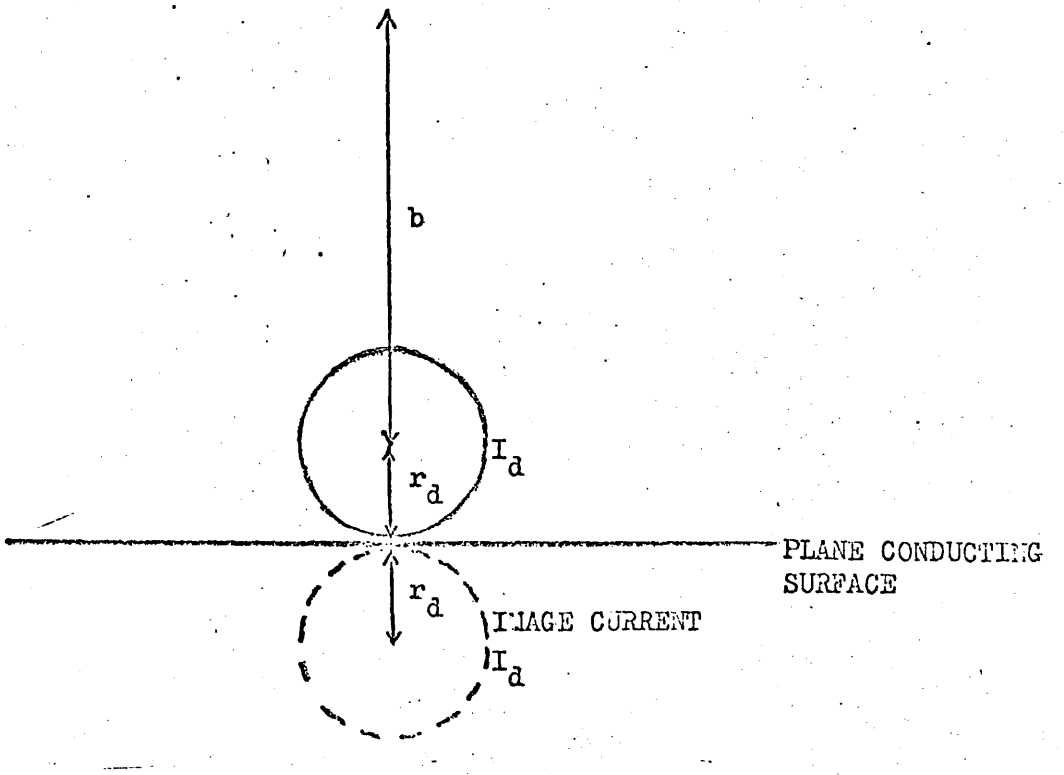

MAGNETIC DIPOLE MOMENT $M_I = n_I(\pi r_d^2)\ I_d$

WHERE $n_I = A_d/(\pi r_d^2)$

Fig.8.1

(a) The sector coil geometry; (b) The image currents

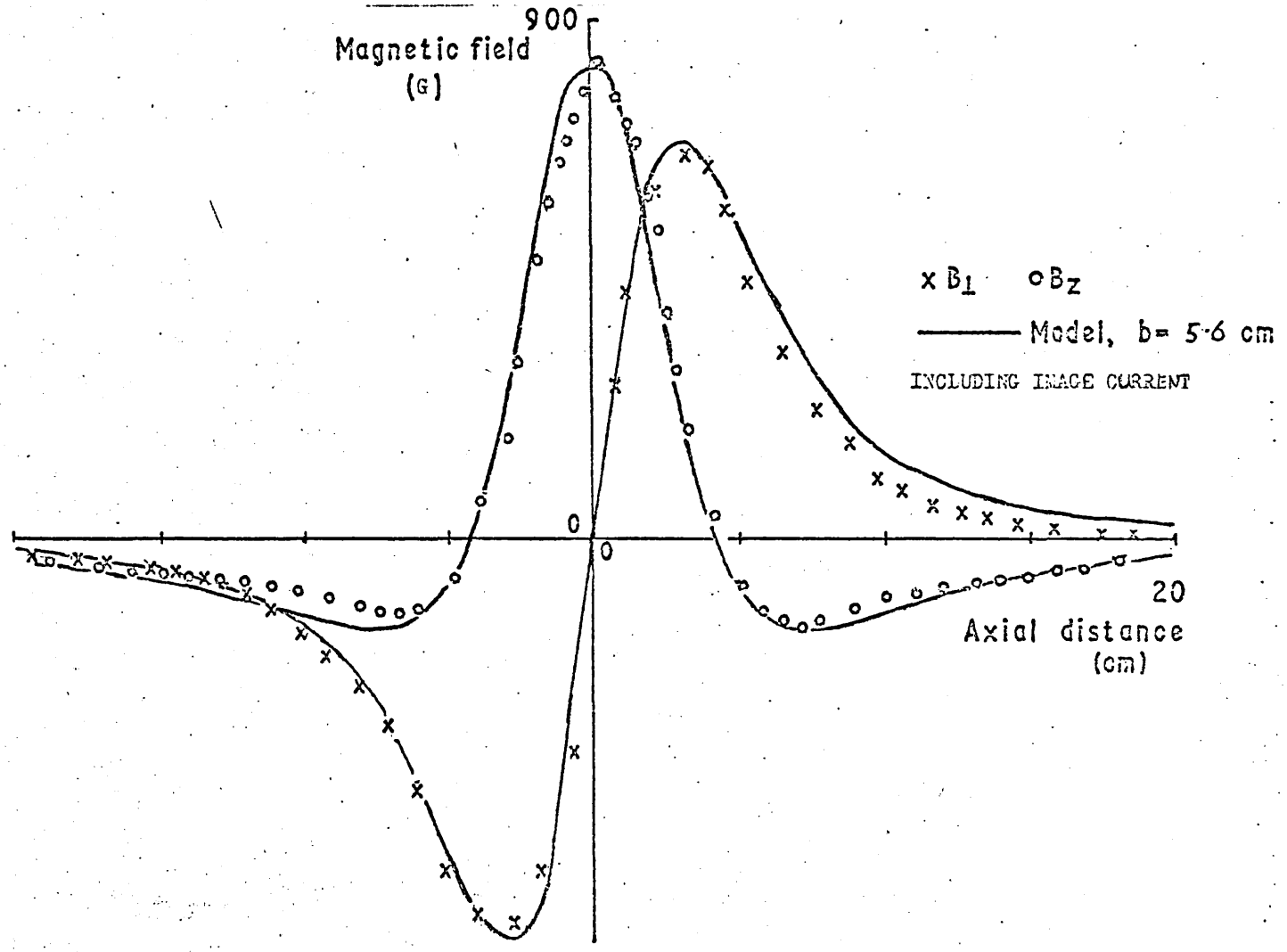

Fig.8.2
The sector coil magnetic field components,
including image currents

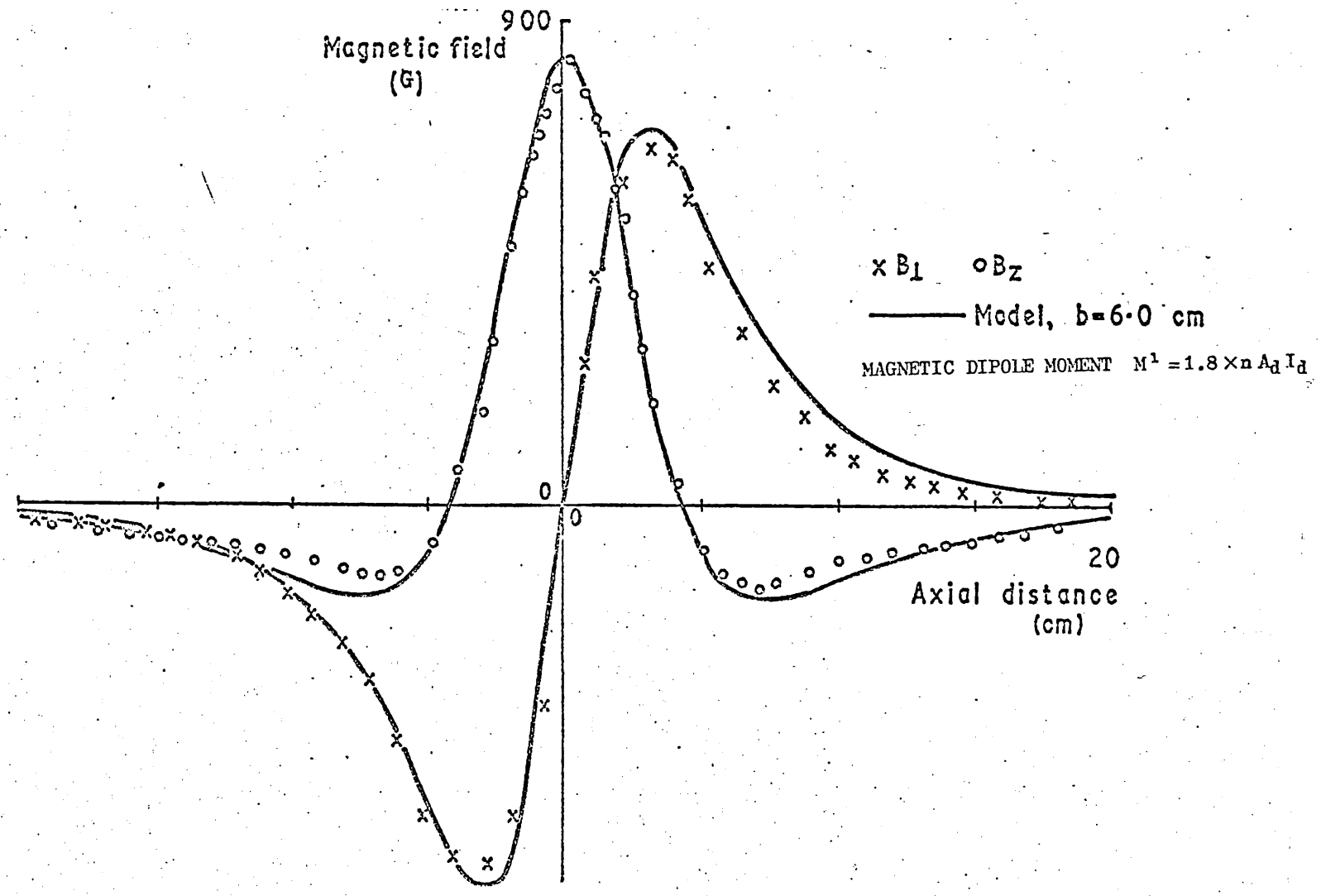

Fig.8.3
The sector coil magnetic field components, with an equivalent dipole moment to simulate the image currents

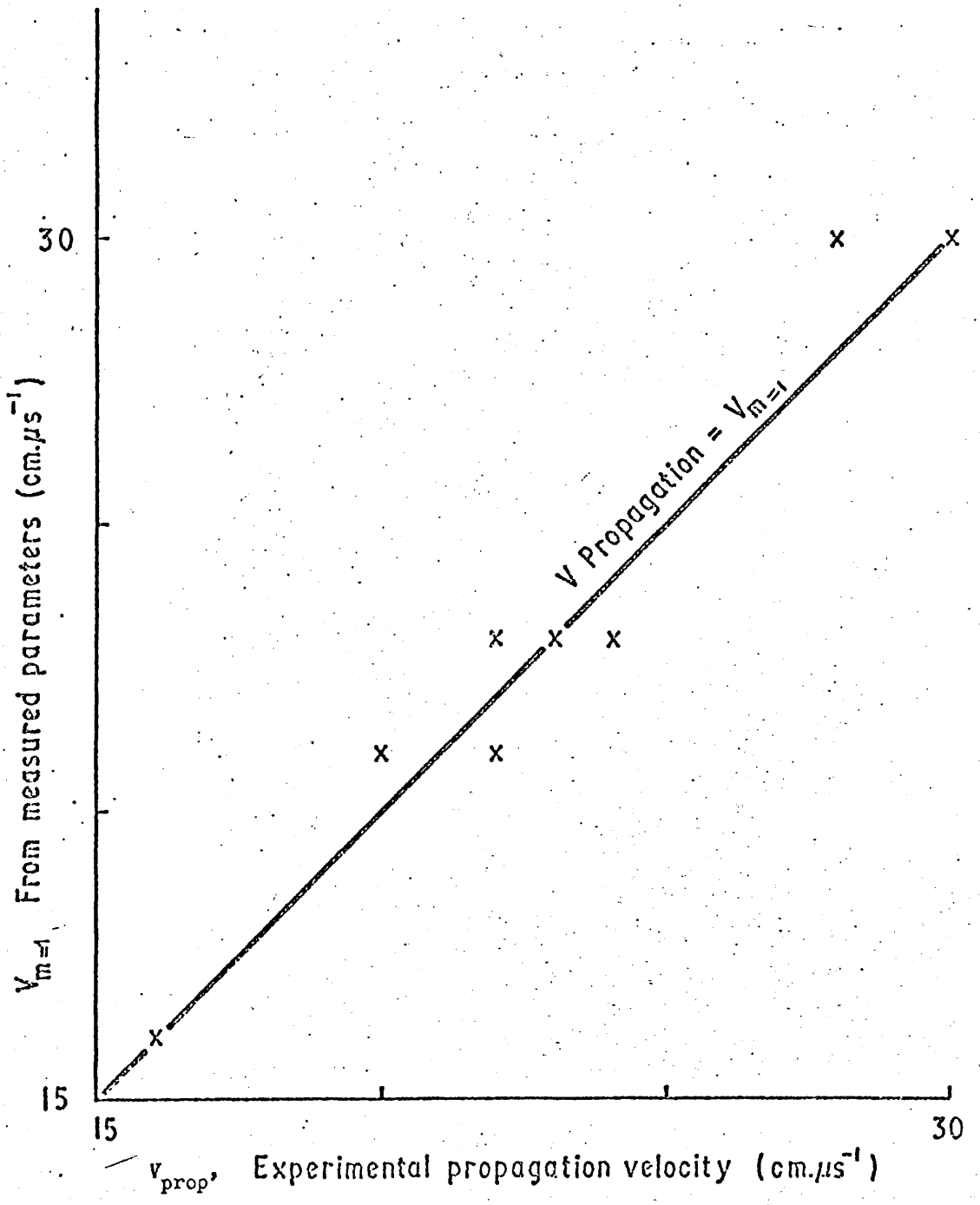

Fig.8.4
The experimental (V_{prop}) and theoretical ($V_{m=1}$) propagation velocities

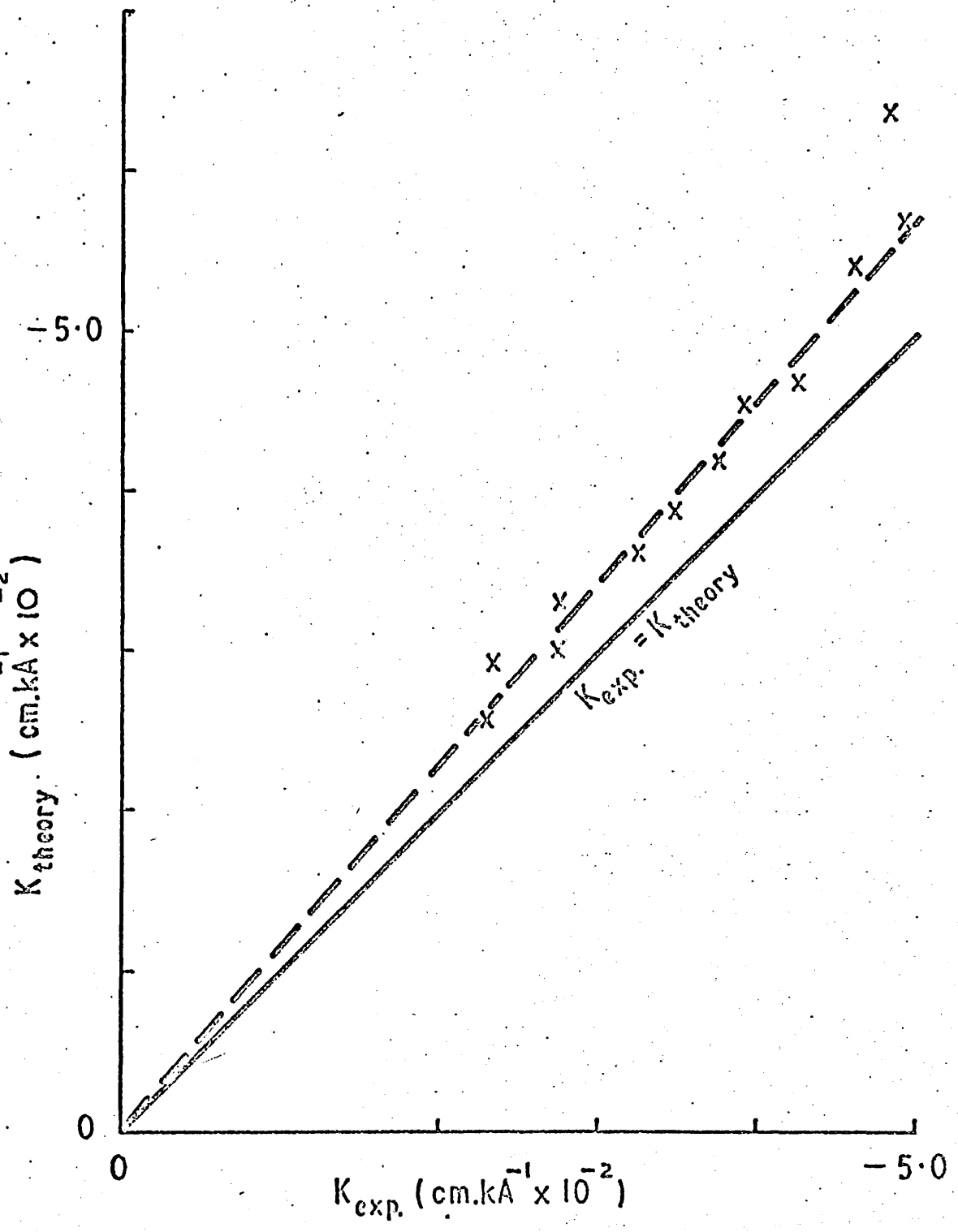

Fig.8.5

The experimental (K_{exp}) and theoretical (K_{theory}) displacement constants

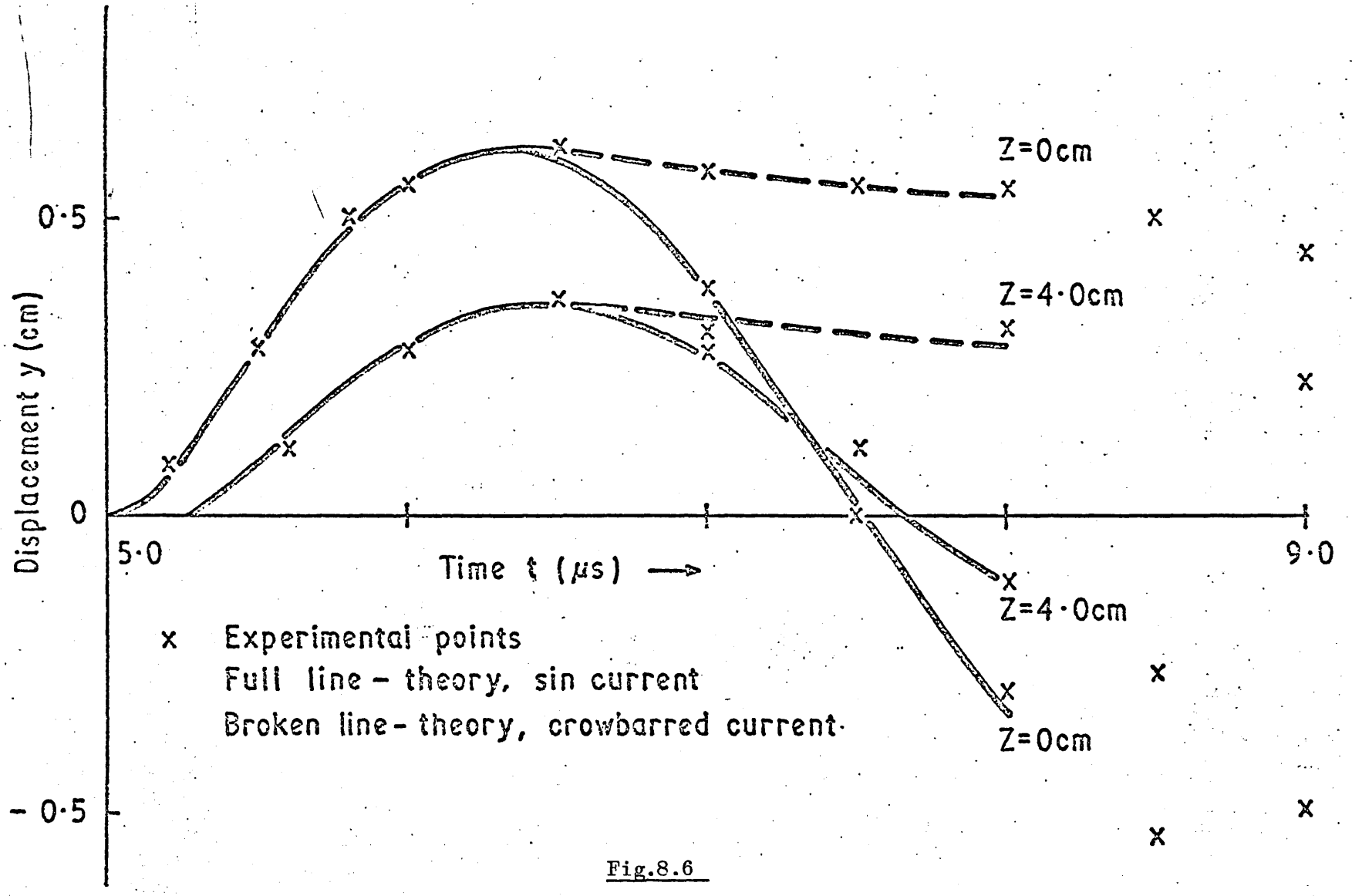

Fig.8.6

The experimental and theoretical plasma displacements with a sinusoidal and crowbarred sector coil current

(a) The 3.5 m theta pinch

Main Capacitor Bank Charging Voltage (kV)			45	40	35
ω = 1.35 rad μs^{-1}	1 μs delay	Z_D (exp) (cm)	15	20	8
		Z_D(theory) (cm)	21	29	5
	4 μs delay	Z_D(exp) (cm)	17	15	7
		Z_D(theory) (cm)	23	18	4
ω = 2.7 rad μs^{-1}	1 μs delay	Z_D(exp) (cm)	13	18	8
		Z_D(theory) (cm)	21	29	5
	4 μs delay	Z_D(exp) (cm)	15	12	6
		Z_D(theory) (cm)	23	18	4

ω = 1.25 rad μs^{-1}	Main Capacitor Bank Charging Voltage = 45 kV - 350 G bias field (Plasma 4, Fig.7.8)	5 μs delay	Z (exp) = 10 cm Z(theory) = 13 cm

(b) The 2 m theta pinch

Filling Pressure (mtorr H_2)			10	20
ω = 1.1 and 2.2 rad μs^{-1}	1 μs delay	Z (exp) (cm)	~ 5	~ 5
		Z(theory) (cm)	45	40
	4 μs delay	Z (exp) (cm)	~ 5	~ 5
		Z(theory) (cm)	2	20

Z_D(theory) is the damping length of Alfven waves in an infinite plasma with the same magnetic field, density and beta as the experimental plasma.

ω is the frequency of the sector coil current. The delay is between the compression current and the sector coil current.

Fig.8.7
Experimental and theoretical damping lengths

CHAPTER IX

A FEEDBACK STABILIZATION SYSTEM FOR A THETA PINCH

9.1 INTRODUCTION

In this chapter the application of the results obtained and the principles discussed in previous chapters to the problem of feedback stabilization of gross MHD instabilities is considered. A review of the limited experimental work is presented. It is then shown that a small, current carrying coil outside a straight theta pinch can be used to produce a restoring force on an unstable plasma. A feedback control system is designed, using this restoring force and an existing power amplifier[98] and optical sensing system. Nyquist's criterion[91] is applied to the control system to determine its stable operating conditions.

9.2 A REVIEW OF FEEDBACK CONTROL EXPERIMENTS AND THEORY FOR HIGH BETA PLASMAS

The suppression of plasma instabilities using feedback control was first suggested by Morozov and Solevev in 1965[92]; since then most experiments have been concerned with low beta plasmas[84]. Experiments with gross modes in high beta plasmas are limited to the Scylla[85] and Scyllac[86] theta pinches.

The straight Scylla IV-3 theta pinch[85] has been used to determine the effect on the plasma motion of perturbing fields whose scalar potentials are of the form

$$\chi_\ell = \frac{B_o}{h}\left[C_\ell I_\ell(hr) + D_\ell K_\ell(hr)\right] \sin(\ell\theta - hz) \qquad \ldots (9.2.1)$$

where

B_o is the longitudinal field,
h is the field wave number, $= 2\pi/\lambda$,
C_ℓ, I_ℓ, D_ℓ and K_ℓ are Bessel functions,
r is the radial coordinate,
θ is the azimuthal coordinate,
$2\pi\ell/h$ is the field pitch.

Applying an $\ell = 1$ helical field, produced by currents in external helical windings, caused the plasma to assume a helical equilibrium position

$$r = a\left[1 + \delta_1 \cos(\theta - hz)\right] , \qquad \ldots (9.2.2)$$

where δ_1 is the helical shift of the plasma column, and a is the plasma radius. The plasma was then unstable to $m=1$, $k \simeq 0$ modes; a destabilizing force F_1 per unit length can be written

$$F_1 = \pi a^2 \rho \gamma_1 \xi , \qquad \ldots (9.2.3)$$

where ρ is the density, ξ is the $m=1$ displacement, and γ_1 is the $m=1$ growth rate.

An $\ell = 0$ (bumpy) field was then applied, which, together with the $\ell = 1$ field, produced a restoring force

$$F_{1,0} = \frac{\beta}{B} (3-2\beta) B_o^2 h^2 a^3 \delta_1 \delta_o \qquad \ldots (9.2.4)$$

where δ_o is the $m=0$ displacement. Experiments showed that the force $F_{1,0}$ could be used to control the plasma position[83]. A feedback control system has been built to stabilize the $m=1$ mode produced by the $\ell = 1$ fields[85]. Twenty 15 MW amplifiers will be used to stabilize one direction only, two amplifiers driving a pair of $\ell = 0$ coils.

An equilibrium plasma configuration does not exist in a simple toroidal theta pinch because of the transverse pressure gradient of the longitudinal field. An equilibrium is possible if helical fields with scalar potentials given by equation (9.2.1) are added[93]. The force $F_{1,0}$ (see equation (9.2.4)), produced by a combination of $\ell = 0$ and $\ell = 1$ fields, has been used to provide toroidal equilibrium in the Scyllac device[86]. It is proposed to utilise the same force to control $m=1$ modes, using about two hundred 15 MW amplifiers.

In contrast to the theory presented in Chapter VI, the MHD model used to derive the force $F_{1,0}$ does not consider propagation. This is valid because the force $F_{1,0}$ is not spatially dependent.

9.3 THE RESTORING FORCES PRODUCED BY EXTERNAL CURRENT CARRYING COILS ON AN m = 1 UNSTABLE THETA PINCH

The experiments reported in Chapter VII showed that a straight theta pinch could be bodily moved by passing current around a sector coil. A theory presented in Chapter VI predicted the plasma displacement and propagation velocity by considering the effect of the perturbing field produced by the sector coil on the plasma equilibrium position. This theory is extended to derive the restoring force produced by a sector coil on an m = 1 unstable plasma.

A theta pinch produced with an additional $\ell = 0$ field is unstable to long wavelength, m = 1 modes (see Section 2.8.4)[34]. An equation of plasma motion can be written (see equation (6.2.8))

$$\ddot{\xi} = A\xi'' + B\xi' + C\xi \qquad \ldots (9.3.1)$$

where A, B and C are functions of B_z, R, β and ρ,

B_z is the axial field,

R(z) is the plasma radius,

ρ is the density.

Equation (9.3.1) describes the plasma motion in an inertial frame of reference. Modifying the equation to describe the motion in a non inertial frame (see equation (6.2.12)) gives

$$\ddot{\xi} = A\xi'' + B\xi' + C\xi - \ddot{\eta} \qquad \ldots (9.3.2)$$

where $\ddot{\eta}$ is the acceleration of the frame of reference. If η describes the unstable equilibrium position, and ξ the plasma displacement about the equilibrium, the plasma displacement y about the z axis is (see equation (6.4.2) and Fig.6.1(b))

$$y = \eta + \xi . \qquad \ldots (9.3.3)$$

Substituting for ξ from equation (9.3.3) into (9.3.2) gives the plasma equation of motion

$$\ddot{y} = Ay'' + By' + Cy - A\eta'' - B\eta' - C\eta . \qquad \ldots (9.3.4)$$

Equation (9.3.4) describes the plasma motion when a sector coil outside the plasma (see Section 7.3) is used to perturb the equilibrium position η.

If the plasma displacement about an unstable non-inertial equilibrium position can be written as

$$\xi = \xi(z) \exp(\gamma t) \qquad \ldots (9.3.5)$$

where γ is the m=1 growth rate (see equation (2.8.4)), then

$$\ddot{\xi} = \gamma^2 \xi \, . \qquad \ldots (9.3.6)$$

Substituting for ξ from equation (9.3.3)) gives

$$\ddot{y} = \gamma^2 y - \gamma^2 \eta \, . \qquad \ldots (9.3.7)$$

Equation (9.3.7) predicts the time dependence of an $m = 1$ unstable plasma when the equilibrium position η is perturbed. Stability is possible if $\eta = y$; that is, the equilibrium position must be perturbed in the same direction as the plasma displacement to produce a restoring force.

9.4 A FEEDBACK CONTROL SYSTEM FOR AN m=1 UNSTABLE THETA PINCH

9.4.1 INTRODUCTION

A feedback control system for an $m=1$ unstable theta pinch, using an existing power amplifier[98] and optical sensing system, is described. The feedback force is produced by perturbing the plasma with the magnetic fields produced by a sector coil (see Section 9.3). Transfer functions[94] for each stage of the control circuit are derived, and Nyquist's criterion[91] applied to determine the overall stability.

9.4.2 The Feedback System

Figure 9.1(a) shows a block diagram of the system. The plasma position is optically monitored to give a signal S directly proportional to the displacement. The output signal S is amplified to a voltage V by a large bandwidth preamplifier. A phase correcting circuit is included, the output of which is used as the grid voltage of a drive amplifier. The output current I from the drive amplifier is passed around a sector coil

to produce an equilibrium shift η; this produces a restoring force on the plasma (see Section 9.3). Each stage of the control system is now discussed in detail.

9.4.3 The Sensing System

Plasma displacements are measured at one or more discrete axial positions by an optical sensing system, illustrated in Fig.9.1(b). The plasma is imaged onto the face of a split light guide, each half of which is optically linked to a photomultiplier. The photomulitplier signals S' are combined to give an output signal S (see Fig.9.1(b)):

$$S = \frac{S'_2 - S'_1}{S'_2 + S'_1} \quad . \qquad \ldots (9.4.1)$$

A plasma displacement $+y$ gives an output signal $+S$; a displacement $-y$ gives an output signal $-S$. The output signal is proportional to the plasma displacement if a Gaussian radial density profile is assumed. The addition is performed to compensate for time varying plasma radii. Motion in the $\pm x$ direction can be resolved by a similar sensing system mounted perpendicular to that shown in Fig.9.1(b).

A sensing system similar to that illustrated has been constructed, without the compensation for changing radius. The signal S was directly proportional to the displacement y for $y \leqslant 0.7\ r_p$, where the plasma radius $r_p \simeq 1.5$ cm.

The transfer function $G(s)$ is defined as[94]

$$G(s) = \frac{\theta_o(s)}{\theta_i(s)} \qquad \ldots (9.4.2)$$

where

s is the Laplace transform variable,

θ_o is the output signal

θ_i is the input signal.

The transfer function of the sensing system is determined by the electron transit time across the photomultipliers. This, and all other pure time

delays in the system, can be combined to give a delay t_d. Then

$$G(s)1 = \frac{S}{y} = k \exp(-t_d) \qquad \ldots (9.4.3)$$

where k is a constant if $y \leqslant 0.7\ r_p$.

9.4.4 The Preamplifier

The sensing system output voltage S is preamplified before it is used to drive the final amplifier stage. A preamplifier with a gain g and risetime τ_A has a transfer function[95]

$$G(s)2 = \frac{V}{S} = \frac{g}{1 + s\tau_A}. \qquad \ldots (9.4.4)$$

τ_A is defined as the time taken for the output voltage V to reach 62.3% of its maximum value when the input signal is a step function. Then

$$\tau_A = 1/\omega_m \qquad \ldots (9.4.5)$$

where ω_m is the 3 d.b. bandwidth.

9.4.5 The Phase Circuit

Provision is made for a phase advance circuit to control the stability of the feedback system. Fig.9.2 illustrates a phase advance circuit with a transfer function[96]

$$G(s)3 = \frac{V_g}{V} = \frac{\alpha(\tau_r s + 1)}{(\alpha\tau_r s + 1)} \qquad \ldots (9.4.6)$$

where V_g is the output voltage across resistance R,

$$\tau_r = R_1 C_1$$

$$\alpha = \frac{R}{R_1 + R}.$$

9.4.6 The Drive Amplifier

The phase circuit output voltage V_g is used as the grid voltage of a drive amplifier. If the amplifier, with conductance g_m and anode resistance r, is used to pass a current I in an inductance L, the transfer function is

$$G(s)4 = \frac{I}{V_g} = \frac{g_m}{(1 + s\tau_T)}, \qquad \ldots (9.4.7)$$

where $\tau_T = L/r$.

9.4.7 The Plasma Equilibrium Position

If the inductive load of the drive amplifier is an n turn sector coil of area A_d, the equilibrium displacement η is given by (see equation (6.3.14) and Section 8.2.7)

$$\eta = \frac{KI}{(1 + (z/b)^2)^{\frac{3}{2}}} \qquad \ldots (9.4.8)$$

where

$$K = - \frac{0.9 \mu_o n A_d}{B_e b^2 \pi} .$$

If the sensing system and sector coil are at the same axial position $z = 0$ the transfer function, neglecting spatial dependence, becomes

$$G(s)5 = \frac{\eta}{I} = K . \qquad \ldots (9.4.9)$$

9.4.8 The Restoring Force

The equation of motion governing an $m = 1$ unstable plasma, neglecting any spatial dependence, is (see equation (9.3.7)) :

$$\ddot{y} = \gamma^2 y - \gamma^2 \eta . \qquad \ldots (9.4.10)$$

If the instability grows symmetrically about the point $z = 0$ (the plasma midplane) the transfer function can be written

$$G(s)6 = \frac{y}{\eta} = \frac{-1}{(\tau_p^2 s^2 - 1)} \qquad \ldots (9.4.11)$$

where $\tau_p = (1/\gamma)$, the instability characteristic time,
$\eta = KI$ (see equation (9.4.9)).

Figure 9.3 shows a block diagram of the complete sensing system. The open loop transfer function

$$T(s) = \sum_i G(s)\, i \qquad \ldots (9.4.12)$$

can be written

$$T(s) = k \exp(-t_d) \frac{g}{(1 + s\tau_A)} \frac{\alpha(\tau_r s + 1)}{(\alpha \tau_r s + 1)} \frac{g_m}{(1 + s\tau_T)} K \frac{(-1)}{(\tau_p^2 s^2 - 1)} \qquad \ldots (9.4.13)$$

The total system gain G_T is

$$G_T = - k \, Kgg_m \alpha . \qquad \ldots (9.4.14)$$

The system described can be used to stabilize motion in the $\pm y$ direction; a second circuit would be necessary to stabilize $\pm x$ motion.

9.5 SYSTEM'S ANALYSIS

Nyquist diagrams are used to determine the stable operating conditions of the feedback control system described in Section 9.4. The Laplace transform variable s in the open loop transfer function $T(s)$ (see equation (9.4.13)) is replaced by an imaginary frequency $i\omega$. The locus of $T(i\omega)$ is plotted as $(X + iY)$ from $\omega = -\infty$ to $\omega = +\infty$. Nyquist's stability criterion[91] for the closed loop response can be written in terms of k_N, where[97]

$$k_N = \left| \frac{\Delta\psi}{2\pi} \right|_{-\infty}^{\infty} - h \qquad \ldots (9.5.1)$$

h is the number of poles of $T(i\omega)$ having positive real parts, $\left| \frac{\Delta\psi}{2\pi} \right|_{-\infty}^{\infty}$ is the number of anticlockwise encirclements of the point $(-1,0)$ by the $T(i\omega)$ locus as ω increases from $-\infty$ to $+\infty$. It is sufficient that k_N, defined by equation (9.5.1), be zero for closed loop stability; that is

$$h = \left| \frac{\Delta\psi}{2\pi} \right|_{-\infty}^{\infty} \text{ for stability} . \qquad \ldots (9.5.2)$$

The open loop transfer function $T(i\omega)$ has one pole with positive real parts, at $i\omega = -1/\tau_p$ (see equation (9.4.13)). The sufficient closed loop stability criterion, equation (9.5.2), becomes

$$\left| \frac{\Delta\psi}{2\pi} \right|_{-\infty}^{\infty} = 1 . \qquad \ldots (9.5.3)$$

Figure 9.4 shows the $T(i\omega)$ locus as a function of the phase advance circuit parameter α (see Section 9.4.5), with the total gain $G_T = 1.0$ (see equation (9.4.14)), and

$\tau_A = 0$; i.e. the preamplifier pole is neglected.

$\tau_T = 1\ \mu s$

$\tau_p = 5\ \mu s$

$\tau_r = 0$ and $2\ \mu s$

$\tau_d = 0$; i.e. no pure time delays.

The loci are drawn for $0 \leq \omega \leq \infty$; for $-\infty \leq \omega \leq 0$ the loci are the mirror images about the X axis of those shown. With no phase advance circuit ($\alpha = 1$, $T_r = 0$) the locus passes through the point $(-1,0)$. For gains $G_T > 1$ the point $(-1,0)$ would be encircled -1 times. For gains $G_T < 1$ the point $(-1,0)$ would not be encircled. The sufficient stability criterion, equation (9.5.3), can be applied to give

$$G_T > 1\ ; \quad \left|\frac{\Delta\psi}{2\pi}\right|_{-\infty}^{\infty} = -1\ , \quad \text{system unstable}$$

$$G_T < 1\ ; \quad \left|\frac{\Delta\psi}{2\pi}\right|_{-\infty}^{\infty} = 0\ , \quad \text{system unstable}$$

For $G_T = 1$ the point $(-1,0)$ is intersected, so that the system is marginally stable. Therefore the feedback control system is not stable without a phase advance circuit.

For $\tau_r = 2\ \mu s$ and $\alpha \leqslant 0.2$, three regions are distinguishable:

$$G_T < 1\ ; \quad \left|\frac{\Delta\psi}{2\pi}\right|_{-\infty}^{\infty} = 0\ , \quad \text{system unstable}$$

$$G_T > 1 > |B|G_T\ ; \quad \left|\frac{\Delta\psi}{2\pi}\right|_{-\infty}^{\infty} = +1, \quad \text{system stable}$$

$$|B|G_T > 1\ ; \quad \left|\frac{\Delta\psi}{2\pi}\right|_{-\infty}^{\infty} = -1, \quad \text{system unstable}\ ,$$

where B is the value of X for $iY = 0$, $G_T = 1$ and $0 < \omega < \infty$, i.e. the value of $T(i\omega)$ when the locus crosses the X axis, as $\omega \to \infty$. Therefore there is a stable operating regime if $\tau_r = 2\mu s$ and $\alpha \leqslant 0.2\mu s$. As α is decreased, the width of the stable regime is reduced; that is, the gain margin[99] is reduced. At the same time the phase margin φ [99]

$$\varphi = \tan^{-1} \frac{|iY|}{|X|} \quad \text{with} \quad |T(i\omega)| = 1 \qquad \ldots (9.5.4)$$

is increased. The system is not stable for $\alpha \geqslant 0.5$.

9.6 A POSSIBLE FEEDBACK STABILIZATION EXPERIMENT

A possible feedback stabilization experiment on a theta pinch with an $\ell = 0$ magnetic field is described, and the overall stability analysed. The instability is produced in a long thetatron similar to the 3.5 m device (see Chapter III), with an enlarged centre region. Fig.9.5(a) shows a front view of the experiment; typical growth rates of 0.1 to 1.0 μs^{-1} would result (see equation (2.8.4)).

An existing power amplifier is considered for the drive stage (see Section 9.4.6)[98]. The 9 MW Machlett triode, ML8618, capable of producing 300 A output current into a 40 μH inductive load with a rise time of 1 μs, is connected to two parallel n turn sector coils, as shown in Fig.9.5(b). This system cancels any induced voltages produced by the time varying external field B_e.

Sector coils were wound to fit the dimensions shown in Fig.9.5(a). The inductance of each coil was

$$L = 0.075\, n^2\ \mu H \qquad \ldots (9.6.1)$$

A maximum amplifier rise time of 1 μs is imposed. This restricts the number of turns in each coil to 33, and the current in each coil to ± 75 A.

The equilibrium displacement constant K (see Section 9.4.7, equation (9.4.8)) can be derived for the drive amplifier stage considered. If the external field $B_e = 10$ kG and the sector coils are a distance $b = 7$ cm from the plasma axis,

$$K = -\ 8.5 \times 10^{-6}\ m\, A^{-1} \qquad \ldots (9.6.2)$$

Plasma displacements $y \leqslant 0.5$ cm are considered. The product $k \alpha g g_m$ (see equations (9.4.13) and (9.4.14)) is the drive amplifier output current

per unit displacement:

$$k\alpha g g_m = \frac{150}{0.5}\ \frac{A}{cm} = 3\times10^4\ A\,m^{-1}\ . \qquad \ldots (9.6.3)$$

It was shown in Section 9.5 that the total system gain G_T (see equation (9.4.14)) must be greater than 1 for stability. For each direction ($\pm x$ and $\pm y$)

$$G_T, = - N k \alpha g g_m K, > 1 \qquad \ldots (9.6.4)$$

where N is the number of drive amplifiers. Substituting from equations (9.6.2) and (9.6.3) into equation (9.6.4) gives

$$N \geq 4\ .$$

Therefore at least 4 amplifiers must be used to stabilize each direction.

Figure 9.6 shows the Nyquist diagram of the open loop transfer function of the control system described, with 5 drive amplifiers. The total gain $G_T = 1.27$. Other variables were

τ_A, the preamplifier rise time, = 0.1 μs,

τ_T, the drive amplifier rise time, = 1.0 μs,

τ_p, the instability characteristic time, = 5 μs,

τ_r, the phase advance circuit time constant, = 2 μs,

t_d, the pure time delay, = 0.1 μs,

α, the phase circuit parameter, = 0.1.

Nyquist's stability criterion (see equation (9.5.2)) shows that the control system is stable, with a phase margin of 4° (see equation (9.5.4)). This is much smaller than the accepted safety margin $\varphi = 40°$ [99], so that any transients in the system would have long decay times. In an experiment, transient displacements would be damped by viscosity, as discussed in Section 8.5.

The above analysis was performed in the time domain, and considered the principle mode only. A real feedback system would excite modes with different wavelengths; in particular the mode with a wavelength equal to

the wavelength of the perturbing fields produced by the sector coil. This excitation would be reduced if the field wavelength and instability wavelenth were matched. A complete solution could then be obtained by solving the equation of motion, equation (9.3.4).

9.7 FEEDBACK STABILIZATION IN TOROIDAL GEOMETRY

The control system described in Section 9.6 is suitable for stabilizing an $m=1$ mode in a straight theta pinch, when the instability position is pre-determined. A more general problem is that of stabilizing an $m=1$ mode in toroidal geometry; for example, a toroidal screw pinch.

The equation of motion describing long wavelength $m=1$ motion in a screw pinch is[100]

$$\frac{\partial^2 \xi}{\partial t^2} - V_A^2(2-\beta)\frac{\partial^2 \xi}{\partial z^2} - 2i\frac{B_\theta}{B_z}\frac{V_A^2}{a}\frac{\partial \xi}{\partial z} = 0 , \qquad \ldots (9.7.1)$$

where a is a measure of the plasma radius

B_θ is the poloidal, or azimuthal, field

B_z is the toroidal, or longitudinal, field.

The system is unstable if the safety factor $q < 1$, where[101]

$$q = \left(1 - \frac{\beta}{2}\right)\frac{B_z}{B_\theta}\frac{2\pi a}{L} , \qquad \ldots (9.7.2)$$

L is the wavelength of the longest mode, $=2\pi R$ for a toroidal plasma, where R is the major radius.

Wesson[100] has shown that a finite number of feedback points can be used to stabilize the system if a delta force function F is applied; that is,

$$F = -\sum_{n=1}^{N} \delta(z - z_n)\,\Phi_n , \qquad \ldots (9.7.3)$$

where F is the feedback force,

Φ_n is a time differential operator,

z_n is the position of the n^{th} feedback point,

N is the total number of feedback points.

A necessary condition for stability is

$$|Nq| > 1 . \qquad \ldots (9.7.4)$$

The plasma is pinned at N points z_n; the propagation velocity allows information to travel between the pinning points and any position z. Dissipation would cause a spatial damping of the m=1 waves with an e-folding length Z_D (see Section 8.5). The distance between the pinning points should be less than the damping length, so that

$$N \geq \frac{2\pi R}{Z_D} . \qquad \ldots (9.7.5)$$

Sector coils can be used to provide the delta feedback force if the characteristic length of the perturbing field, b, is much less than the instability wavelength.

9.8 SUMMARY

It was shown that sector coils similar to those used to excite m=1 Alfven waves[79] (see Chapters VI and VII) could be used to provide a restoring force on an m=1 unstable theta pinch. The restoring force produced was spatially dependent, in contrast to the restoring forces used on the Scylla[85] and Scyllac[86] experiments.

A feedback control system for an m=1 unstable straight theta pinch was designed, using an existing optical sensing system and a 9 MW amplifier[98]. Nyquist's criterion[91] was applied to determine the closed loop stability from the open loop transfer function[94]. It was necessary to introduce a velocity dependent term using a phase advance circuit to obtain overall stability. Typical plasma characteristics were used to show that about 45 MW were necessary to stabilise each coordinate.

'Delta' stabilization of a toroidal screw pinch was shown possible[100], using a finite number of sector coils to pin the plasma. Dissipative damping imposed a minimum number of feedback points if hydromagnetic connection was to be maintained between the sector coils and the plasma.

a) A BLOCK DIAGRAM OF THE FEEDBACK CONTROL SYSTEM

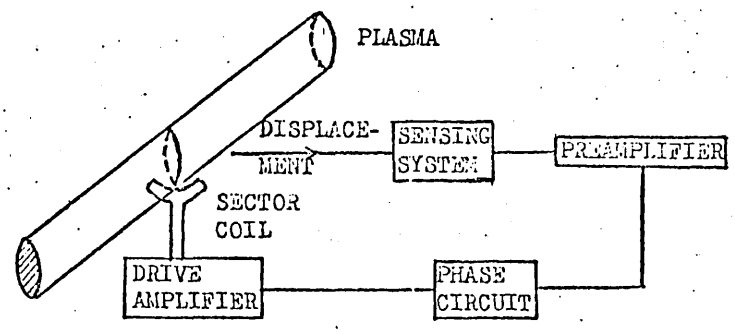

b) THE OPTICAL SENSING SYSTEM

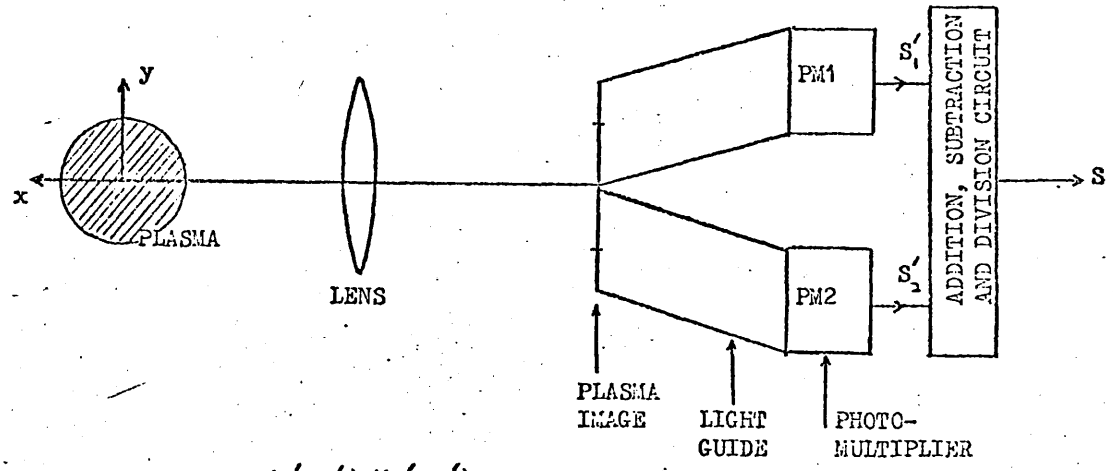

OUTPUT $S = (S'_2 - S'_1)/(S'_2 + S'_1)$

Fig.9.1

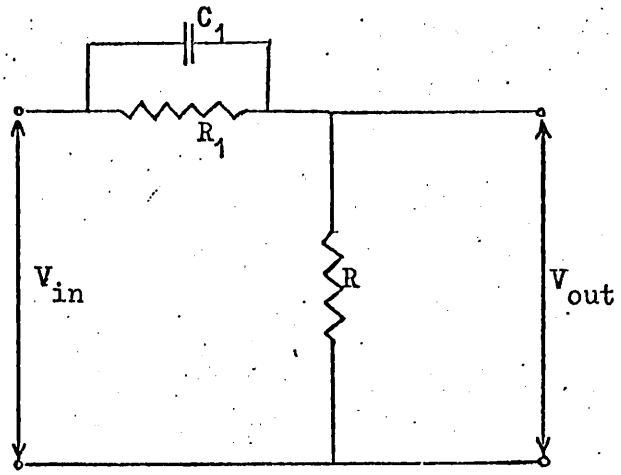

TRANSFER FUNCTION $G(s)1 = \frac{\alpha(\tau_r s+1)}{(\alpha \tau_r s+1)}$

WHERE $\alpha = R/(R+R_1)$

$\tau_r = R_1 C_1$

Fig.9.2
The phase advance circuit

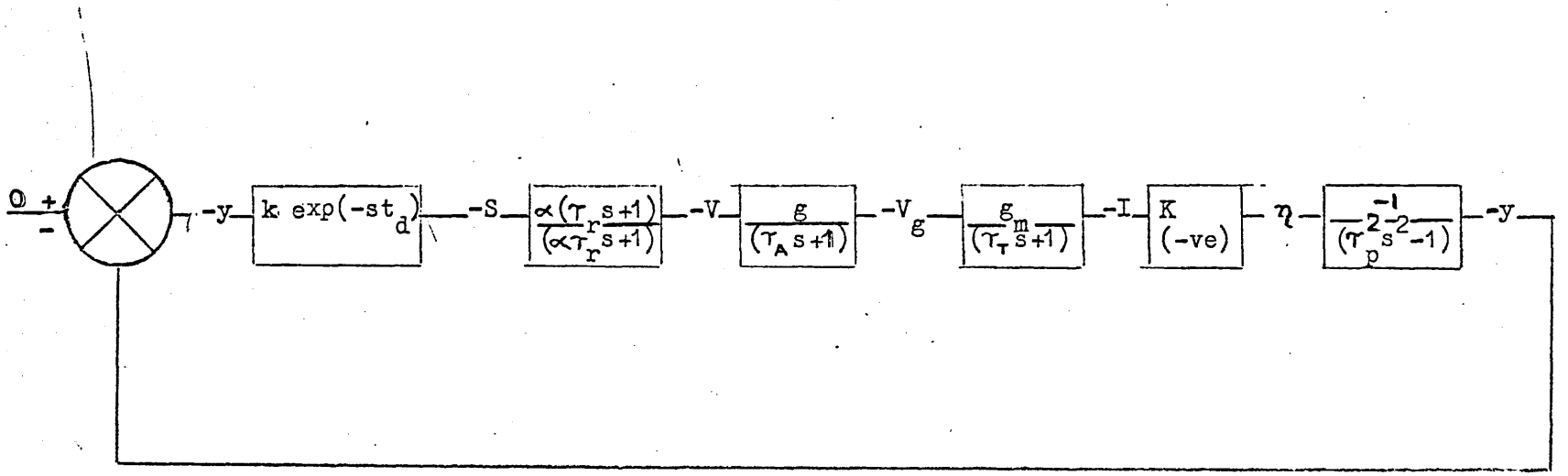

$$\text{OPEN LOOP TRANSFER FUNCTION } T(s) = \sum_i G(s)i = \frac{k\exp(-st_d)}{(\alpha\tau_r s+1)} \cdot \frac{\alpha(\tau_r s+1)}{(\tau_A s+1)} \cdot \frac{g}{(\tau_T s+1)} \cdot \frac{g_m}{(\tau_p^2 s^2-1)} \cdot K \cdot (-1)$$

Fig.9.3

The feedback control system transfer function

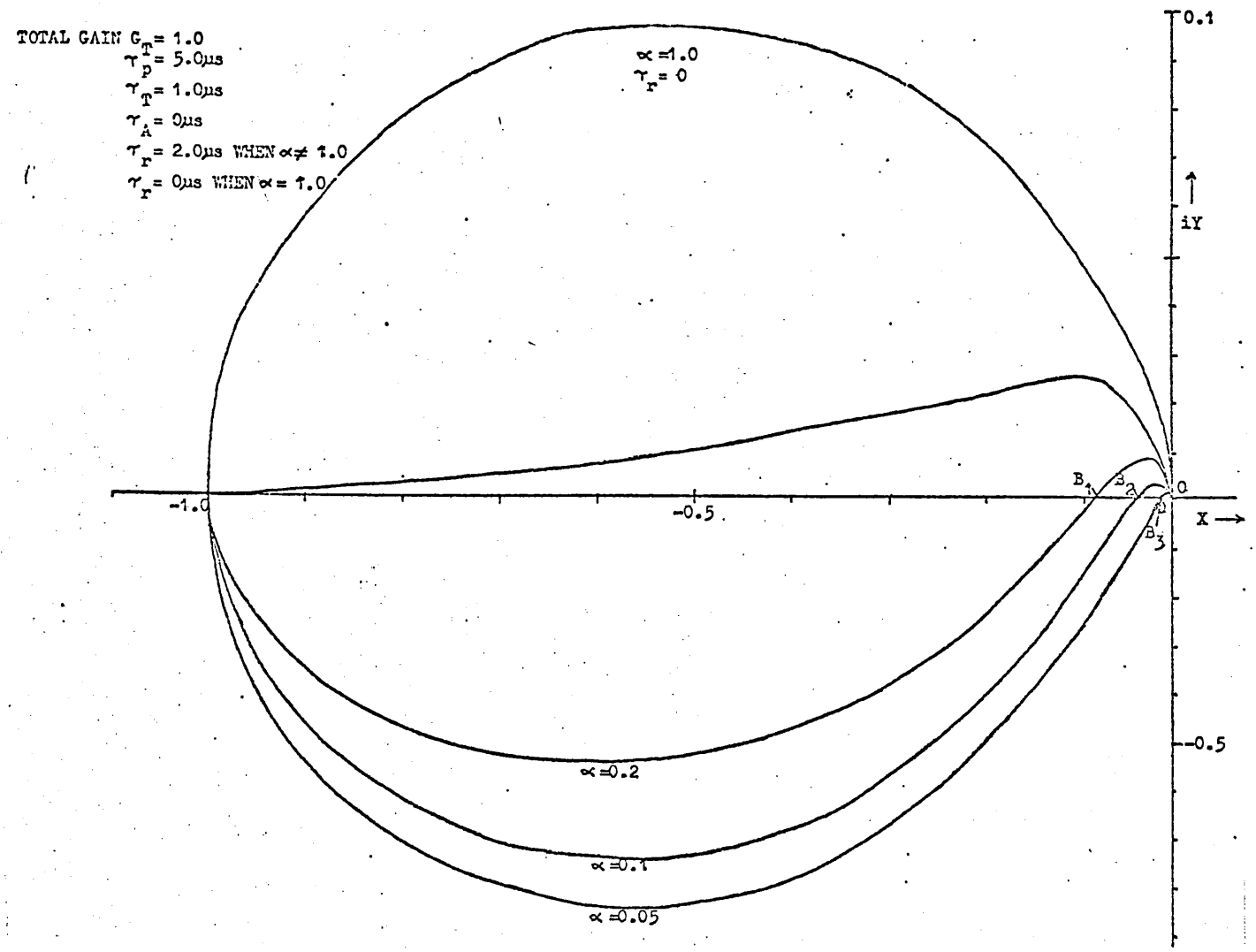

Fig.9.4

The Nyquist diagrams for different phase advance circuit parameters

a) A FRONT VIEW OF THE SECTOR COIL SYSTEM

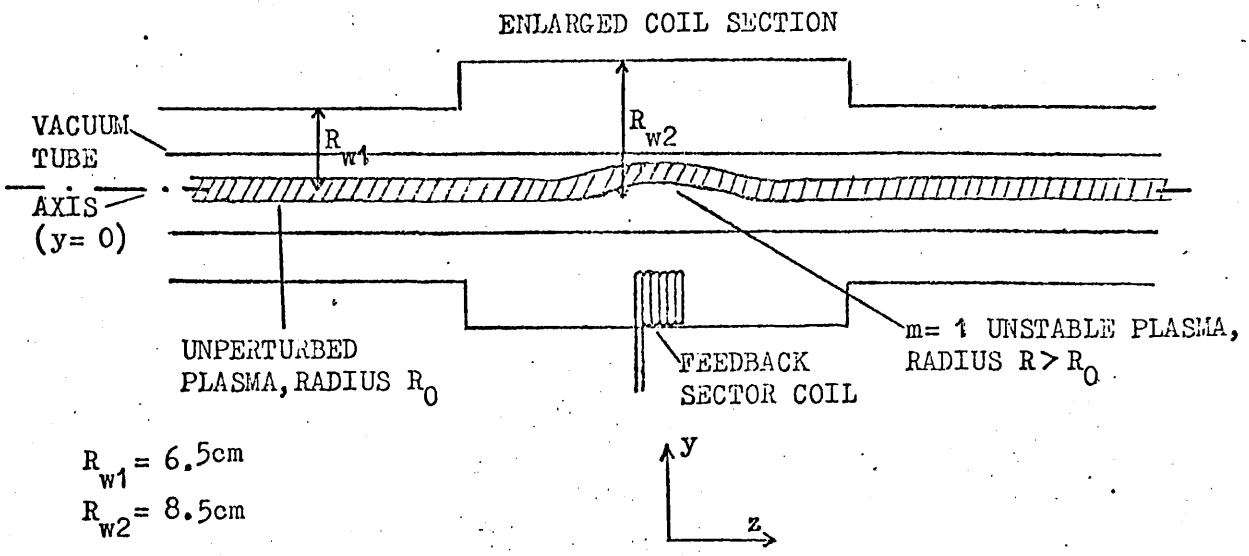

b) A CROSS SECTION OF THE SECTOR COIL SYSTEM

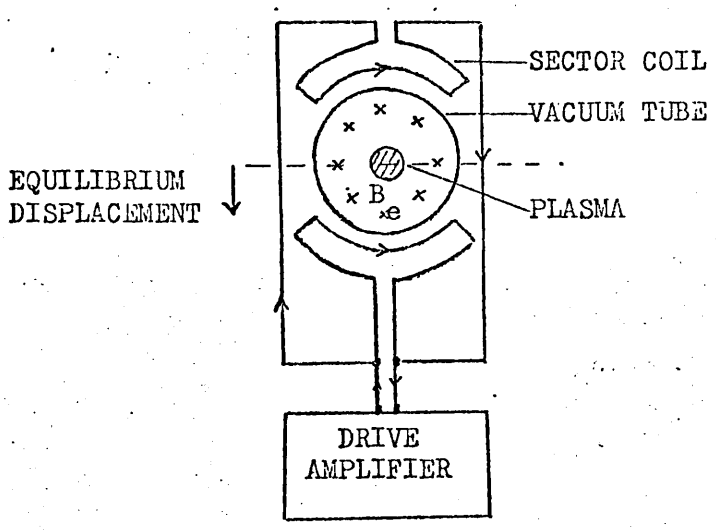

DRIVE AMPLIFIER CURRENT = $\pm I/2$
SECTOR COIL CURRENT = $\pm I/4$
SECTOR COIL INDUCTANCE = 2L
TOTAL INDUCTANCE = L

Fig.9.5

The sector coil system for the proposed feedback control experiment

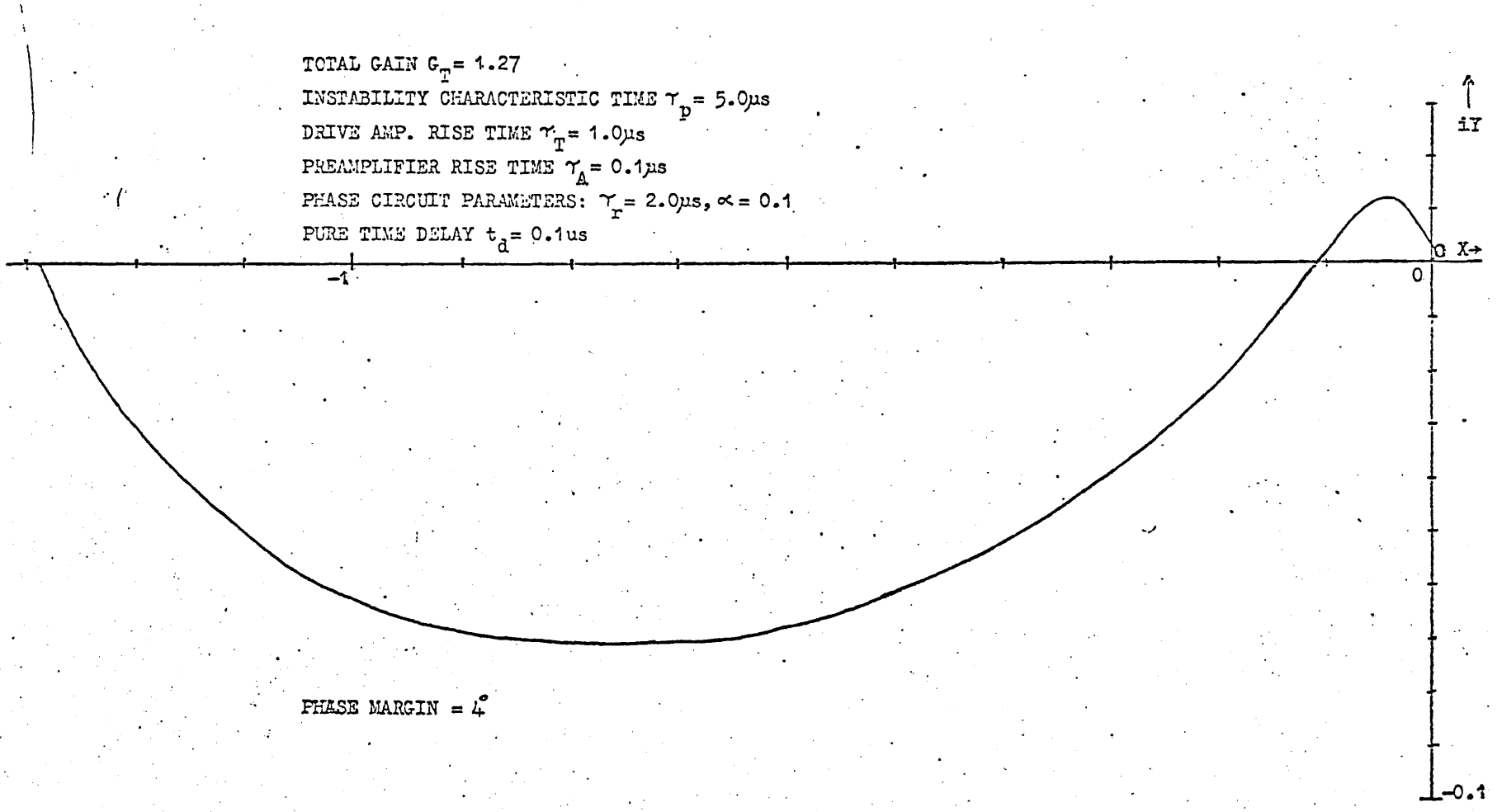

Fig.9.6

The Nyquist diagram for a feedback stabilization system

CHAPTER X

CONCLUSIONS

10.1 SUMMARY

It was found that a small, current carrying (sector) coil outside a theta pinch produced gross plasma displacements in the plane of the coil axis and plasma axis. This displacement, which was proportional to the sector coil current and inversely proportional to the external axial magnetic field, was observed to propagate with a spatial damping. The velocity and damping were dependent on the plasma parameters, and independent of the sector coil parameters.

A theory was presented which considered the restoring forces produced when the plasma equilibrium position was displaced by the sector coil magnetic fields. The resulting equation of motion was solved analytically and numerically to predict $m=1$ Alfven waves as observed. Spatial damping was accredited to resistivity at temperatures below, and viscosity above, 20 eV.

An existing theory based on a calculation of the $\bar{j}\times\bar{B}$ forces over the plasma volume predicted displacements ten times smaller than those measured. This illustrates the importance of considering the equilibrium position when deriving an equation of motion for a plasma in the presence of perturbing fields.

Experiments using a step current waveform in the sector coil showed that the plasma could be moved to an equilibrium which was displaced from the unperturbed equilibrium position. It was concluded that the plasma position could be controlled by passing a pre-determined current in the coil.

The theory describing the plasma motion was extended to derive the restoring force produced by a sector coil on an $m=1$ unstable plasma. This force was shown to be suitable for feedback stabilization; in

particular of the m = 1 instability produced in a bulged theta pinch. The control of toroidal plasmas, using a finite number of sector coils to pin the plasma, was considered.

10.2 APPLICATIONS AND FUTURE WORK

Feedback stabilization of an m = 1 instability in a theta pinch should be attempted. A non-linear on-off (impulsive) system using capacitors to drive the sector coil currents would determine the feasibility; after this amplifiers would replace the capacitors. An optical sensing system should be used to monitor the plasma position (see Section 9.4.3).

The spatial damping of m = 1 plasma motion determines the number of sector coils necessary to control an unstable toroidal plasma (see Section 9.7). Experimental damping lengths were interpreted by assuming that the plasma wavelength was determined by the spatial distribution of the driving force, and not the sector coil current frequency and plasma propagation velocity. More detailed experiments, not possible with the existing apparatus, would determine the frequency dependence of the damping lengths by observing the plasma motion after the first current cycle.

Experiments should be performed to determine the gross motion produced by perturbing fields in plasmas other than theta pinches. Since this work was completed, results obtained by perturbing a screw pinch with transverse fields have been reported[102].

APPENDIX A.1

THE NOMENCLATURE AND A GLOSSARY OF TERMS

A1.1 INTRODUCTION

Definitions of the symbols, and a glassary of some of the terms used in the text, are given. Equations are in MKS units. Definitions are taken, where possible, from the Glossaire de Physique des Plasmas[45].

A1.2 THE NOMENCLATURE

a	Plasma radius
A	Vector potential
A_d	Area of dipole (sector coil)
A_p	Plasma area
b	Distance between dipole (sector coil) axis and plasma axis
B	Magnetic field
B_1	Bias field
$\dot{B}$	Rate of change of magnetic field
c	Velocity of light
C	Capacitance
c_s	Sound speed, $(p\gamma/\rho)^{\frac{1}{2}}$
e	Electronic charge
E	Electric field; energy
F	Force
g , G	Gain
g_m	Conductance
G(s)	Transfer function
h	Field wave number
I	Current ; intensity
j	Current density
k	Wave number
K	Equilibrium displacement constant, η/I
ℓ	Field azimuthal mode number
ℓ , L	Characteristic length
L	Inductance
m	Particle mass; azimuthal mode number (see Section A1.3)
m_p	Percentage of mass collected by implosion
M	Mach number ; line mass ; dipole moment

n	Particle density
N	Particle line density
p	Pressure
p_m	Prandtl number (see Section A1.3, 'hydromagnetic waves') $\frac{\mu_o \mu}{\rho \eta}$
q	Charge
r	Radius vector
r_d	Dipole (sector coil) radius
r_p	Plasma radius
r_W	Wall radius
R_m	Reynolds number (see Section A1.3, 'hydromagnetic waves') $\mu_o VL/\eta$
R	Resistance
R_W	Wall radius
S	Diamagnetism, $\int_0^{A_p} (B_e - B_i)\, dA$; photomultiplier output
s	Laplace transform variable
t	Time
t_{eq}	Equipartition time
t_d	Delay time
t_c	Self collision time
T	Temperature, expressed as an energy kT; tension; period of oscillation; kinetic energy
T_{Av}	Average temperature, $(T_e + T_i)/2$
$T(s)$	Open loop transfer function
v	Velocity
V	Voltage; characteristic velocity
V_A	Alfven velocity, $B/(\mu_o \rho)^{\frac{1}{2}}$ (see Section A1.3 'hydromagnetic waves')
W	Potential energy
y	Displacement
Y_m	Admittance
Z_D	Damping length
α	Ionization coefficient, $n_e/(n_e + n_i)$; phase circuit parameter; image current parameter
β	Beta, $p/(p + \frac{B_i^2}{2\mu_o})$ (see Section A1.3)
γ	Ratio of specific heats; growth rate; impurity concentration
δ_ℓ	Equilibrium displacement
η	Resistivity; equilibrium position.
θ	Poloidal coordinate

λ	Wavelength
λ_{mfp}	Mean free path between binary collisions
μ	Viscosity
μ_o	Permeability of free space
ξ	Plasma position
ρ	Mass density
τ	Characteristic time; rise time
τ_{pI}	Delay between preionization current and compression current
φ	Phase margin; trapped flux
ω	Angular frequency
ω_c	Cyclotron frequency, qB/m .

Subscripts

e	Electron External to the plasma
i	Ion Internal (inside the plasma)
$\parallel$	Component parallel to the magnetic field
$\perp$	Component perpendicular to the magnetic field
n	Normalised
pI	Preionization
z	Axial

A1.3 A GLOSSARY OF TERMS[45]

Collisional plasma:	A plasma where λ_{mfp} (see Section A1.2) is less than any characteristic length, i.e. $\lambda_{mfp} < L$.
Collisionless plasma:	A plasma where $\lambda_{mfp} > L$
High β plasma :	$\beta > 0.1$
Low β plasma :	$\beta < 0.1$
Macro, or gross, instability:	An instability which can be described by the MHD equations
Microinstability:	An instability described by fluctuating electric and magnetic fields.
Quasi neutrality:	$n_i \simeq n_e$
Bremsstrahlung radiation:	Continuous radiation emitted by free electrons in an ionized gas, retarded by their interactions with charged particles.

Recombination : The process whereby two particles of opposite charge recombine, the excess energy being emitted as a photon

Three body recombination : $e^- + X + A^+ \rightarrow X + A^o$

An electron encounters a particle X in the presence of a positive ion A^+. The electron imparts some energy to X, is slowed down, and becomes attached to the positive ion. X is accelerated.

Beta (β) : If a fluid is introduced into a system of straight, parallel field lines so as to leave the symmetry unchanged, the momentum equation becomes

$$\nabla\left(p + \frac{B^2}{2\mu_o}\right) = 0$$

If the fluid has an internal field B_i and an external field B_e, the equation becomes

$$p + \frac{B_i^2}{2\mu_o} = \frac{B_e^2}{2\mu_o}$$

Therefore the plasma behaves as a diamagnetic material. β is defined as

$$\beta = \frac{p}{(B_i^2/2\mu_o + p)}$$

so that

$$\beta = 1 - \frac{B_i^2}{B_e^2}$$

'Frozen in' field lines: In an infinitely conducting medium, Maxwell's equations give

$$\frac{\partial \bar{B}}{\partial t} = \nabla \times (\bar{V} \times \bar{B})$$

Integrating over an arbitrary surface S gives the flux φ;

$$\frac{\partial \varphi}{\partial t} + \oint \bar{B}\,(V \times d\bar{S}) = 0$$

This equation expresses the constancy of flux through any material surface. Therefore the field lines may be considered as 'frozen in' the fluid[46].

Hydromagnetic waves:

If an unbounded inifinite medium is perturbed, Alfven waves may occur[47]. These can be described using the MHD equations; they have a phase velocity

$$V_A = \pm \frac{B}{(\mu_o \rho)^{\frac{1}{2}}}$$

Including resistivity and viscosity in the analysis leads to a damping of the waves[47], with an e-folding distance

$$Z_D = \frac{\mu_o V_A \lambda^2}{2\pi^2 \left(\eta + \frac{\mu \mu_o}{\rho} \right)}$$

where λ is the wavelength;

η is the resistivity

μ/ρ is the kinematic viscosity.

This can be written in terms of the Prandtl number p_m[48], and the Reynolds number R_m[48] as

$$Z_D = \frac{R_m \lambda}{2\pi^2 (1 + P_m)} .$$

The m number:

Small amplitude plasma displacements can be expressed in Fourier components. For a cylindrical system with a displacement $\bar{\xi}$;

$$\bar{\xi} = \left[\bar{\xi}_r(r) + \bar{\xi}_\theta(r) + \bar{\xi}_z(r) \right] \exp \left[i(\omega t + m\theta + kz) \right]$$

where m is the azimuthal mode number

k is the axial wave number

ω is the frequency

APPENDIX A.2

THE DIAGNOSTIC TECHNIQUES

A2.1 INTRODUCTION

The standard diagnostic techniques used for the experiments (Chapters V and VII) are described. For each parameter measured the necessary equations are quoted, and the percentage errors given.

A2.2 VOLTAGE MEASUREMENTS

Voltages were measured, using calibrated resistance-capacitance dividers, to $\pm 3\%$.

A2.3 CURRENT AND IMPEDANCE MEASUREMENTS

Rogowski coils[49] were used to measure electric currents; each coil was calibrated from a known current. For a series L C R circuit producing underdamped oscillations[50],

$$I = \frac{V}{\omega L} \exp\left(-\frac{Rt}{2L}\right) \sin \omega t \qquad \ldots (A2.1)$$

The current can be calculated from the measured values of ω and the ratio of the first two current maxima $\hat{I}_1/\hat{I}_2$, and known values of C and V. Values of resistance and inductance are given by

$$R = 2\ell n \left(\hat{I}_1/\hat{I}_2\right) \frac{L}{T} \qquad \ldots (A2.2)$$

and

$$L = \frac{4\,T^2}{C\left(4\ell n^2 \left(\frac{\hat{I}_1}{\hat{I}_2}\right) + 16\,\pi^2\right)} \qquad \ldots (A2.3)$$

where T is the period, $2\pi/\omega$. Errors in the values of I, R and L were $\pm 5\%$.

A2.4 MAGNETIC FIELD MEASUREMENTS

Magnetic fields inside the thetatron were calculated using the formula for an n turn solenoid, length ℓ;[37]

$$B = \frac{\mu_o n I}{\ell} \qquad \ldots (A2.4)$$

It was assumed that the field external to the plasma, B_e, was given by equation(A2.4). Errors were ± 5%.

Small search coils were used to determine the spatial variation of magnetic fields at atmospheric pressure[51]. These coils were calibrated either from the known field inside the thetatron, or using the search coil area and integrating circuit parameters. The independent calibration had errors of ± 10%. The spatial resolution of the search coils used was ± 0.3 cm.

A2.5 GAS PRESSURE MEASUREMENTS

A Pirani gauge, calibrated from a McLeod gauge, was used to measure the initial gas filling pressure to ± 3%.

A2.6 INTENSITY PROFILE MEASUREMENTS[41]

The plasma radiation was viewed with an STL/TRW electronic image converter camera at a range of 50 cm. One slit in the compression coil (see Fig.3.2(a)) was photographed through normal glass optics with an aperture of f 2.8 to f 5.6. This produced an image on the image converter tube photocathode, the phosphor having a range of 3,900 to 6,000 Å. The slit image was streaked across the anode, poducing a time resolved, or streak, picture. The film used was either Polaroid 10,000 ASA or Ilford HP4.

The time resolution is given by

$$\frac{\text{Slit width} \times \text{magnification} \times \text{streak time}}{\text{streak distance on film}} \qquad \ldots (A2.5)$$

For the photographs in the text, (e.g. Fig.4.2(b)), this corresponded to ± 3% of the total streak time.

The spatial resolution was determined by the photocathode, and was quoted at 250 resolvable points per cm.

The intensity resolution was governed by the film used. For low light intensities, each picture was calibrated using a uniformly illuminated photographic density wedge.

Each plate produced was analysed using a Hilger and Watts microdensitometer. The plasma image was scanned radially, and compared with a scan of the density wedge image. The plasma relative light intensity profile could then be derived. Because the profile obtained represented the intensity I_x as viewed by an observer looking along a number of parallel chords, Abel's integral inversion[52] was used to obtain the radial profile I_r. This calculation was performed computationally.

A2.7 ELECTRON PARTICLE DENSITY PROFILE MEASUREMENTS[41]

The intensity of continuum radiation emitted in the visible region from hydrogen like ions can be written[53]

$$I_\lambda = 1.5\times10^{-29} \frac{n_e n_i}{\lambda^2 T_e^{\frac{1}{2}}} \text{ watts cm}^{-3} \text{ sterads}^{-1} \text{ A}^{-1} \qquad \ldots \text{(A2.6)}$$

where I_λ is the bremsstrahlung intensity at a wavelength λ.
Radial determinations of the temperature in theta pinches have shown that T_e is not strongly dependent on the radius[42]. Therefore equation (A2.6) can be written

$$I \propto n_e^2 , \qquad \ldots \text{(A2.7)}$$

where I is the intensity emitted over the visible region. Thus the radial electron density profiles can be directly obtained from the radial intensity profiles (see Section A2.6). Because the intensity profiles are relative, the integral of the electron density must be normalised to the measured line density (see Section A2.9),

$$N_e = 2\pi \int_0^{r_W} n_e(r)\, r\, dr \qquad \ldots \text{(A2.8)}$$

where N_e is the measured particle line density
r_W is the vacuum tube radius.

The normalisation was performed computationally to give absolute values of electron density. This method of determining the electron density has been found to give results in agreement with laser scattering results[42].

Errors were calculated as a standard deviation by the computer program. Impurities present in the plasma would effect the validity of equation (A2.6); 0.25% of oxygen results in an error of 4%. The total error in the electron density was taken as ± 5%.

A2.8 DIAMAGNETIC MEASUREMENTS[54]

The plasma diamagnetism S is defined as

$$S = \int_0^{A_p} (B_e - B_i)\, dA \qquad \ldots (A2.9)$$

where A_p is the plasma area. S was measured using two single turn coils of different area, placed concentrically around the vacuum tube and inside the compression coil (see Fig.A2.1 and Fig.3.2(a), marked 'double loops').

The two coils 1 and 2 in Fig.A2.1 with areas A_1 and A_2 each measure the rate of change of flux. After integration of the output voltages, the two signals S'_1 and S'_2 are

$$S'_1 = k_1\left((A_1 - A_p)\, B_e + \varphi\right) \qquad \ldots (A2.10)$$

$$S'_2 = k_2\left((A_2 - A_p) B_e + \varphi\right) \qquad \ldots (A2.11)$$

where k_1 and k_2 are circuit constants, and φ is the flux trapped inside the plasma. The two signals were differenced, and balanced for vacuum conditions, to give

$$S'_o = S'_{1o} - S'_{2o} = (k_1 A_1 - k_2 A_2)\, B_e = 0 \qquad \ldots (A2.12)$$

where subscript zero refers to vacuum conditions.

With a plasma present,

$$S' = S'_1 - S'_2 = k_1\, (A_p B_e - \varphi)\left(\frac{A_1}{A_2} - 1\right) \qquad \ldots (A2.13)$$

Therefore the diamagnetism S can be written

$$S = A_p B_e - \varphi \qquad \ldots (A2.14)$$

$$= \frac{S'}{S'_{1o}} \frac{A_1 B_e}{(A_1/A_2 - 1)} \cdot \qquad \ldots (A2.15)$$

The coils used in the experiments had areas $A_1 = 127$ cm^2 and $A_2 = 73$ cm^2. For each plasma produced, S' was recorded as a function of time, as in Fig.4.2(b). Normalisative with respect to S'_{1o} was performed during the analysis. The errors were ± 7%.

A2.9 LINE MASS MEASUREMENTS

After the implosion stage the plasma oscillates radially about its axis (see Section 2.3). These oscillations appear on streak photographs and diamagnetic signals (see Fig.4.2(b)). A theory by Niblett and Green[9] relates the oscillation frequency ω to the plasma line mass (mass per unit length), by assuming that the plasma, initially confined to a thin annulus is swept up by a snowplough mechanism[4]. A correction for the mass profile leads to the equation[55]

$$\omega = g \sqrt{\frac{B_e^2}{M}} \qquad \ldots (A2.16)$$

where g is a correction factor, $\simeq 1$; M is the line mass. Therefore the particle line density N can be obtained if the particle mass is known.

Experimental determinations of M showed that the mass collected increased over typically 3 oscillations, and then was time independent. Values of M quoted in the text refer to the stationary cases. Errors were estimated as ± 10%.

A2.10 MEASUREMENTS OF BETA (β) AND TEMPERATURE

Average values of β (written $\langle\beta\rangle$), and a plasma radius r_p, are defined as those values of β and r of an equivalent plasma, with a square density and temperature distribution, which has the same line density, temperature and diamagnetism as the experimental plasma. For an experimental

plasma with a uniform temperature distribution and a Gaussian pressure profile[34],

$$\langle\beta\rangle = \frac{\beta \text{ on axis}}{2} \qquad (\text{i.e. } \langle\beta\rangle_{max} = 0.5) \qquad \ldots (A2.17)$$

and

r_p = radius when n_e falls to 0.14 n_e on axis . ... (A2.18)

Using the definition of β (see Section A1.3) and assuming pressure balance

$$p + \frac{B_i^2}{2\mu_o} = \frac{B_e^2}{2\mu_o} \qquad \ldots (A2.19)$$

the diamagnetism of a plasma with a uniform temperature distribution and a Gaussian pressure profile may be written

$$S = \int_0^{A_p} (B_e - B_i)\, dA$$

$$= A_p B_e (1 - \sqrt{1 - \langle\beta\rangle}) \qquad \ldots (A2.20)$$

where $A_p = \pi r_p^2$

and $A_p B_i \geq 0$; i.e. the trapped flux is positive with respect to the external field B_e.

The plasma radius r_p can be obtained from the electron density profiles (see Section A2.7). Equation (A2.20) can be rearranged to give

$$\langle\beta\rangle = 1 - \left(1 - \frac{S}{A_p B_e}\right)^2 \qquad \ldots (A2.21)$$

Values of $\langle\beta\rangle$ were calculated using equation (A2.21) and the measured diamagnetism.

Using the definition of β and line density N_e (equation (A2.8)), equation (A2.21) can be written

$$T_{Av} = \frac{S\, B_e\, \langle\beta\rangle}{4\mu_o\, k\, N_e\, (1 - \sqrt{1 - \langle\beta\rangle})} \qquad \ldots (A2.22)$$

where

$$T_{Av} = (T_e + T_i)/2 \; . \qquad \ldots (A2.23)$$

Equation (A2.23) was used to derive the plasma average temperature from the measured values of diamagnetism S, average beta $\langle\beta\rangle$, external field B_e

and particle line density N_e (see Section A2.9). Thus the plasma radius, electron density, line mass, average temperature and average beta can be derived using a pair of loops and an intensity profile derived from a streak picture. The errors were estimated as

quantity	error
r_p	± 5%
$\hat{n}_e$	± 5%
M	± 10%
T_{Av}	± 20%
$\langle\beta\rangle$	± 15% .

A2.11 TEMPERATURE MEASUREMENTS USING IMPURITY RADIATION

The life history of carbon lines radiated from the plasma was used to check the diamagnetic temperature results (see Section A2.10). A computer code[56] was available which predicted the temporal history of any line radiation, given the electron density and temperature time history, by considering :

(a) The collisional ionization of an atom or ion by an electron.

(b) The recombination of an ion with an electron.

(c) The collisional excitation of an atom or ion by an electron.

The plasma was imaged on the entrance slit of a Bausch and Lomb grating monochrometer (1200 lines mm^{-1}, dispersion 16 Å mm^{-1}, aperture f 4.4). A photomultiplier was positioned at the exit slit, and the signals displayed on an oscilloscope. The time histories of the C^{I} to C^{III} lines were recorded on a shot-to-shot basis.

The electron density time history obtained from the streak photographs (see Section A2.7) and the average temperature history obtained from the diamagnetism (see Section A2.10) were used as input data for the computer code. The predicted line radiation histories were then compared with the experimental histories, and the diamagnetic temperature input data

adjusted until the correct histories were predicted. In this way the diamagnetic temperature could be checked.

The above method was used on the 2 mm theta pinch, which produced a plasma with diamagnetic temperatures ≤ 10 eV (see Fig. 7.4). It was found that the diamagnetic temperature, after 3 μs, correctly predicted the line radiation histories, but for times less than 3 μs the diamagnetic temperature was as much as 50% too large. The errors were ± 20%; this change in temperature resulted in the predicted line radiation time histories being outside the scatter of the experimental time histories.

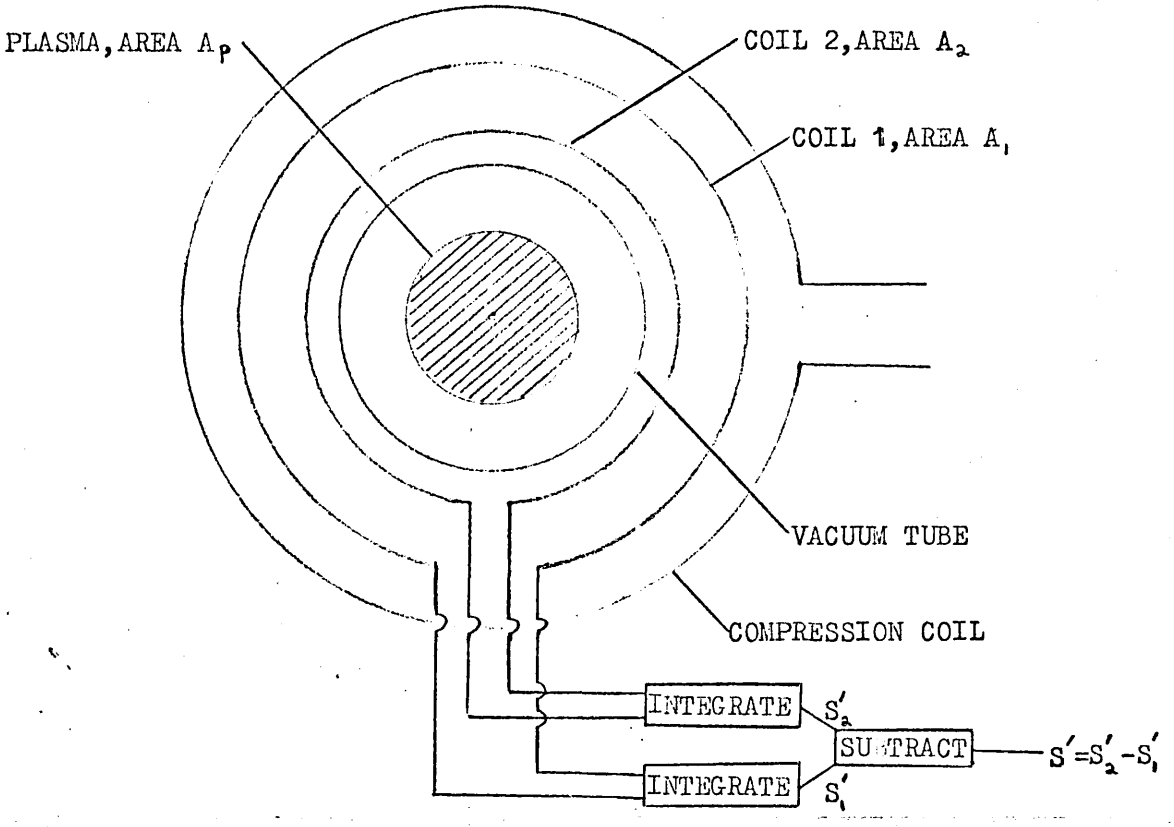

$$\text{DIAMAGNETISM} \quad S = \int_0^{A_p} (B_e - B_i)\,dA = \frac{S' A_1 B_e}{S_{10}' (A_1/A_2 - 1)}$$

where subscript 0 implies vacuum conditions

B_e is the external field

B_i is the internal field

Fig.A2.1

The double coil system for measuring the diamagnetism

PARAMETER		ERROR, %
VOLTAGE	V	3
CURRENT	I	5
MAGNETIC FIELD	B	5
PRESSURE	p	3
TIME	t	3
RATE OF CHANGE OF MAGNETIC FIELD	$\dot{B}$	8
PARTICLE DENSITY	n	5
DIAMAGNETISM	S	7
PLASMA RADIUS	r_p	5
LINE MASS	M	10
BETA	β	15
TEMPERATURE	T_{Av}	20
INDUCTANCE	L	5
RESISTANCE	R	5

ERROR BARS INDICATE THE MOST PROBABLE ERROR r :

$$r = 0.85 \frac{\Sigma_i x_i}{(n-1)n}$$

where x_i is the deviation of the i^{th} observation from the mean

n is the number of observations

Fig.A2.2

The experimental errors

APPENDIX A.3

THE ANALYTIC SOLUTION OF THE THETA PINCH EQUATION OF MOTION

A3.1 INTRODUCTION

The analytic solution of the equation of motion of a theta pinch with a distributed, time dependent driving force is described. An analogy between the plasma and a string under tension is made. The general approach, using operational calculus, consists of finding the steady state response to a simple harmonic force applied at a point. The response to an impulsive force applied at a point is then found; the response to a general force is obtained by integrating over the length of application and time duration of the force. The resulting solution applies to any system obeying a one dimensional wave equation with a driving force. To obtain the motion of a theta pinch the force term derived in Chapter VI is used as the driving force.

A3.2 THE GENERAL APPROACH

The equation of motion describing a theta pinch in the presence of a magnetic dipole with its axis parallel to the plasma axis is (see Section 6.4, equation (6.4.3))

$$\frac{\partial^2 y}{\partial t^2} - V^2 \frac{\partial^2 y}{\partial z^2} + V^2 \frac{\partial^2 \eta}{\partial z^2} = 0 \qquad \ldots \text{(A3.1)}$$

where $V = V_{m=1} = V_A\sqrt{2-\beta}$

$\eta = \eta(z,t)$, the equilibrium position.

Equation (A3.1) can be written as (see equation (6.4.4))

$$\frac{\partial^2 y}{\partial t^2} - V^2 \frac{\partial^2 y}{\partial z^2} = \frac{F(z,t)}{M} \qquad \ldots \text{(A3.2)}$$

where

$$\frac{F(z,t)}{M} = - V^2 \frac{\partial^2 \eta}{\partial z^2} \qquad \ldots \text{(A3.3)}$$

and M is the line mass. The function $F(z,t)$ represents a force. Equation (A3.2) describes the motion of a string under a tension $T = V^2 M$, with a distributed driving force. This general equation is solved, and

then the force on the plasma (equation (6.6.1)) is substituted for $F(z,t)$.

The solution consists of three parts:

(1) The steady state response of the string is obtained for a simple harmonic force applied at $z = \xi$, described by $f(\xi)e^{-i\omega t}$. The admittance[75] $Y_m(\xi, z, \omega)$, the ratio of the steady state velocity to the simple harmonic driving force, is then obtained.

(2) The response of the string to an impulsive force applied at $z = \xi$ is derived, using the function $Y_m(\xi, z, \omega)$ and operational calculus[75]. This gives $y_\delta(\xi, z, t)$.

(3) The response of the string to a general force $F(z,t)$ is then obtained by integrating over the length of application of the force, ℓ, and the time duration τ for which it is applied[76]:

$$y(z,t) = \int_{-\infty}^{\infty} d\tau \int_{0}^{\ell} d\xi \; F(\xi,\tau) \; y_\delta(\xi,z,t-\tau) \qquad \ldots \text{(A3.4)}$$

A3.3 THE ADMITTANCE

Using the Fourier transforms,

$$f(t) = \int_{-\infty}^{\infty} F(\omega) \; e^{-i\omega t} \; d\omega \qquad \ldots \text{(A3.5)}$$

$$y(t) = \int_{-\infty}^{\infty} X(\omega) \; e^{-i\omega t} \; d\omega \qquad \ldots \text{(A3.6)}$$

and the Fourier transform pairs

$$F(\omega) = \frac{1}{2\pi} \int_{-\infty}^{\infty} f(t) \; e^{i\omega t} \; dt \qquad \ldots \text{(A3.7)}$$

$$X(\omega) = \frac{1}{2\pi} \int_{-\infty}^{\infty} y(t) \; e^{i\omega t} \; dt \qquad \ldots \text{(A3.8)}$$

the response of a string to a force $f(t)$ applied at $z = \xi$ can be written

$$y(\xi,z,t) = \int_{-\infty}^{\infty} \frac{F(\xi,\omega)}{-i\omega} \; e^{-i\omega t} \; Y_m(\xi,z,\omega) \; d\omega \qquad \ldots \text{(A3.9)}$$

where

$$Y_m(\xi,z,\omega) = - \frac{i\omega X(\xi,z,\omega)}{F(\xi,\omega)} \; . \qquad \ldots \text{(A3.10)}$$

$Y_m(\xi,z,\omega)$ is the admittance, and is equivalent to the ratio of the steady state velocity to the force, when the force is simple harmonic, i.e.

$$Y_m(\xi,z,\omega) = \frac{\dot{y}}{f(\xi)e^{-i\omega t}} \qquad \ldots \text{(A3.11)}$$

If the applied force is a Dirac delta function $\delta(t)$, the response of the string is obtained by substituting $\delta(t)$ for $f(t)$ in equation (A3.7) and then substituting $F(\omega,\xi) = \frac{1}{2\pi}$ into equation (A3.9) to give[75]

$$y_\delta(\xi,z,t) = \frac{1}{2\pi}\int_{-\infty}^{\infty} \frac{e^{-i\omega t}\, Y_m(\xi,z,\omega)}{-i\omega}\, d\omega \ . \qquad \ldots \text{(A3.12)}$$

This is then substituted into equation (A3.4) to give $y(z,t)$.

A3.4 THE RESPONSE TO A SIMPLE HARMONIC FORCE

Consider a string, length ℓ, held between two rigid supports, acted on by a force $f(\xi)\ e^{-i\omega t}$ applied at $z = \xi$. If a simple harmonic force of frequency ω is applied at $z = \xi$, the part of the string for $z < \xi$ should be part of a standing wave that is zero for $z = 0$, such as $A\sin\left(\frac{\omega z}{V}\right)$. For $z > \xi$ the string should be part of a standing wave that is zero for $z = \ell$, such as $B\sin\left[\frac{\omega}{V}(\ell - z)\right]$. At $z = \xi$ there will be a sudden change of slope, and $-T$ times this change in slope must equal the applied force (T is the tension). Using the above method, and using the relationship $T = MV^2$, the displacement y can be written

$$y(\xi,z,t) = \begin{cases} \dfrac{f(\xi)e^{-i\omega t}}{MV\omega} \dfrac{\sin\left[\frac{\omega}{V}(\ell - \xi)\right]}{\sin\left(\frac{\omega\ell}{V}\right)} \sin\left(\frac{\omega z}{V}\right) & \text{for } z < \xi \\ \dfrac{f(\xi)e^{-i\omega t}}{MV\omega} \dfrac{\sin\left(\frac{\omega\xi}{V}\right)}{\sin\left(\frac{\omega\ell}{V}\right)} \sin\left[\frac{\omega}{V}(\ell - z)\right] & \text{for } z > \xi \end{cases} \qquad \ldots \text{(A3.13)}$$

The admittance Y_m can now be calculated using equation (A3.11)

$$\overline{Y_m(\xi,z,\omega)} = \begin{cases} \dfrac{-i}{MV} \dfrac{\sin\left[\frac{\omega}{V}(\ell - \xi)\right]}{\sin\left(\frac{\omega\ell}{V}\right)} \sin\left(\frac{\omega z}{V}\right) & \text{for } z < \xi \\ \dfrac{-i}{MV} \dfrac{\sin\left(\frac{\omega\xi}{V}\right)}{\sin\left(\frac{\omega\ell}{V}\right)} \sin\left[\frac{\omega}{V}(\ell - z)\right] & \text{for } z > \xi \end{cases} \qquad \ldots \text{(A3.14)}$$

$y(\xi,z,t)$ is the steady state solution of equation (A3.2) with $F(z,t) = f(\xi)e^{-i\omega t}$.

A3.5 THE RESPONSE TO AN IMPULSIVE FORCE

The response of the string to an impulsive force at $t = 0$ applied at $z = \xi$, namely $f(z,t) = \delta(z-\xi)\delta(t)$, is given by equation (A3.12). Substituting for Y_m from equation (A3.14) into equation (A3.12) gives

$$y_\delta(\xi,z,t) = \frac{1}{2\pi MV}\int_{-\infty}^{\infty} \frac{e^{-i\omega t}}{\omega}\,\frac{P(\omega,z)}{\sin\left(\frac{\omega\ell}{V}\right)}\,d\omega \qquad \ldots (A3.15)$$

where $$P(\omega,z) = \begin{cases} \sin\left[\frac{\omega}{V}(\ell-\xi)\right]\sin\left(\frac{\omega z}{V}\right) & \text{for } z < \xi \\ \sin\left(\frac{\omega\xi}{V}\right)\sin\left[\frac{\omega}{V}(\ell-z)\right] & \text{for } z > \xi \end{cases} \qquad \ldots (A3.16)$$

The poles of the integrand are $\omega = \frac{m\pi V}{\ell}$, where m is an integer, positive or negative. These correspond to the natural frequencies of the string. Near an even pole the quantity $\sin\left(\frac{\omega\ell}{V}\right)$ approaches the value $\frac{\ell}{V}\left(\omega - \frac{m\pi V}{\ell}\right)$. Therefore for $\omega \to \frac{m\pi V}{\ell}$ (m even) the integrand approaches the value

$$\frac{1}{2\pi M\ell}\,\frac{e^{-im\pi Vt/\ell}}{m\pi V/\ell}\,\frac{\sin\left(m\pi - \frac{m\pi\xi}{\ell}\right)}{\left(\omega - \frac{m\pi V}{\ell}\right)}\sin\left(\frac{m\pi z}{\ell}\right) \text{ for } z < \xi \qquad \ldots (A3.17)$$

The residue of this expression, its limiting value when multiplied by $\left(\omega - \frac{m\pi V}{\ell}\right)$ as this factor approaches zero, is

$$\frac{-1}{2\pi^2 mVM}\,e^{-im\pi Vt/\ell}\sin\left(\frac{m\pi\xi}{\ell}\right)\sin\left(\frac{\pi m z}{\ell}\right) \quad \text{for } 0 < z < \ell \qquad \ldots (A3.18)$$

For m odd, the factor $\sin\left(\frac{\omega\ell}{V}\right)$ approaches $\frac{-\ell}{V}\left(\omega - \frac{m\pi V}{\ell}\right)$.

Now $\sin\left(m\pi - \frac{m\pi\xi}{\ell}\right) = -\sin\left(\frac{m\pi\xi}{\ell}\right)$. Therefore the residue of the integrand for m odd is the same as for m even. The final value of the integral, $-2\pi i$ times the sum of the residues on or below the real ω axis, gives a displacement (equation (A3.15))

$$y_\delta(\xi,z,t) = \begin{cases} 0 & \text{for } t<0 \\ \dfrac{-1}{i\pi MV}\displaystyle\sum_{m=1}^{\infty}\frac{1}{m}\sin\left(\frac{\pi m\xi}{\ell}\right)\sin\left(\frac{\pi m z}{\ell}\right)e^{-i\pi mVt/\ell} & \text{for } t>0 \end{cases} \quad \ldots \text{(A3.19)}$$

Using $\sin z = \frac{1}{2i}\left(e^{iz} - e^{-iz}\right)$, equation (A3.19) becomes

$$y_\delta(\xi,z,t) = \begin{cases} 0 & \text{for } t<0 \\ \dfrac{2}{\pi MV}\displaystyle\sum_{m=1}^{\infty}\frac{1}{m}\sin\left(\frac{\pi m\xi}{\ell}\right)\sin\left(\frac{\pi m z}{\ell}\right)\sin\left(\frac{\pi m Vt}{\ell}\right) & \text{for } t>0 \end{cases} \quad \ldots \text{(A3.20)}$$

This is the solution to equation (A3.2) with $F(z,t) = \delta(z-\xi)\,\delta(t)$.

A3.6 THE RESPONSE TO A GENERAL FORCE

For the most general type of force $F(\xi,\tau)$ the response of the string is given by equation (A3.4). Substituting for $y_\delta(\xi,z,t-\tau)$ from equation (A3.20) into (A3.4) gives

$$y(z,t) = \frac{2}{\pi MV}\sum_{m=1}^{\infty}\frac{1}{m}\left\{\int_{-\infty}^{\infty}\sin\left[\frac{\pi m V}{\ell}(t-\tau)\right]d\tau \cdot \int_0^{\ell}\sin\left(\frac{\pi m\xi}{\ell}\right)F(\xi,\tau)\,d\xi\right\}\sin\left(\frac{\pi m z}{\ell}\right) \quad \ldots \text{(A3.21)}$$

A3.7 THE APPLICATION TO A THETA PINCH

The equation of motion of a theta pinch in the presence of a perturbing field produced by a nearby current loop can be written (see equation (6.4.5))

$$\frac{\partial^2 y}{\partial t^2} - V^2\frac{\partial^2 y}{\partial z^2} = -\frac{6\mu_o V^2}{4\pi}\,\frac{n A_d I_o(1-4(z/b)^2)}{b^4 B_e\,(1+(z/b)^2)^{\frac{7}{2}}}\sin\omega t \quad \ldots \text{(A3.22)}$$

where the symbols are defined as for equation (6.4.5), and $-\infty < z < +\infty$. Equation (A3.21) can be used to solve equation (A3.22) if the substitution

$$\frac{F(\xi,\tau)}{M} = -\frac{6\mu_o V^2 n A_d I_o \mu_o\left(1-4\left(\frac{\xi-\xi_o}{b}\right)^2\right)}{4\pi b^4 B_e\left(1+\left(\frac{\xi-\xi_o}{b}\right)^2\right)^{\frac{7}{2}}}\sin\omega\tau \quad \ldots \text{(A3.23)}$$

is made, where ξ_o is the axial position of the current loop.

In the theory leading to equation (A3.21) the impulsive force was applied at time $t = 0$. A sinusoidal force can then be expressed as a cosinusoidal force starting at $t = -\pi/2\omega$. The integration in time is then from $-\pi/2\omega$ to t, and the integration in space from $\xi = 0$ to $\xi = \ell$. Equation (A3.21) then gives

$$y(z,t) = K \sum_{m=1}^{\infty} \frac{1}{m} A_m B_m C_m \qquad \ldots (A3.24)$$

where

$$K = -\frac{3\mu_o n V A_d I_o}{\pi^2 b^4 B_e} \qquad \ldots (A3.25)$$

$$A_m = \int_{-\pi/2\omega}^{t} \sin\left[\frac{\pi m V}{\ell}(t-\tau)\right] \cos(\omega\tau)\, d\tau \qquad \ldots (A3.26)$$

$$B_m = \int_{0}^{\ell} \sin\left(\frac{\pi m \xi}{\ell}\right) \frac{\left(1 - 4\left(\frac{\xi-\xi_o}{b}\right)^2\right)}{\left(1+\left(\frac{\xi-\xi_o}{b}\right)^2\right)^{\frac{7}{2}}}\, d\xi \qquad \ldots (A3.27)$$

$$C_m = \sin\left(\frac{\pi m Z}{\ell}\right) \qquad \ldots (A3.28)$$

Explicitly A_m is

$$A_m = \frac{1}{\omega\left(1-\left(\frac{mV\pi}{\ell}\right)^2\right)}\left\{\sin\left[\frac{\pi m V}{\ell}\left(\frac{\pi}{2\omega}+t\right)\right] - \frac{mV\pi}{\omega\ell}\cos(\omega t)\right\} \qquad \ldots (A3.29)$$

The integral B_m (equation (A3.27)) was evaluated numerically on an I C L 470 computer, using a 5 point Newton-Cotes quadrature subroutine[77]. The complete solution (equation (A3.24)) converged when the number of summation steps was taken as $m = 1$ to 500.

APPENDIX A.4

THE NUMERICAL SOLUTION OF THE THETA PINCH EQUATION OF MOTION

A4.1 INTRODUCTION

The equation of motion of a theta pinch in the presence of a local perturbing field (section 6.4, equation (6.4.3)) was solved numerically on an I C L 470 computer. The program used was adapted from a code written by W. Schneider which solved the equation of motion of an $m=1$ unstable theta pinch (see Section 2.8.4 and Section 6.2). A description of the code with an additional forcing term $F(z,t)$ (see equation (6.4.4)) is given.

A4.2 THE CODE

The hyperbolic equation of motion was solved as an initial value problem with

$$y(z)_{t=0} = 0 \qquad \ldots (A4.1)$$

$$\dot{y}(z)_{t=0} = 0 \qquad \ldots (A4.2)$$

and the boundary conditions

$$y(z=\ell/2) = 0 \qquad \ldots (A4.3)$$

$$\dot{y}(z=\ell/2) = 0 \; . \qquad \ldots (A4.4)$$

That is, the plasma ends, at $z=\pm\ell/2$, were fixed.

The initial conditions were applied as functions of the axial distance z, with the definitions

$$Y_{44} = 4\pi\rho \qquad \ldots (A4.5)$$

$$XK = (2-\beta+\alpha)\, B_e^2 R^2 \qquad \ldots (A4.6)$$

$$Y_4(K) = Y_{44}\, R^2 \qquad \ldots (A4.7)$$

$$Y_1(K) = XK/Y_4(K) \, , = V_{m=1}^2 \qquad \ldots (A4.8)$$

$$Y_5(K) = F(z)/M, \text{ the forcing function (see equation (6.4.4))} \qquad \ldots (A4.9)$$

$$W(K) = [Y(K+1) - Y(K)]/DZ \qquad \ldots (A4.10)$$

where

ρ	is the mass density
α	describes the conducting wall radius (see Section 6.2)
R	is the plasma radius
K	is the axial (z) coordinate array
DZ	is the axial step length
Y(K)	is the solution.

The explicit solution proceeded by calculating

$$W_K^J = W_K^{J-1} + DT^J \left[\dot{Y}_{K+1}^{J-1} - \dot{Y}_K^{J-1} \right] / DZ \qquad \ldots (A4.11)$$

$$\dot{Y}_K^J = \dot{Y}_K^{J-1} + DT^J \left[Y_{1K}^J \left(W_K^J - W_{K-1}^J \right) \right] / DZ + DT^J \cdot Y_{5K}^J \, f(T^J) \qquad \ldots (A4.12)$$

$$Y_K^J = Y_K^{J-1} + \dot{Y}_K^J \, DT \qquad \ldots (A4.13)$$

with the Courant, Lewy and Friederichs stability condition [78]

$$DT^J \leq \frac{0.5 \, DZ}{(Y_{1K}^J)^{\frac{1}{2}}} \qquad \ldots (A4.14)$$

where

Y	is the velocity
J	is the time array
DT	is the time step
f(T)	is the time dependence of the force $Y_5(K)$.

The characteristic length in the problem is the distance over which the force $F(z)$ changes sign, $\simeq b$, the distance between the plasma and the current carrying loop which perturbed the field. DZ was chosen $\simeq b/50$. To reduce computing time the plasma length was set to either 0.5 or 2.0 m; the solutions were relevant only for times less than the end connection time.

Agreement to within 5% was found between the analytic (see Appendix A.3) and the numerical solutions. In no case did the conducting wall, at $R_W = 6.5$ cm, affect the results.

REFERENCES

(1) PAUL, J.W.M. In 'Physics of Hot Plasmas', Chapter 8, p.302, Oliver and Boyd, edited by Rye, B.J. and Taylor, J.C., (1970).

(2) SAGDEEV, R.Z., Proc. Symp. Appl. Math., New York, vol.XVIII, p.281, (1965).

(3) SAGDEEV R.Z. and GALEEV, A.A., Lectures on Nonlinear Theory of Plasma, TC/66/64, Trieste, (1966).

(4) UCHIDA, T. et al., Nuc. Fus., 2, 70 (1962).

(5) HOFFMAN, F. and TELLER, E., Phys. Rev., 80 692 (1950).

(6) KEVER, H., Julich Report No. Ju-2-PP. (1960).

(7) ROSENBLUTH M. and GARVIN, R., U S A E C Report No. LA-1850 (1954).

(8) KEVER, H., Nuc. Fus. Suppl., 2, 613 (1962).

(9) NIBLETT, G.B.F. and GREEN T.S., Proc. Phys. Soc., 74, 737 (1959).

(10) GREEN, T.S. et al., Phys. Fluids, 10, 1663 (1967).

(11) MEWE, R., Z. Naturfosch., 25A, 1803 (1970).

(12) BODIN H.A.B. and NEWTON A.A., Phys. Fluids, 12, 2175 (1969).

(13) ARTZIMOVICH, L.A., 'Controlled Thermonuclear Research', p.55. Oliver and Boyd, (1964).

(14) NEWTON, A.A. Nucl. Fus., 8, 93 (1968).

(15) WESSON, J.A., In Plasma Physics and Controlled Nuclear Fusion Research. Culham Conference 1965, 1, p.223, I A E A Vienna (1966).

(16) GLASSTONE, S. and LOVBERG, R.H., 'Controlled Thermonuclear Reactions' p.473, Van Nostrand (1960).

(17) BODIN, H.A.B. et al. Nucl. Fus. Suppl., 2, 521 (1962).

(18) LITTLE, E.M. et al., Nucl. Fus. Suppl., 2, 497 (1962).

(19) HINTZ, E. et al., Nucl. Fus. Suppl., 2, 601 (1962).

(20) MALESANI, G. et al., IVth European Conference on Controlled Fusion and Plasma Physics Rome, p.42, (1970).

(21) BODIN, H.A.B. and NEWTON, A.A. Phys. Fluids, 6, 1338 (1963).

(22) ROSTOKER N. and KOLB, A.C. Phys. Rev., 124, 965 (1961).

(23) HINTZ, E. and KOLB A.C., Phys. Fluids, 8, 1347 (1965).

(24) THOMAS, K.S., Phys. Rev. Letts., 23 746 (1969).

(25) HAINES, M.G., Phys. Letts., 6, 313 (1963).

(26) ROSENBLUTH, M.N. et al., Nucl. Fus. Suppl., 1, 143 (1962).

(27) TAYLOR, J.B., J. Nucl. Energy Pt.C (Plasma Physics), 4, 401 (1962)

(28) FURTH, H.P. et al., Phys. Fluids, 6, 459 (1963).

(29) WESSON, J.A., Nucl. Fusion, 6, 130 (1966).

(30) BODIN, H.A.B., Nucl. Fusion, 3, 215 (1963).

(31) EBERHAGEN, A. and GLASER, H., Nucl. Fusion, 4, 296 (1964).

(32) KALECK, A. et al., Plasma Physics and Controlled Nuclear Fusion Research, Novosibirsk Conference 1968, 2, p.581, Paper K-4, IAEA Vienna (1969).

(33) HAAS, F. and WESSON, J.A., Phys. Fluids, 10, 2245 (1967).

(34) BODIN, H.A.B. et al., Phys. Fluids, 13, 2735 (1970).

(35) MORSE, R.L., Phys. Fluids, 10, 1017 (1967).

(36) SMYTHE, W.R., 'Static and Dynamic Electricity', p.318, McGraw Hill, (1950).

(37) SMYTHE, W.R., 'Static and Dynamic Electricity', p.276, McGraw Hill, (1950).

(38) REYNOLDS, J.A., Phys. Fluids, 8, 529 (1965).

(39) ELLIS, W.R., J. Phys. D. Appl. Phys., 4, 332 (1971).

(40) POHL, F. and HEROLD, H., Garching Report No. IPP 1/31 (1964).

(41) PASCO, I.K., 'Electron Diffusion Measurements in High Energy Discharges', M.Sc. Thesis, London University, (1968).

(42) BEACH, A.D., Nucl. Fusion, 9, 215 (1969).

(43) ANDELFINGER, C. et al., Plasma Physics and Controlled Nuclear Fusion Research, Culham Conference 1965, 1, p.249, Paper CN-21/49, IAEA Vienna (1966).

(44) PASCO, I.K., 'The Early Phases of a Composite Pinch Discharge', Ph.D. Thesis, London University (1972).

(45) GLOSSAIRE de Physique des Plasmas, Bureau de Terminologie Division IX/D/1.

(46) ALFVEN, H., Ark. Mat., Astr. Fysik, 29B, no.2, (1942).

(47) ALFVEN, H., 'Cosmic Electrodynamics', p.76, Oxford (1950).

(48) ROBERTS, P.H., 'An Introduction to Magnetohydrodynamics', p.3. Longmans (1967).

(49) ARTZIMOVICH, L.A., 'Controlled Thermonuclear Reactors,' p.111, Oliver and Boyd (1964).

(50) WINCH, R.P., 'Electricity and Magnetism,' 2nd ed., p.115, Prentice Hall (1963)

(51) HUDDLESTONE, R.H. and LEONARD, S.L., 'Plasma Diagnostic Techniques,' Chapter 3, p.69, Assoc. Press. (1965).

(52) LADENBURG, R.W., 'Physical Measurements in Gas Dynamics and Combustion', Chapter 1, OUP, p.12, (1955).

(53) FINKELNBURG, W. and PETERS, T., 'Kontinuierliche Spekten', In Handbuch der Physik, (Flugge, S. ed.), 28, p.79, Berlin, Springer-Verlag (1957).

(54) GREEN, T.S. et al. Nucl. Fusion, 2, 92 (1962).

(55) BODIN, H.A.B. and McNAMARA, B., Plasma Phys., 9, 505 (1967).

(56) HOBBS, G.D. and ROSE, M.A. Culham Laboratory Report No. CLM-R3 (1963).

(57) WORSNOP, B.L. and FLINT, H.T., 'Advanced Practical Physics for Students', Chapter 1, Methuen (1961).

(58) BODIN, H.A.B. et al., In Plasma Physics and Controlled Nuclear Fusion Research, Culham Confernece (1965), 1, p.193, IAEA Vienna (1966).

(59) GOWERS, C.W. et al. Proc. of the Second Topical Conference on Pulsed High Beta Plasmas, Garching Conference (1972), Paper A4.

(60) HAIN, G. et al., Z. Naturfosch, 15a, 1039 (1960).

(61) FISHER, D.L., Culham Laboratory Report No. COS 12/66.

(62) BODIN, H.A.B. et al., In Plasma Physics and Controlled Nuclear Fusion Research, Novosibirsk Conference (1968), 2, p.533 IAEA Vienna (1969).

(63) LONG, J. and NEWTON, A.A. Xth International Conference on Phenomena in Ionized Gases, Oxford, Paper 1.1.3.7. Parsons (1971).

(64) NEWTON, A.A. and SEXTON, M.C. J. Phys. B, ser. 2, 1, 669 (1968); ser. 2, 2, 1069 (1969).

(65) NEWTON, A.A. (private communication).

(66) LITTLE, E.M. et al., Phys. Fluids, 8, 1168 (1965).

(67) GRIBBLE, R.F. et al. Los Alamos Report No. LA-DC-11581, (1970).

(68) JUNKER, J. et al., IVth European Conference on Controlled Fusion and Plasma Physics, Rome, (1970), p.155.

(69) BERNSTEIN, I.B. et al., Proc. Roy. Soc., 244A, 17 (1958).

(70) LANDAU, L.D. and LIFSHITZ, E.M., 'Course of Theoretical Physics, 1 - Mechanics', p.126, Pergamon (1960).

(71) MOROZOV, A.I. and SOLEVEV, L.S., 'Reviews of Plasma Physics', 2, p.9, Consultant's Bureau (1966).

(72) MOROZOV, A.I. and SOLEVEV, L.S., 'Reviews of Plasma Physics', 2, p.21, Consultant's Bureau (1966).

(73) SMYTHE, W.R., 'Static and Dynamic Electricity', p.270 McGraw Hill (1950).

(74) SMYTHE, W.R., 'Static and Dynamic Electricity', p.262, McGraw Hill (1950).

(75) MORSE, P.M., 'Vibration and Sound', 2nd ed. p.50, McGraw Hill (1948).

(76) MORSE, P.M., 'Vibration and Sound' 2nd ed. p.102, McGraw Hill (1948).

(77) BUCKINGHAM, R.A., 'Numerical Methods', p.79, Pitman (1962).

(78) BOOTH, A.D., 'Numerical Methods', p.125, Butterworths (1966).

(79) WOOTTON, A.J. et al., Proc. of the Second Topical Conference on Pulsed High Beta Plasmas, Garching Conference (1972), Paper C4.

(80) BODIN, H.A.B. et al. Culham Laboratory Report No. CLM-P 283 (1971).

(81) WILCOX, J.M. et al., Phys. Fluids, 4, 1506 (1961)

(82) JEPHCOTT, D.F. and MALEIN, A., Culham Laboratory Report No. CLM-P28, (1963).

(83) HARDER, C.R. et al., Phys. Rev. Letts., 27, 386 (1971).

(84) THOMASSEN, K.I., Nucl. Fusion, 11, 175 (1971).

(85) GRIBBLE, R.F. et al., Proc. of the Second Topical Conference on Pulsed High Beta Plasmas, Garching Conference (1972), Paper G1.

(86) ELLIS, W.R. et al., Proc. of the Second Topical Conference on Pulsed High Beta Plasmas, Garching Conference (1972), Paper A1.

(87) SPITZER, L., 'Physics of Fully Ionized Gases', p.133, Interscience (1962).

(88) SPITZER, L., 'Physics of Fully Ionized Gases,' p.135, Interscience, (1962).

(89) SPITZER, L., 'Physics of Fully Ionized Gases,' p.143, Interscience, (1962).

(90) SPITZER, L., 'Physics of Fully Ionized Gases,' p.146, Interscience (1962).

(91) NYQUIST, H., 'Regeneration Theory', Bell System Tech. J., 11, 126 (1932).

(92) MOROZOV, A.I. and SOLEVEV, L.S., Sov. Phys. Tech. Phys., 9, 1214 (1965).

(93) ROSENBLUTH, M.N. et al. Phys. Fluids, 12, 726 (1969).

(94) PORTER, B., 'Stability Criteria for Linear Dynamic Systems', p.11, Oliver and Boyd (1967).

(95) MURPHY, G.L., 'Basic Automatic Control Theory', p.26, D. Van Nostrand (1958).

(96) STOCKDALE, L.A., 'Servomechanisms', p.93, Pitman (1962).

(97) PORTER, B., 'Stability Criteria for Linear Dynamic Systems', p.41, Oliver and Boyd (1967).

(98) HARDING, G.E.S. and ANDERSON, J.H. 7th Symposium on Fusion Technology Grenoble (1972).

(99) PORTER, A., 'Introduction to Servomechanisms', p.88 Methuen (1961).

(100) WESSON, J.A., Lecture at Enrico Fermi Summer School, Varenna (1971).

(101) LITTLE, E.M. et al.. Plasma Physics and Controlled Nuclear Fusion Research, Novosibirsk Conference (1968), 2, p.555, IAEA, Vienna (1969).

(102) NEWTON, A.A. et al, Monteray Meeting of the A.P.S., Session No.24, Subject No.35 (1972).

(103) BODIN, H.A.B. et al., Plasma Physics and Controlled Nuclear Fusion Research, Madison Conference, 1, 225, Paper CN-28/B-5, IAEA Vienna, (1971).